AD-A273 778

THESIS

EFFECTS OF CRENULATIONS
ON THREE DIMENSIONAL LOSSES
IN A LINEAR COMPRESSOR CASCADE

William Lee Spacy II
Captain, USAF

AFIT/GAE/ENY/93D-26

93-30471

93 12 15 085

AFIT/GAE/ENY/93D-26

EFFECTS OF CRENULATIONS

ON THREE DIMENSIONAL LOSSES

IN A LINEAR COMPRESSOR CASCADE

THESIS

Presented to the Faculty of the Graduate School of Engineering

of the Air Force Institute of Technology

Air University

In Partial Fulfillment of the

Requirements for the Degree of

Master of Science in Aeronautical Engineering

William Lee Spacy II

Captain

December, 1993

Approved for public release: distribution unlimited.

Acknowledgments

The completion of this thesis is the culmination of a great deal of time and effort. I would not have been able to finish it without the help I received from a great many people. I would like to take this opportunity to thank these people for the enormous amount of help they gave me.

First I would like to thank my advisor Dr. Paul I. King for the guidance he gave me during the course of the project. In addition to advice on specific details of experimental research, he helped me to stay focused on the objective of the thesis. His help was indispensable. I would also like to thank the other members of my thesis committee Dr. William C. Elrod and Dr. Milton E. Franke for the time and effort they devoted to helping me conduct a thorough investigation and write up a concise report. Dr. Elrod in particular was always available for advice when problems arose.

The support I received from the AFIT model shop was also critical. David Driscoll and Timothy Hancock fabricated the compressor blades used in the investigation, John Brohas built the cascade test section and Ronald Ruley made the modifications to the hot-film and total pressure rake probes. Each of these individuals produced excellent workmanship and timely results which were essential to the success of this thesis.

The laboratory technicians Jay Anderson, Andrew Pitts, Daniel Rioux, and Mark Deriso were also helpful. They were always available to help with equipment

Table of Contents

List of Figures

vii

List of Tables

List of Symbols

Symbol

AFIT	Air Force Institute of Technology
AR	blade aspect ratio
ASME	American Society of Mechanical Engineers
$AVDR$	axial velocity density ratio
LE	leading edge
PS	pressure surface
SS	suction surface
SSE	sum squared error over hot-film probe calibration range
TE	trailing edge
WVD	wake velocity deficit

a	point of maximum camber measured from leading edge (cm)
A	a general quantity, also hot-film sensor calibration constant
$\tilde{A}$	mass averaged general quantity
b	temperature loading factor
B	hot-film sensor calibration constant
c	blade chord (cm)
C	hot-film sensor calibration constant
C_p	static pressure coefficient

d_s	hot-film sensor diameter (m)
i	incidence angle (degrees)
$i*$	nominal incidence angle (degrees)
I_T	outlet turbulence intensity (%)
j	index for individual data point in the sample set
k	cooling ratio of hot-film sensor
l	spanwise distance from center of blade (cm)
n	number of data points in the sample set
Nu	Nusselt number
p	static pressure on blade surface (Pa)
p_1	static pressure at cascade inlet (Pa)
P_{01}	total pressure at cascade inlet (Pa)
p_2	static pressure at cascade exit (Pa)
P_{02}	total pressure at cascade exit (Pa)
P_{int}	stilling chamber static pressure (Pa)
R	gas constant (J/kg-K)
Re	Reynolds number
s	one blade spacing (cm)
T	static temperature of fluid about hot-film sensor (K)
T_1	cascade inlet static temperature (K)
T_2	cascade exit static temperature (K)

T_r	Eckert reference temperature (K)
T_{ot}	stilling chamber total temperature (K)
V	actual fluid velocity about hot-film sensor (m/s)
V_1	velocity at cascade inlet (m/s)
V_2	velocity at cascade exit (m/s)
$\tilde{V}_2$	mass averaged velocity in cascade exit duct (m/s)
$\bar{V}_2$	arithmetic average of velocities sampled in exit plane (m/s)
V_{eff}	effective velocity (m/s)
V_{x1}	axial velocity at cascade inlet (m/s)
V_{x2}	axial velocity at cascade exit (m/s)
V_∞	freestream velocity in cascade exit duct (m/s)
x	axial coordinate
y	pitchwise coordinate
z	spanwise coordinate

Greek Symbol

α	angle between sensor axis and actual fluid velocity (deg)
α_1	air inlet angle = throat angle (degrees)
α_1'	blade inlet angle (degrees)
α_2	air outlet angle (degrees)
α_2'	blade outlet angle (degrees)

δ	deviation (degrees)
ε	deflection (degrees)
ε^*	nominal deflection (degrees)
ϕ_1	angle between chord line and meanline at LE (degrees)
ϕ_2	angle between chord line and meanline at TE (degrees)
γ	ratio of specific heats
μ	viscosity (N· s/m²)
ν_x	mean x-component of velocity fluctuations (m/s)
ν_y	mean y-component of velocity fluctuations (m/s)
ρ_1	density at cascade inlet (kg/m³)
ρ_2	density at cascade exit (kg/m³)
σ^2	outlet velocity variance (%)
$\tilde{\sigma}^2$	mass weighted outlet velocity variance (%)
ω	total pressure loss coefficient
ζ	stagger angle (degrees)

Abstract

An experimental investigation into the effect of compressor blade trailing edge geometry on three-dimensional flows in a linear cascade was conducted at the AFIT linear cascade test facility. Hot-wire/hot-film anemometry along with total pressure instrumentation was used to analyze crenulation generated vortices and their interaction with the three-dimensional flows in the cascade. The effects of this interaction on the performance parameters associated with the cascade were quantified. The results indicate that wake mixing is better for crenulated trailing edges and that the precise geometry of the crenulations is critical to performance. One crenulation geometry was found to increase wake mixing while slightly reducing the total pressure losses.

EFFECTS OF CRENULATIONS

ON THREE-DIMENSIONAL LOSSES

IN A LINEAR COMPRESSOR CASCADE

I. Introduction

Background

In the continuing search for improved turbine engine performance a premium is

placed on size and weight. Two areas of potential gain are decreasing the space

required between blade rows of the compressor and shortening the length of the

combustor. These reductions would result in a lighter more compact engine for a

specified power rating. One limit imposed on both the inter-stage spacing and the

combustor length, results from the need to have uniform airflow entering each of these

devices. Each blade in a stator (or rotor) creates a region of low velocity air

immediately behind it, called the wake, caused by the combining of the boundary

layers from the two blade surfaces (Figure 1). For optimum performance there must

be enough room to allow the blade wakes to dissipate both between stages and before

entering the combustor. Previous efforts have examined the possibility of using

crenulations, or notches, on the trailing edges of compressor blades to increase the rate

of wake dissipation and shorten this required spacing. These investigations showed that compressor blades with crenulated trailing edges increase wake dissipation and decrease total pressure losses in a linear cascade. Until now only two crenulation geometries have been explored, one with large crenulations and one with small crenulations (Figures 2.a, 2.b). The interactions of the vortices generated by these crenulations with the secondary flow fields of the cascade have yet to be investigated. Additionally, there is likely an optimum crenulation geometry or at least a range of configurations that yield better performance than those already tested. This research investigated three new crenulation geometries in a linear cascade with significant three dimensional effects. This investigation focused on the performance of the blades, and the interaction of their associated vortices with those present in the cascade.

In pursuing methods of improving wake dissipation Wennerstrom (1982) hypothesized that crenulations in the trailing edges of compressor blades might help increase the rate of wake dissipation. These crenulations would create counter-rotating vortices that would more quickly mix the low velocity, low momentum wake air with the high velocity freestream air (Figure 3). This active mixing should cause the flow behind the blades to become uniform more quickly.

The most recent investigations into this phenomenon were by Veesart (1989) and DeCook (1991) using the Air Force Institute of Technology (AFIT) linear cascade test facility. Veesart's investigation compared straight trailing edge blades with two crenulation geometries, the large and small crenulations depicted in Figures 2.a and 2.b. Her investigation indicated that both crenulation geometries improved not only

2

wake mixing but also flow turning angle and total pressure losses. DeCook's investigation (1991) used the same blade geometries and centered on the effects of sidewall suction and turbulence levels on the results obtained by Veesart. DeCook's investigation showed an improvement in wake mixing and total pressure losses, both with and without suction and turbulence injection, but did not reproduce the turning angle improvements for either crenulation geometry. In both of these investigations the large crenulation geometry produced the most significant improvements in wake mixing but also suffered the greatest losses of turning angle. The small crenulations had smaller turning and total pressure losses but did not dissipate the wake as fast as the large crenulations. Both geometries had faster wake dissipation and lower total pressure losses than the straight trailing edge blade.

Kang and Hirsch (1991) recently investigated the three-dimensional flows that developed in a linear cascade which had no provisions for sidewall boundary layer control. Their investigation used a cascade similar to the one used in this investigation and carefully examined the structure of the three-dimensional flows. The flow structure proposed by Kang and Hirsch (1991) appeared to be present in the cascade used in this experiment and is discussed later. The interactions between the crenulation vortices and these cascade vortices were examined to determine the causes of the previously mentioned gains in performance.

Problem Statement

Compressor blades with crenulated trailing edges have been shown to increase wake dissipation and decrease total pressure losses in a linear cascade. Until now only two crenulation geometries have been explored, the large and small crenulations depicted in Figure 2. The purpose of this investigation is to explore the interaction between the vortices generated with crenulated trailing edge blades and the three-dimensional flow characteristics of a linear cascade. Three new crenulation geometries were tested in an attempt to find one with a better combination of wake mixing, pressure losses and turning angle.

Scope

This thesis encompassed the design and testing of three new blade crenulation geometries (Figures 2.c-2.e) in the search for an improvement over previous designs. One crenulation geometry, Figure 2.c, was designed as a compromise between the two previously tested geometries and, as will be shown later, yielded the best results. The second geometry, Figure 2.d, explored a totally new design to determine its suitability in this application. The last new design, Figure 2.e, was designed specifically to try and diminish the intensity of the three dimensional effects.

4

To provide a direct comparison with previous work, the large crenulation blades tested in earlier investigations were also fabricated (Figure 2.b). To provide a baseline for this specific cascade a set of straight trailing edge blades was fabricated and tested. Of interest was the universality, with various blade configurations, of the previously discovered reduction in total pressure losses.

II. Theory

General Description of a Cascade

A cascade is a row of identical blades which is normally used to change the direction and pressure of a flowing gas. Cascades have been widely used to model the flow environment in axial flow compressors. A *linear* cascade (as opposed to an annular cascade) is a cascade which has its blades arranged as if they were mounted on a hub with an infinite radius of curvature. Consequently, the edges of the blades in a linear cascade are parallel to each other.

A cascade is typically defined by specifying the blade profile, the geometric arrangement of the blades, and the flow condition. The nomenclature used to define a particular linear cascade are identified in Figure 4. The blade geometry is specified by the blade chord length (c), the blade camber angle (θ), the point of maximum camber (a, typically measured along the chord and normalized by chord length), the blade thickness distribution, and the aspect ratio (AR). The aspect ratio is defined as the blade span normalized by the blade chord. The arrangement of the blades is specified by the blade spacing (s), the stagger angle (ζ), the blade inlet angle (α_1'), and the blade outlet angle (α_2'). The flow condition of the cascade is specified by the air inlet angle (α_1) and velocity (V_1), and the air outlet angle (α_2) and velocity (V_2). Various other cascade descriptors can be derived from these basic parameters. Three

6

descriptors which are typically used are the deviation angle (δ), the incidence angle (i), and the deflection angle (ϵ). The deviation angle, as shown in Figure 4, is the angle between the tangent to the mean camber line at the trailing edge and the outlet flow velocity vector. Likewise, the incidence angle is the angle between the inlet flow velocity vector and the tangent to the mean camber line at the leading edge. The deflection is simply the amount by which the flow was turned, i.e. the angle between the inlet flow and exit flow velocity vectors.

Ideal Cascade Flow

An ideal cascade would have an infinite number of blades. An infinite number of blades would eliminate the viscous effects of the cascade endwalls on the flow. These effects are undesirable because there are no analogous effects in an axial flow compressor.

In many cascade experiments, it would also be ideal to have blades of infinite span. Blades of infinite span would eliminate the viscous effects of the cascade sidewalls on the flow. The elimination of sidewall effects (given uniform flow conditions at the flow source) would result in two-dimensional flow. Two-dimensional flow as specified by Erwin and Emery (1950) has the characteristics listed below.

7

1. Equal pressures, velocities, and directions exist at different spanwise locations.

2. The static pressure rise across the cascade equals the value associated with the measured turning angle and wake.

3. No regions of low energy flow, other than blade wakes exist. The blade wakes are constant in the spanwise direction.

4. The measured force on the blades equals that associated with the measured momentum and pressure change across the cascade.

5. The various performance values do not change with aspect ratio, number of blades, or other physical factors of the tunnel configuration.

Cascade flow which is two-dimensional is thought to have the broadest application to axial flow compressor design in general.

Although purely two-dimensional flow affords considerable simplification in interpreting cascade results, it is often impractical to achieve. In practice, a finite amount of three-dimensionality in cascade flow can be tolerated, and useful results can still be produced. In some cases, a cascade with three-dimensional effects may be useful in modeling a specific flow condition in a compressor. For example, the flow through the last row of stator blades in a compressor may have strong three-dimensional effects. The characteristically low aspect ratio of these blades allow the viscous effects at the compressor casing and hub to significantly degrade the two-

dimensionality of the flow. The blades used in this experiment are low aspect ratio blades ($AR = 1$) which are representative of those typically used as the last row of stator blades in an axial flow compressor; achieving two dimensional flow was not the intent of this study. The two dimensional flow condition did serve as a point of comparison to qualitatively assess the degree of secondary flow present in the cascade.

Quantification of Cascade Performance

Several parameters can be used to quantify the performance of linear cascades. These parameters serve two purposes. They, 1) provide a basis for evaluating the validity of the cascade as a model, and 2) provide a basis for evaluating the aerodynamic performance of the particular concept being modeled. In this study, the concept being considered is the effect of using crenulated blades where three-dimensional flow is present. Since some of these parameters are expressed with respect to a coordinate system, the cascade coordinate system used in this investigation is defined as shown in Figure 5.

Evaluation of the Cascade as a Model. The validity of the cascade as a model can be evaluated by determining the periodicity and the axial velocity density ratio ($AVDR$) of the cascade. Periodicity refers to the blade-to-blade static pressure or velocity variation at the cascade inlet and exit. These distributions should vary in a cycle from blade-to-blade for periodicity to be achieved. According to Gostelow (1984), periodicity is essential for a cascade to be considered a valid model.

9

The *AVDR* is an indication of the two-dimensionality of the flow. If a cascade

has no spanwise gradients of momentum, the *AVDR* = 1.0 and the flow is two-

dimensional. An *AVDR* > 1.0 indicates flow contraction and a subsequent increase of

the midspan mass flux through the cascade.

The *AVDR* is defined as:

$$AVDR = \frac{\int_{s^-}^{s^+} (\rho_2 V_{x_2})_{midspan} \, dy}{\int_{s^-}^{s^+} (\rho_1 V_{x_1})_{midspan} \, dy} \tag{1}$$

Where $s^+ - s^-$ is one blade spacing. If a discrete number of data points comprising at

least one blade spacing are sampled in the y-z plane (Figure 5), with equal spacing in

the y-direction such that the spacing between the data points is sufficiently smaller

than the sample range, the mass average of the *AVDR* can be approximated

numerically. Using this approximation, Equation (1) was re-cast in terms of a

summation of the exit quantities and the measured inlet conditions.

These changes resulted in Equation (2) below:

$$AVDR = \frac{\sum_{j=1}^{n} (\rho_{2_j} V_{x_{2_j}})_{midspan}}{\sum_{j=1}^{n} \rho_{1_j} V_{x_{1_j}}} \tag{2}$$

Results from cascades with non-unity *AVDR* are correlated with two-

dimensional flow results (*AVDR* = 1) by the relationships presented by Gostelow

(1984). According to Gostelow (1984) caution must be exercised when using the

10

AVDR to indicate the two-dimensionality of the flow because the *AVDR* represents a mass average of the velocities at the midspan which may not accurately reflect the localized three-dimensional effects which may develop in the cascade. Examples of such effects were proposed by Kang and Hirsch (1991) as well as Tang et al. (1991).

Kang and Hirsch (1991) used a cascade very similar to the one used in this investigation to examine the structure of the secondary flows in a cascade. They proposed a flow structure that included a new *concentrated shed* vortex (Figure 6). Figure 6 depicts the three vortices associated with each sidewall that were proposed by Kang and Hirsch (1991). This figure depicts the approximate locations of the vortices in a plane perpendicular to, and just behind the blade row, i.e. the concentrated shed vortex was located at about 30% span from the sidewall. The horizontal line is the trailing edge of a blade and the vortices are located just below the suction surface. Tang et al. (1991) also investigated three-dimensional effects in a linear cascade and found a very similar system of vortices. These vortices comprise the major features of the three-dimensional flow.

Evaluation of Aerodynamic Concepts using the Cascade. With the periodicity and *AVDR* established, the aerodynamic performance of a cascade can be determined. Common indicators of cascade performance are the total pressure loss coefficient (ω), the blade static pressure coefficient (C_p), the non-dimensional static pressure rise (C_p), and the flow turning angle or deflection (ϵ). Since this investigation focuses in part

11

on the wakes generated by the cascade, it is also relevant to quantify the character of the flow downstream of the cascade. This can be accomplished with (in addition to ω) the wake velocity deficit (WVD) and outlet velocity variance (σ^2).

The static pressure coefficient is defined as:

$$C_p = \frac{p - p_1}{\frac{1}{2}\rho_1 V_1^2} \qquad (3)$$

Where p is the static pressure on the blade surface or at the cascade exit and the other values are as previously defined. C_p is useful in quantifying blade performance because it can be integrated over the blade surface to find the net force of the fluid acting on the blade. The net force on the blade is equal in magnitude and opposite in direction to the net force on the fluid. Through conservation of momentum and a force balance on the blades, it follows that the net force on the fluid indicates the amount of flow-turning caused by the blade. Since compressor blades are designed to turn the flow, C_p profiles for blades in different cascade configurations, or for blades with different geometries, provide a comparative indication of blade performance.

The total pressure loss coefficient is defined as

$$\overline{\omega} \equiv \frac{P_{01} - P_{02}}{\frac{1}{2}\rho_1 V_1^2} \qquad (4)$$

Determination of ω provides an indication of the energy lost through the cascade due to viscous dissipation. A value of zero with no heat or work added would indicate isentropic flow through the cascade. The total pressure loss coefficient can be useful

12

in defining the incidence angle at which a particular cascade is stalled. For example, Dixon (1986) specifies the incidence at which stall occurs as being that which corresponds to twice the minimum ω.

Gostelow (1984) states that for a steady, incompressible flow the non-dimensional pressure rise through a two-dimensional cascade may be expressed as (referring to Figure 4):

$$C_p = 1 - \frac{\cos^2\alpha_1}{\cos^2\alpha_2} - \bar{\omega} \tag{5}$$

This expression for C_p provides a means of estimating flow turning $(\alpha_1 - \alpha_2)$ through a linear cascade from pressure measurements at the exit, provided the inlet conditions are known. In this case, C_p is determined by using Equation (3) with p measured just downstream of the blade trailing edge.

The wake velocity deficit and the outlet velocity variance are defined with the use of average properties. Since the wake region is a region of varying mass flow, a mass averaging scheme is used in the wake region. The mass average of some quantity A, is defined as:

$$\tilde{A} \equiv \frac{\int_{s^-}^{s^+} \int_{1^-}^{1^+} A \rho_2 V_{x_2} \, dz \, dy}{\int_{s^-}^{s^+} \int_{1^-}^{1^+} \rho_2 V_{x_2} \, dz \, dy} \tag{6}$$

Where z is the spanwise coordinate, l^+ is the spanwise maximum of the measurement plane and l^- is the spanwise minimum of the measurement plane (Figure 5). If a discrete number of data points are sampled in the y-z plane with equal spacing in the

13

y-direction and equal spacing in the z-direction such that the spacing between the data points is sufficiently smaller than the sample range, the mass average of A can be approximated numerically by:

$$\tilde{A} = \frac{\sum\limits_{j=1}^{n} \rho_{2_j} V_{x_{2_j}} A_j}{\sum\limits_{j=1}^{n} \rho_{2_j} V_{x_{2_j}}} \qquad (7)$$

The wake velocity deficit is defined as:

$$WVD \equiv 1 - \frac{\tilde{V}_{x_2}}{V_\infty} \qquad (8)$$

Where $\tilde{V}_{x2}$ is mass averaged axial velocity in the cascade exit duct and V_∞ is the freestream velocity in the cascade exit duct.

The value of the wake velocity deficit would be expected to be nearly 0 immediately downstream of a cascade which had blades with a sharp trailing edge. This is because a wake trailing a sharp edge would have a very narrow width and account for a relatively small portion of the total mass flow throughout the cascade. For incompressible flow over an airfoil with zero lift, it follows from White (1991) that as the wake develops downstream of the airfoil, the wake velocity deficit should initially increase to a maximum and then decay to a value approaching 0 at a location

14

far downstream of the airfoil. White (1991) went on to point out that the flow behind a cascade of cambered blades is likely to be complicated with shed vortices and therefore the above trend can be thought of as a time averaged trend..

The exit velocity variance is the square of the standard deviation of the exit velocity distribution. It is normalized by the square of the mean exit velocity and is defined as:

$$\sigma^2 \equiv \frac{1}{\overline{V_2}^2} \cdot \frac{\sum_{j=1}^{n} (V_{2_j} - \overline{V_2})^2}{(n-1)} \tag{9}$$

This calculates the sample variance as opposed to the population variance. Due to the variations of mass flow in the wake region discussed previously, it is appropriate to calculate a mass weighted variance. The mass weighted exit velocity variance is defined below (DeCook, 1991).

$$\sigma^2 \equiv \frac{1}{\overline{V_2}^2} \cdot \frac{\sum_{j=1}^{n} \rho_{2_j} V_{x_{2_j}} (V_{2_j} - \overline{V_2})^2}{\overline{\rho_2 V_{x_2}} (n-1)} \tag{10}$$

Where $\overline{\rho_2 V_{x2}}$ is the arithmetic mean of the mass flux in the axial direction.

The variance can not be evaluated at a single data point; it applies to a set of data points. Consequently, the mass weighted exit velocity variance is not a mass averaged quantity per the definition previously given (Equation 6). However, the mass weighted exit velocity variance was converted into an expression which takes a mass averaged form.

Expressing the mean mass flux term as a sum yields:

$$\sigma^2 \equiv \frac{1}{\overline{V_2}^2} \cdot \frac{\displaystyle\sum_{j=1}^{n} \rho_{2_j} V_{x_{2_j}} (V_{2_j} - \overline{V_2})^2}{\left(\dfrac{\displaystyle\sum_{j=1}^{n} \rho_{2_j} V_{x_{2_j}}}{n}\right)(n-1)}$$

(11)

Which rearranges to:

$$\sigma^2 \equiv \frac{n}{(n-1)} \cdot \frac{1}{\overline{V_2}^2} \cdot \frac{\displaystyle\sum_{j=1}^{n} \rho_{2_j} V_{x_{2_j}} (V_{2_j} - \overline{V_2})^2}{\displaystyle\sum_{j=1}^{n} \rho_{2_j} V_{x_{2_j}}}$$

(12)

Introducing the squared mean exit velocity into the sum in the numerator:

$$\sigma^2 \equiv \frac{n}{(n-1)} \cdot \frac{\displaystyle\sum_{j=1}^{n} \rho_{2_j} V_{x_{2_j}} \left(\dfrac{V_{2_j}}{\overline{V_2}} - 1\right)^2}{\displaystyle\sum_{j=1}^{n} \rho_{2_j} V_{x_{2_j}}}$$

(13)

The expression now takes on the mass averaged form:

$$\partial^2 = \frac{n}{(n-1)} \cdot \text{mass average of } \left(\frac{V_2}{\overline{V_2}} - 1\right)^2$$

(14)

16

III. Experimental Apparatus

The experimental apparatus consists of five major components. These components are the air supply system, the diffuser/stilling chamber, the throat, the cascade test section, and the instrumentation. A description of each component is provided in this section.

Air Supply System

A schematic of the air supply system and diffuser/ stilling chamber is shown in Figure 7. The air supply system consists of a 30 kW centrifugal blower which delivers air to the test section at approximately 1.6 kg/s and produces an inlet flow Mach number of approximately 0.4 for the cascade test section. The blower is configured so that it can use outside air, laboratory air, or a combination of outside and laboratory air. This option is useful for controlling the total temperature of the flow through the cascade. The air is electrostatically filtered before entering the diffuser.

17

Diffuser/Stilling Chamber

The air from the blower is diffused to approximately 3 m/s in the stilling chamber. The stilling chamber is cylindrical with an internal diameter of approximately 1.1 m. It also has provisions for conditioning and straightening the flow prior to the test section entrance, and contains a styrofoam center body plug which is covered with foam rubber. The plug provides a gradual cross-sectional area change for diffusion of the flow; it also obstructs the acoustic path between the blower and the test section. A 40 mesh wire screen, a cloth filter, and a 10 cm thick honeycomb grid provide the final flow conditioning and straightening before the flow exits the stilling chamber through a rectangular ASME long-radius bellmouth nozzle. The nozzle throat has a 5.08 cm by 20.32 cm cross-section. A more detailed description of the air supply system and diffuser/stilling chamber is given by Allison (1982).

Throat and Cascade Test Section

A schematic of the cascade test section is shown in Figure 8. Shown in Figure 8, the throat has provisions for endwall boundary layer removal. Suction was applied to the endwall suction slots for all cascade testing. Also shown, the test section holds 7 blades. The profile of the blades used in this study is shown in Figure 9; its surface coordinates and mean camber line are listed in Table 1. The details of the blade geometry, including the determination of the camber angle and the

18

blade inlet and exit angles, are covered in Appendix A. Although the blade profile was fixed throughout this study, the trailing edge of the blades differed depending on whether the blades were crenulated or not crenulated. The planform of each blade tested is shown in Figure 2. During a single test run all 7 blades were the same, either crenulated or not crenulated.

In order to vary the incidence angle, the test section interfaces directly with any one of four interchangeable throat sections. This interface is schematically shown in Figure 8. Each throat section causes the cascade to see a unique air inlet angle. These air inlet angles and the corresponding incidence angles are listed in Table 2. This method of varying the incidence angle allows the stagger angle to remain fixed throughout the testing. As can be seen from Figure 8, the throat/test section interface requires that the cascade test section accommodate various inlet areas. This is accomplished with the adjustable endpieces in the cascade test section. The endpieces were adjusted by using a shim of the appropriate thickness for each incidence angle. Depending on the incidence angle tested, the spacing between the outer-most blade and the cascade endwall varies from 1.1 cm to 2.9 cm. This variation in endwall spacing can be expected to affect the performance of the outer blades. However Erwin and Emery (1950) found that variations in endwall spacing had a negligible effect on the performance of the center blade. Since the primary focus of this experiment is on the center blade, the variations in endwall spacing were determined to be acceptable. For this investigation the incidence angle was held constant at $4.49°$ for all of the blade configurations.

19

The center blade of each cascade was fabricated with static pressure ports on its pressure surface and suction surface to allow a midspan blade surface pressure distribution to be obtained. The position of these ports along the blade chord are listed in Table 3. It should be noted that the crenulated blades have the furthest downstream pressure port omitted due to interference with the crenulations. The cascade specifications as defined in Chapter II are listed in Tables 2 and 4.

Table 1. Blade Surface Coordinates and Mean Camber Line

Suction	Suction	Pressure	Pressure	Mean
5.001	0.000	5.001	0.000	0.000
4.902	0.020	4.901	0.009	0.015
4.703	0.061	4.699	0.028	0.044
4.404	0.119	4.497	0.046	0.083
4.257	0.148	4.245	0.069	0.108
4.010	0.202	3.992	0.092	0.147
3.612	0.285	3.590	0.132	0.208
3.213	0.359	3.189	0.169	0.264
2.811	0.420	2.790	0.198	0.309
2.404	0.456	2.397	0.213	0.335
1.997	0.460	2.004	0.210	0.335
1.744	0.448	1.757	0.201	0.325
1.491	0.427	1.510	0.189	0.308
1.238	0.396	1.263	0.172	0.284
0.986	0.356	1.015	0.150	0.253
0.734	0.304	0.766	0.122	0.213
0.483	0.239	0.517	0.087	0.163
0.383	0.209	0.417	0.071	0.140
0.283	0.174	0.317	0.053	0.114
0.184	0.134	0.216	0.034	0.084
0.086	0.084	0.114	0.013	0.049
0.038	0.053	0.062	0.002	0.028
0.016	0.033	0.034	-0.002	0.015
0.000	0.011	0.010	-0.004	0.004
0.000	0.000	0.000	0.000	0.000

Note: For Table 1, x refers to distance from leading edge along the blade chord and y refers to perpendicular distance from blade chord

21

Table 2. Throat Angles and Corresponding Incidence Angles

α_4 (deg)	i (deg)
25.43	-1.08
31.00	+4.49
35.83	+9.32
38.95	+12.44

Table 3. Location of Blade Static Pressure Ports

Location in Fraction of Chord	
Suction Surface	Pressure Surface
0.045	0.070
0.095	0.120
0.169	0.195
0.245	0.270
0.295	0.320
0.345	0.370
0.395	0.420
0.445	0.470
0.495	0.520
0.545	0.620
0.645	0.670
0.695	0.720

Table 4. Cascade Specifications

Specification	Symbol	Value
Blade Chord Length	c	5.0 cm
Blade Camber Angle	θ	30.51
Blade Inlet Angle	α_1'	26.51
Blade Outlet Angle	α_2'	-4.00
Point of Maximum Camber	a	0.5 chord
Blade Spacing	s	3.4 cm
Stagger Angle	ζ	7.50 deg
Air Inlet Angle	α_1	see Table 2
Inlet Velocity	V_1	137-146 m/s
Outlet Velocity	V_2	107-122 m/s
Incidence Angle	i	see Table 2

Data Acquisition System

The elements of the AFIT Cascade Test Facility Digital Data Acquisition System are depicted in Figure 10. As can be seen in the figure, the acquisition system consists of a central computer and four subsystems. The four subsystems can be described functionally as (1) the pressure measurement subsystem, (2) the velocity and temperature measurement subsystem, (3) the temperature measurement subsystem, and (4) the traverse control subsystem. A detailed equipment listing is presented in Appendix B.

Central Computer. The central computer for the data acquisition system is a Zenith Z-248 computer. The computer is equipped with a math co-processor to speed numerical computations. The software which commands the acquisition process is written in MS-QuickBasic 4.5. The software consists of several multi-module programs and provides automation of both data acquisition and data reduction.

Pressure Measurement Subsystem. The pressure measurement subsystem consists of a Pressure Systems, Inc. Model 8400 Pressure Scanner, 3 32-port transducer blocks, a total pressure rake, and a CEC Model 2500 Digital Barometer. The pressure scanner was used to measure the cascade inlet total and static pressures, the blade surface static pressures, and the cascade exit total and static pressures. The digital barometer was used to measure the facility ambient pressure.

As configured in this study, the pressure scanner scanned the output from the transducer blocks at a rate of 20 kHz. For one data point, it scanned each of the 96 ports 11 times and averaged the 11 values which resulted in a total sample time of

24

0.053 seconds. The pressure scanner has an internal certified standard transducer which was used for calibration at the beginning of each test run. The standard transducer is supported by an internal heater to minimize the impact of ambient temperature fluctuations.

The transducer blocks provided 96 transducers from which pressure was measured. Each transducer block has 1 reference port which was vented to ambient conditions. Each block also contains a plunger operated valve which redirects the sensing location of the transducers to a known reference pressure during calibration.

The total pressure rake was used to measure the total pressure at the cascade exit. A schematic of the total pressure rake is shown in Figure 11. Each of its 11 tubes has an inner diameter of 0.0635 cm and an outer diameter of 0.0889 cm. The centers of the tubes are equally spaced at 0.381 cm. This spacing resulted in a measurement span of 75% of the blade span.

The digital barometer was used to measure ambient pressure for each data point. It is equipped with an IEEE 488 interface which facilitated automation of the ambient pressure data acquisition. The digital barometer also has an internal heater to minimize the impact of ambient temperature fluctuations.

Velocity and Temperature Measurement Subsystem. The velocity and temperature measurement subsystem consisted of a TSI Model IFA 100 Intelligent Flow Analyzer, a TSI Model IFA 200 System Multichannel Digitizer, TSI x-configuration hot-film sensors, and a thermocouple.

The intelligent flow analyzer was used to acquire velocity and temperature data. It contains a Model 140 temperature module which acquires voltages from 2 thermocouples. It also contains 2 Model 150 constant temperature anemometer modules which acquire voltages from the hot film sensors. The gain, offset, and low pass filtering are provided by three Model 157 signal conditioners. As configured in this study, the gain was set to 5 and the offset was set to 2, to make maximum use of the range of the digitizer. The low pass filter was set to 5 kHz to eliminate aliasing.

The multichannel digitizer was used to scan and digitize the voltages from the signal conditioners in the intelligent flow analyzer. It contains three Model 252 digitizers. As configured in this study, the digitizer acquired the velocity and temperature raw data simultaneously at a sample rate of 10 kHz.

The hot-film sensors were used to acquire velocity and turbulence data. A schematic of the hot-film probe is shown in Figure 12. As shown in this figure, one hot-film probe consists of two sensors. PSI Model 1241-10 and Model 1241-20 x-configuration hot-film probes were used. Different model numbers were used based on the limited availability of the sensors and because the sensors are very fragile and were broken during this study. All of the sensors used gave acceptable results during the verification phase of the calibration (see Chapter IV).

The thermocouple used in this subsystem was used to measure the probe calibrator total temperature. This thermocouple is an Omega T-type copper-constantan thermocouple.

26

Temperature Measurement Subsystem. The temperature measurement subsystem was used to supplement the temperature measurement capability of the velocity and temperature measurement subsystem. This was needed because the velocity and temperature measurement subsystem is only capable of accommodating two thermocouples, and three thermocouples were used in this study. The temperature subsystem measured cascade total temperature and ambient temperature. It consists of a Hewlett-Packard Model 3455A Digital Voltmeter, a Hewlett-Packard Model 3495A Scanner, and two Omega T-type thermocouples.

Traverse Control Subsystem. The traverse control subsystem consists of two New England Affiliated Technologies Model 301 Programmable Motion Controllers and two Oriental Motor Company Stepper Motors. One of each of these was used for traverse in the cascade pitch direction, and one of each was used for traverse in the spanwise direction. When attached to the traversing mechanism, the resolution of the subsystem is ± 0.0013 cm.

Crenulation Geometry

One purpose of this investigation was to attempt to improve the wake mixing, turning angle and pressure loss characteristics of the previously tested crenulation geometries. The previous investigations revealed that each geometry had its own advantages. The small crenulation geometry had the smallest loss in turning angle but also had the smallest improvement in wake mixing and total pressure losses. The

large crenulations, on the other hand, had greater losses in turning angle, but better wake mixing, lower total pressure losses and seemed to diminish the size of the secondary flow vortices. With these facts in mind the new blade crenulation geometries were conceived.

The first new crenulation geometry is a combination of the previous large and small crenulation geometries (Figure 2.c). For this configuration the depth of the large crenulations was combined with the width and spacing of the small crenulations. The large crenulation depth was chosen on the premise that the greater pressure differences found closer to the leading edge of the blade helped to drive the wake mixing generated by the crenulations. The width and spacing of the small crenulations was chosen in an attempt to regain some of the flow turning lost with the large crenulations. It was thought that the loss of flow turning was due in part to the loss of a great deal of the trailing edge with the large crenulation geometry.

The second geometry was arrived at after looking at the total pressure loss contour plots presented in DeCook's thesis (1991). A comparison of the *Suction off, Turb off* plots for each of his geometries showed the large crenulation design to reduce the vortices near the sidewalls. This present design (Figure 2.d) tried to reproduce this effect by placing large crenulations the edges of the blades in an attempt to diminish these vortices. The design incorporated small crenulations in the center of the blade to retain the flow turning and pressure rise characteristics of this geometry. It was hoped that this design would produce lower total pressure losses than the small crenulation geometry and greater flow turning than the large one.

28

The final geometry investigated in this thesis consisted of 6.35 mm holes drilled through blade 9.525 mm from the trailing edge (Figure 2.e). It was similar to the long narrow crenulation geometry in that the holes had the same diameter and were positioned in the same locations as the tops of these crenulations. Since there was no actual crenulation in the trailing edge it was thought that the turning angle would be more like that of the small crenulations or even the straight blades. The flow field for this case was unknown and its efficiency at wake mixing could not be predicted.

III. Experimental Procedures

Hot-wire/film Calibration

Overview. Hot-wire anemometry is a method of determining the velocity and direction of a flowing fluid by measuring the amount of energy dissipated by a heated wire placed in the flow. The two commonly used methods of measuring this energy dissipation use either constant temperature or constant current principles. This investigation used a constant temperature device. In constant temperature hot-wire anemometry the basic concept is to pass a current through a thin wire and measure the amount of voltage required to keep the resistance, and hence the temperature, constant. This input voltage is then used to determine the mass flow of the fluid flowing over the wire. From this mass flow the velocity of the fluid is determined. With an x-wire the magnitudes of the velocities flowing across two wires at a known angle to each other are measured. From these magnitudes and the known angle between the wires the direction as well as the magnitude of the velocity is determined. The operating principles of hot-wires and the development of the following equations are covered by DeCook (1991). A comprehensive bibliography of sources detailing the theory of the electrical and thermodynamic relationships behind hot-wire anemometry may be found in *A Bibliography of Thermal Anemometry* by Peter Freymuth (1982).

30

Governing Equations. As described in chapter III the two sensor types used in this investigation were TSI 1241-10 and TSI 1241-20 constant temperature x-film anemometers. The difference between the film sensors and the wire sensor described above is that the former is a quartz cylinder with a conductive film deposited on it rather than an actual wire. The equations that follow were developed by DeCook (1991) and are the ones implemented by the calibration and data reduction software. The most pertinent equations used in this investigation and are printed here for reference.

The fluid velocity is found using the following relationship:

$$Re = \frac{\rho V_{eff} d_s}{\mu} \tag{15}$$

Where V_{eff} is the effective velocity over each wire of the probe and is the vector sum of the component of velocity perpendicular to the wire and a fraction of the velocity parallel to it. The relationship between the effective velocity and the fluid velocity is:

$$V_{eff} = V \sqrt{\sin^2\alpha + k^2\cos^2\alpha} \tag{16}$$

In this equation V is the fluid velocity and α is the angle between the sensor axis and this velocity. The term k in this equation is related to the ratio of the sensor length to the sensor diameter and was determined for this investigation by an angle and velocity calibration procedure described below.

31

The Reynolds number is determined by solving the equation:

$$Nu \left(\frac{T_I}{T} \right)^b = A + B\sqrt{Re} + CRe \qquad (17)$$

In Equation (17) A, B, and C are constants determined by the previously mentioned calibration procedure and b is a temperature loading factor determined by a separate temperature calibration. Both of these calibration procedures are detailed below. The methods for determining the values of the quantities listed above are thoroughly explained by DeCook (1991)

Calibration Procedure. The calibration procedure for this device consisted of two distinct parts, a velocity and angle calibration, and a temperature calibration. The first of these required a set of velocity measurements and a set of angle measurements. This procedure determined the constants A, B, and C in Equation (17) and the value of k in the Equation (16). The first step was accomplished by performing a 31 point unidirectional calibration at a constant air temperature with velocities ranging from 65 m/s to 150 m/s. Next a 21 point unidirectional angle calibration was performed with angles ranging from positive to negative ten degrees. The velocities and angles used in this procedure were chosen to cover the range of values expected to be found in the cascade. An post mortem analysis of these choices showed them to be valid since the ranges over which the calibrations were made included two standard deviations of both the measured angles and measured velocities. In order to solve Equations (16) and

32

(17) it was necessary to set the temperature loading coefficient b to zero. The coefficients A, B and C were calculated for a range of values of k using the known calibrator velocities and angles. The resulting coefficients were then used to calculate flow velocities and angles which were compared with the angles measured with the calibrator. A sum squared error (SSE) was computed using:

$$SSE = \sum_{j=1}^{n} \left(Nu_j \left(\frac{T_{r_j}}{T_j} \right)^b - (A + B \sqrt{Re_j} + C \, Re_j) \right)^2 \qquad (18)$$

The value of k producing the lowest SSE for the angle calibration was used. The values used in this investigation varied from 0.09 to 0.45 depending on the particular probe being used.

With the values for A, B and C calculated, the next step was to perform a temperature calibration and solve for the temperature loading coefficient. This procedure consisted of taking a series of velocity measurements while the temperature of the airflow was varied. The temperatures used were selected to cover the range of expected temperatures. This process was repeated twice to include measurements of both high and low velocities at both high and low temperatures. The results of this calibration were compared to the values measured with the calibrator and the sum

33

squared error equation was again implemented using the previously determined value for k and varying the value of b. The value of b yielding the smallest sum squared error was used with values for the individual films ranging from -0.15 to 0.44.

With the values for these coefficients determined, the calibration was checked by measuring a fluid flow at known angles, velocities and temperatures. The results of this check showed the instrument to be accurate to within $\pm$ 0.25 degrees and $\pm$ 0.5 m/s as long as the temperature was maintained within a range of $\pm$ 2°C of the optimum. The center of this range depended on the particular probe. Deviations outside of this range produced progressively larger discrepancies, primarily in the angle measurements. These deviations increased slowly up to about 0.5° at $\pm$ 5°C of the optimum temperature.

The velocities and directions measured with the x-wire were relative to the a line bisecting the angle between the two wires. This velocity was then transformed into the cascade axis system by the data reduction software. A detailed explanation of these calculations may be found in Appendix C of DeCook's thesis (1991).

Pressure System Calibration

The PSI 8400 pressure measurement system was calibrated using an internal standard and an automated calibration process. This calibration took approximately three minutes and was performed prior to each data acquisition run. The PSI 8400 system uses piezoelectric pressure transducers which have definite and known

34

reactions to temperature changes. For this reason PSI Inc. recommends a re-calibration for any temperature change greater than 3°C. Since the temperature varied less than 3° during the data acquisition process, it was deemed unnecessary to compensate for this effect with a complete re-calibration. A quicker "re-zero" procedure was available and the data acquisition software was modified to implement it if a change in ambient temperature of more than 1.5°C occurred. The details of this process, along with those of the complete calibration procedure, may be found in the PSI 8400 Pressure Scanner User's Manual (1993).

Cascade Flow Conditions

Overview. The cascade test section was completely redesigned for this investigation. In light of this it was necessary to first establish the inlet and outlet flow conditions for the blade row. Once these conditions were known the data acquisition process was begun.

Inlet Flow Conditions. A survey of the throat was made with the hot-film probe to determine the throat velocity distribution and turbulence intensity. Turbulence intensity quantifies the magnitude of unsteady velocity fluctuations which are superimposed on the steady mean flow velocity. In this study, velocity fluctuations were measured in the cascade x-y plane (Figure 5) with an x-configuration hot-film probe.

Turbulence intensity (Tu) for one data point in a given measurement plane is defined as:

$$Tu \equiv \frac{\sqrt{\frac{1}{2}(\overline{v}_x^2 + \overline{v}_y^2)}}{\overline{V}} \qquad (19)$$

with

$$\overline{v}_x \equiv \sqrt{\frac{\sum_{j=1}^{L}(V_{x_j} - \overline{V}_x)^2}{L}} \qquad (20)$$

and

$$\overline{v}_y \equiv \sqrt{\frac{\sum_{j=1}^{L}(V_{y_j} - \overline{V}_y)^2}{L}} \qquad (21)$$

Where L was the number of samples taken at each data point, 100 for this investigation.

The survey was made with the test section removed, because the test section interfered with the hot-film probe, and revealed a slight skew to the velocity distribution. This skewness comprised velocities of about 1 m/s higher at the bottom of the throat than at the top. The mass averaged turbulence level was determined to be 0.68% and the mass averaged velocity was determined to be 135.6 m/s.

The next inlet condition to be evaluated was the periodicity of the static pressure distribution. This was measured with the test section in place and the straight trailing edge blades installed at each of the four flow incidence angles. The inlet periodicity was determined by scanning 23 static ports placed downstream of the suction slots and in front of the cascade inlet plane. These ports formed a row 0.05c in front of the leading edge of the blade row and were spaced at 0.46 cm intervals centered on the leading edge of the middle blade. The static pressure distribution was found to be periodic but was skewed with higher pressures near the cascade top and lower pressures near the bottom for each of the incidence angles (Figures 13, 14). As can be seen both the amplitude and the skew of the periodicity increase with increasing incidence angle. This increase in skew was likely due to increasing flow deflection caused by the increasing incidence angle. The lower pressure at the top of the cascade was not unexpected since this was the inside of the turn. These figures depict the inlet periodicity with the cascade tailboards balanced for a decreasing pressure distribution along their length and ambient pressure at the diffuser exit. Attempts to vary the tailboards to establish uniform periodicity across the inlet were never completely successful and resulted in a skewing of the pressure distribution in the exit planes (Figure 15). Uniformity of flow through the exit plane was later determined to be more critical than at the inlet so the tailboards were subsequently set to provide uniform exit plane periodicity. The determination of the tailboard balancing criteria

37

will be discussed later. For computations requiring inlet static pressure the nine static ports comprising one period and centered on the middle blade were monitored (Figure 16). An arithmetic average of these ports was used as the inlet static pressure.

The final aspect of the inlet flow conditions that was evaluated was the inlet total pressure. For this investigation the stilling chamber static pressure was considered to be the upstream total pressure and the corrections described below were made to this value.

The losses between the stilling chamber and the throat are small, but the end wall suction slots must be accounted for if an accurate evaluation of the total pressure losses is to be made. The measurement used to determine the suction losses was made with the test section in place and straight trailing edge blades mounted at the 4.49° incidence angle. The total pressure rake was used and placed so that it was about 0.05c in front of the blade row. This location was downstream of the endwall suction slots and even with the inlet static ports. The value of the inlet total pressure was taken to be the arithmetic average of the eleven total pressure readings taken by the rake and was found to be 99.85% of the stilling chamber pressure (P_{ink}). For all calculations in this investigation, the inlet total pressure was considered to be 0.9985 P_{ink}.

Exit Plane and Diffuser Conditions. With the inlet conditions established, it was necessary to evaluate the cascade exit conditions. The exit plane of the test section was evaluated for static pressure periodicity and general flow conditions. The diffuser

38

downstream of the cascade exit plane was also evaluated and the measurement window, measurement planes and measurement grid size were determined.

The static pressure periodicity was the first characteristic of the flow to be evaluated. The measurements were taken from a row of 23 sidewall static ports spaced at 0.46 mm intervals and centered on the trailing edge of the center blade. The row of ports was placed at 0.05c behind the trailing edge plane of the blade row. The measurements were made with straight trailing edge blades installed at an angle of 4.49° incidence. As mentioned earlier, exit plane static pressure was also periodic. In this case, however, there was little skew due to the procedures used to balance the tailboards (Figure 17). This uniformity in the periodicity of the exit static pressure is indicative of the uniformity of the flow distribution across the cascade exit plane. Nine static ports encompassing one period, and the measurement window discussed below, were monitored during each data acquisition run. The arithmetic average of the pressures from these nine ports were used as the exit plane static pressure (Figure 18).

With the periodicity evaluated, a series of five planes were scanned with the hot-film anemometer. These survey's were made with the blades installed at the 4.49° incidence angle and were used to determine the appropriate 'window' to scan during the data acquisition runs.

The planes that were surveyed were located at distances downstream of the cascade exit corresponding to the rows of sidewall static ports (0.05c, 0.30c, 0.56c, 0.96c, 1.37c) (Figure 8). Using these rows of static ports to determine the sampling

39

planes allowed the static pressure at each x location to be more accurately estimated. For the initial survey of each plane, static ports centered on the trailing edge of the center blade were arithmetically averaged to determine the static pressure used in the associated data reductions.

For these initial surveys a relatively coarse grid of 1.27 mm (0.05 in) spacing in the y direction and 2.79 mm (0.11 in) spacing in the z direction was used. Contour plots of the velocity and total pressure distributions were evaluated to determine an appropriate sampling window for all of the planes. As seen in Figures 19 and 20, the second and last sample planes, the blade wakes and associated vortices descend as they travel downstream from the blade exit plane. To compensate for this phenomenon the sampling window ranged from 121 mm above the y axis zero reference (the trailing edge of the center blade) to 216 mm below the zero reference. These distances correspond to one blade spacing and were chosen so that the window began and ended in the least disturbed airflow between the blades. The sampling window is plotted on the 0.30c and 1.37c contour plots (Figures 19, 20). The window chosen ensured that all wake turbulence and vortices came from the same blade.

With the size of the window chosen the grid spacing for the data acquisition runs needed to be determined. From the preliminary contour plots it could be seen that conditions changed much more rapidly in the pitchwise (y) direction than in the spanwise (z) direction. This indicated that the sampling grid should be as fine as practical in the pitch direction and could be coarser in the span direction. The total pressure rake spanned a distance of 381 mm (1.5 in) and had tubes at 38.1 mm (0.15

in) intervals. The hot-film sensor, on the other hand could be placed at much smaller intervals but could only scan an additional 0.5 mm (0.02 in) laterally. It was decided that the distance and spacing of the pressure rake would be adequate for the hot-wire as well. In the pitch direction a much finer grid of 0.25 mm (0.01 in) was used. With the thickness of the blade wake being approximately 2.5 mm (0.1 in) at the first sampling plane this spacing ensured that approximately 10 measurements were taken within the wake. While a finer grid would have provided more resolution, the time required to make a scan of the window would have been excessive. The grid size chosen was the same for the hot-film sensor and the pressure rake and resulted in 1474 points being sampled for each window surveyed.

Data Acquisition

Tailboard Balancing. Prior to the first run for each configuration the tailboards were balanced (Figure 8). This was necessary because of the different flow deflection angles dictated by the different throat sections. The two primary considerations in balancing the tailboards were ensuring the diffuser exit pressure was equal to ambient and ensuring that the top and bottom tailboards had the same pressure distribution. Since it was desired to have ambient pressure at the exit plane of the diffuser, the pressure at the exit plane of the blade row varied with flow deflection angle. In all cases the tailboards were balanced to achieve 0 ± 0.09 psig at the diffuser exit and 0 ± 0.09 psid between top and bottom. This resulted in blade row exit pressures of

41

0.047 to 0.083 psig depending on the particular configuration. These procedures also ensured the previously mentioned uniform pressure distribution across blade exit plane. The tailboards were balanced with the probe to be used, either the pressure rake or the hot-film sensor, installed in the cascade.

Probe Alignment. The procedure for aligning each of these devices was the same. Each was centered spanwise behind the center blade of the test section and the reference point of the traversing mechanism was set to zero. The spanwise alignment process required the removal of the sidewall and the tailboards had to be balanced after it was completed. The pitchwise alignment was made with the tailboards in place and the airflow turned on. The precision with which the devices could be aligned was ± 0.13 mm (0.005 in). An additional alignment check was made for the hot-film to ensure that it was aligned with the cascade x axis. This check was made with the flow on and any corrections for misalignment were made to the reduced data.

Static Pressure Collection. For data collection runs all pressures were read into the data acquisition computer from the PSI 8400. The raw data received by the data acquisition computer was pressure (psid) readings. The reading for each port was the arithmetic average of 11 samples taken over a period of 0.053 seconds. As mentioned previously, the inlet and exit static pressures were the arithmetic average of nine static pressure ports. These readings were averaged when they were received, and the value recorded in the data file for each data point was the arithmetic average of the nine ports. The stilling chamber static pressure was read directly into the data file.

The PSI 8400 system measures differential pressures using either 1.0 or 5.0 psid transducers. Each pressure reading passed on to the computer was the arithmetic average of eleven samples taken at 208 Hz. Since these are differential pressures, a reference pressure was required against which to measure the differences. The reference pressure chosen for this investigation was ambient pressure. The ambient pressure was measured by the digital barometer described in the previous chapter and was monitored directly by the data acquisition computer. This arrangement provided the computer with an ambient pressure reading for each physical data point. (A series of test runs made with varying ambient pressure were made. These runs showed that all measured pressures tracked with ambient pressure, validating the choice of ambient pressure as a reference. The details of this test are outlined in Appendix C.

Temperature Collection. The thermocouples monitoring the stilling chamber and ambient temperatures were read each time a data point is taken. At each physical point the temperature was read from the thermocouples and written to the data file as a voltage. These voltages were then translated into temperatures during data reduction.

Total Pressure Rake. With the tailboards balanced and the pressure rake aligned the rest of the data acquisition process was automated. The airflow was turned on and the tank and ambient temperatures were allowed to stabilize. With the initiation of the data collection run the computer positioned the traversing mechanism at the highest point of the traverse. For the pressure rake all data runs were made using a vertical traverse with the rake aligned with the span of the blades. At each point of the

43

traverse the readings from each of the eleven total pressure tubes were read from the PSI 8400. If the change in pressure from one point to the next resulted in a change of more than 0.02 psid for any of the eleven tubes, that point was re-taken for all them. This process was repeated until all tubes showed a change in pressure of less than 0.02 psid for two consecutive samples. All eleven pressures were recorded simultaneously. The previously mentioned grid spacing resulted in 134 vertical points being taken to cover the survey window and took from 7 to 25 minutes for each measurement plane.

Hot-film Anemometer. The data acquisition process for the hot-film was also automated but used a slightly different scanning pattern. In this case it was necessary to traverse in the span direction as well as the pitch direction. This difference required that the probe be repositioned for each of the 1474 data points and caused significantly longer run times. These longer run times and the sensitivity of the hot-film to temperature changes made it necessary to actively control the stilling chamber temperature. This was done using a combination of outside and inside air and the temperature in the stilling chamber was maintained within the four degree (C) range for which the hot-film produced the most accurate results. At each point scanned, 100 samples of the hot-film voltages were taken at a rate of 10,000 Hz. The arithmetic average of the 100 samples as well as the rms value for each film voltage was recorded along with the pressure and temperature data at each point. These quantities were written to data files for subsequent data reduction.

44

<u>Blade Pressures</u>. The pressure distribution around the center blade was scanned
for each blade geometry at each of the incidence angles at which it was tested. These
pressures were measured using the PSI 8400 attached to the blade surface pressure
ports.

Data Reduction

The parameters desired from the acquired data fall into two categories. The first
is the channel flow quality which is quantified by the $AVDR$, turbulence and velocity
distribution. The second category includes the parameters indicative of blade
performance. This category includes the pressure loss coefficient (ω), the cascade
deflection angle (ε), the wake velocity variance (σ^2), the wake velocity deficit (WVD),
the channel static pressure rise coefficient (C_p) and the blade static pressure coefficient
(C_p). The procedures used to determine these parameters consisted of two steps. The
first step was to convert the raw voltages from the hot-film and the thermocouples into
velocities and temperatures for each of the data points collected. The second part of
the data reduction process was to manipulate these discrete data points to determine
average or mass averaged values representative of the flow properties through the
channel as a whole. The following sections delineate the fundamental equations used
in this process.

The initial reduction of the raw voltages from the thermocouples is accomplished
using standard procedures. The reduction of the hot-film voltages into velocities and
angles at each discrete point follows the same process outlined in the calibration

45

section except that in the reduction program the previously determined coefficients are used compute the unknown flow direction and velocity. As mentioned previously a detailed explanation of the reduction of the voltages and the translation of the resulting velocities into the cascade axis system is available in DeCook's thesis (1991). This first data reduction step also computed the difference between the inlet and local total pressures for the pressure rake runs. The remainder of the data reduction is significantly different for the two probe types. The reduction equations for each will therefore be treated separately.

   Total Pressure Rake Data Reduction. In this investigation the pressure loss coefficient was the only reported quantity that used the measurements taken by the total pressure rake. The total pressure rake, due to its nature, provides a direct reading of the total pressure at discrete locations. Equation (4) was used to calculate the local pressure loss coefficient. In this equation, the quantity $(P_{oI} - P_{a2})$ was the quantity computed in the first reduction step where P_{a2} was the local total pressure measured by a single tube. The value for P_{oI} was the inlet total pressure and equal to 0.9985 P_{at}.

46

The value for ρ_1 was calculated using the following equation:

$$\rho_1 = \frac{P_1}{RT_1} \qquad (22)$$

The value for p_1 is the arithmetic average of the sidewall static pressure port readings for the inlet plane and T_1 is calculated from the following equation:

$$T_1 = T_{tnk} \left(\frac{p_1}{P_{01}} \right)^{\frac{(\gamma-1)}{\gamma}} \qquad (23)$$

The velocity used in Equation (4) was computed using the total enthalpy relationship:

$$V_1^2 = 2R \left(\frac{\gamma}{\gamma-1} \right) (T_{tnk} - T_1) \qquad (24)$$

Values for V_1 ranged from 139.1 m/s to 141.5 m/s.

After the pressure loss coefficient was computed for each point the values were mass averaged for the channel as a whole. The mass averaging was accomplished as outlined in Chapter II (Equation 7) with A_j replaced by ω_j. The value for ρ_2 is calculated with:

$$\rho_2 = \frac{P_2}{RT_2} \qquad (25)$$

Where p_2 was the arithmetic average of the nine exit plane sidewall static pressures.

47

The value for T_2 was calculated with:

$$T_2 = T_{tnk} \left(\frac{P_2}{P_{02}} \right)^{\frac{(\gamma - 1)}{\gamma}} \qquad \qquad \textbf{(26)}$$

The velocity used for mass averaging in Equation (7) was the x-component of the velocity for that point measured by the hot-film. This velocity was read in from the reduced hot-film data file and required that the hot-film run be made prior to the pressure rake data reduction.

Hot-film Data Reduction. The remainder of the performance and flow quality parameters were calculated from data acquired with the hot-film anemometer. With the initial reduction complete, the equations outlined in Chapter II were implemented. This process is outlined below.

The flow deflection angle calculated for each point in the first data reduction step was next mass averaged to find the flow deflection angle for the channel as a whole. This was done using the same method used for the pressure loss coefficient with ε_i inserted for A_j in Equation (7).

The wake velocity variance was calculated using Equation (13). The grid size chosen for this investigation set the value for n at 1474. The values for the other parameters were computed as outlined above. As explained in Chapter II, the velocity variance is a mass averaged value and a measure of the uniformity of the flow downstream of the blade row.

48

The wake velocity deficit is another indication of the uniformity of the flow in the wake region. It was calculated using Equation (8) from Chapter II. The freestream velocity was taken to be the arithmetic average of the top 25 percent of the velocities recorded in the plane being sampled. An examination of the velocity distribution for the middle three blades shows large areas of relatively constant freestream velocity (Figure 19). These large areas of near constant velocity validate the assumption that the top 25 percent of the measured velocities represent the freestream value. The mass averaged value for the axial velocity in this plane was calculated using Equation (7).

The static pressure rise was evaluated by calculating a static pressure coefficient using Equation (3). In this equation p is the downstream static pressure that was recorded for the plane being sampled. The other quantities are the inlet values computed as detailed above.

The blade pressure coefficients were the last performance parameter that were evaluated. The data for these distributions were gathered with a separate program. The blade C_p was also calculated using Equation (3). In this case p is the static pressure measured at points along the center span of the blade surface. The other quantities were calculated as previously described. This C_p was calculated for each static port on the blade surface and was plotted against non-dimensionalized distance as a distribution along the blade.

49

The last parameter to be determined from the hot-film data was a flow quality parameter, *AVDR*. This parameter was calculated using Equation (2). The quantities ρ_2 and V_{x_2} were computed from the midspan (z=0) data taken during each run. The calculation of these quantities used Equation (25) to calculate the density. The x-component of the downstream velocity was calculated from the angle and velocity data computed during the first step of the reduction process. This yielded 134 data points ($n = 134$) in the downstream plane being scanned. The upstream data (subscript 1) was calculated as previously described. This method of determining the upstream quantities was used because direct measurement of the upstream conditions was not possible with the blades in place.

Error Analysis

Equipment Accuracies. The manufacturer specified accuracies for the various pieces of data acquisition equipment are discussed in Appendix D. The errors resulting from these inaccuracies are calculated in Appendix D and summarized below in Table 5.

50

Table 5: Estimated Equipment Errors

Parameter	Expected Error (%)
ω	2
Blade C_p	2
Exit Plane C_p	2
WVD	3
Velocity Variance	1
AVDR	1

Repeatability

The results of this study were validated by conducting repeat test runs. These repeat runs were normally made at the x/c = 0.05 measurement plane. This location was chosen since it was determined to be the most sensitive to changes in either cascade conditions or instrument alignment and calibration. Before a repeat run was made, the cascade blower was turned off and the system allowed to blow down. In

51

most cases the repeat run was made approximately eight hours after the initial run at that location. In some cases the repeat run was made on the day following the initial run with the system having been shut down for several hours.

A repeat run was considered to validate the initial results if the repeated run yielded results which differed from the initial results by no more than the estimated errors listed in Table 5. If the repeat run did not corroborate the initial results, then another repeat run was made at the $x/c = 0.56$ measurement plane. If this run also failed to corroborate the initial results, the cause of the different results was investigated and corrected. Following this investigation, the data acquisition process was repeated in its entirety.

IV Discussion of Results

Introduction

This investigation examined four trailing edge crenulation geometries and determined their performance relative to uncrenulated blades as well as each other. The blade geometries are numbered as depicted in Figure 2. As mentioned previously, all blades were tested at an incidence angle of 4.49° which yielded anangle of attack of 23.5°. The results of the tests fell into two categories. The first was how each geometry interacted with the three-dimensional flows in the cascade. The other was the impact of each geometry on cascade performance. The results are discussed in the following sections.

Effects on Cascade Flow Conditions

Axial Velocity Density Ratio. As mentioned in chapter II, the *AVDR* provides an indication of the two-dimensionality of the flow. This parameter must be compared with some form of flow visualization, since it does not reflect concentrated areas of vorticity. The flow visualization used in this investigation comprised contour plots of velocity and pressure loss coefficient. These plots were generated from the data acquired by the hotfilm and pressure rake respectively.

53

The *AVDR* was evaluated by plotting its value for each crenulation geometry against downstream distance (Figure 21). As seen in Figure 21, the values were virtually the same for all geometries when the error bars are taken into account. These values are also well within the 0.8 to 1.2 range proposed by Klein for *quasi-two-dimensional* flow (Klein, 1977:489). The next step was to examine the velocity contour plots for three-dimensional flows.

The velocity contour plots for the straight blades showed distinct regions of low velocity near the sides of the passage (Figure 22). The other geometries had additional regions of low velocity associated with the crenulations (Figures 23-25). For all of the geometries, the most intense regions of low velocity were near the sidewalls. These strong three-dimensional flows make the validity of the *AVDR* questionable, at least as it was measured and computed in this investigation.

The main point to be taken from the above discussion is that while the *AVDR* indicated quasi-two-dimensional flow, there were strong three-dimensional effects apparent in the low velocity regions near the sidewalls. These regions, apparent in all configurations, were a product of the solid wall nature of this cascade. It is the details of the interaction between these regions and those of the trailing edge crenulations that is of particular interest in this investigation. The next section looks at each blade in turn to examine the impact of its crenulations on the flow in the passage.

Three-Dimensional Flows. The three-dimensional flows in a linear cascade were investigated by Kang and Hirsch (1991) using a linear cascade with physical parameters similar to those of the one used in the present cascade. Their investigation

54

determined the three-dimensional flow geometry to be as depicted in Figure 6, adapted from Kang and Hirsch (1991).

The similarities between the two cascades included equal aspect ratios, similar Reynolds numbers and no provisions for sidewall boundary layer control. These similarities indicate that the three-dimensional flows in the cascades may also be similar. Along with the similarities, there were some important differences between the cascades. These differences included a camber angle of 45° for Kang and Hirsch, as opposed to 30.51°, and served primarily to increase the loading on the blades in their cascade. In light of these differences, it was expected that some of the features of the flow structure depicted by Kang and Hirsch would be displaced and possibly harder to detect.

Straight Blades. To form a basis for reference, the velocity contour plots of the straight trailing edge blades were examined. Plots made at 0.05c downstream of the blade trailing edge were used for this purpose, since the velocity gradients close to the blade were easier to discern. This examination revealed distinct areas of low velocity downstream of the suction surface of the blade, the areas encompassed by the 60 m/s contours in Figure 22.a. These areas seemed to correspond to the passage vortex and possibly the concentrated shed vortex proposed by Kang and Hirsch (1991) and depicted in Figure 6.

Figure 6 depicts the approximate locations of the vortices shows how they would appear in a plane immediately behind the cascade exit plane. The corner vortices depicted in Figure 6 would not have been seen in Figure 22.a, since the hotfilm probe

55

could not be placed close enough to the sidewall. In order to try and locate these corner vortices, a survey with the pressure rake displaced to get as close as possible to the right (positive z) wall was examined (Figure 26). This plot showed areas of high ω likely caused by the corner vortices. Figure 26 depicts three blade wakes with triangular shaped areas of high ω associated with the corner vortices adjacent to the suction surface of each of the blades. These areas are seen to be distinctly separate from inner areas of high ω associated with the previously mentioned low velocity regions in Figure 22.a.

A closer examination of Figure 22.a revealed smaller areas of localized low velocity, labeled "A", within the areas enclosed by the 60 m/s contours. These may have been the concentrated shed vortices proposed by Kang and Hirsch (1991). The local velocity minimum is more visible on the right side of this plot, but a less pronounced area was also found on the left side. This latter region of low velocity was found by varying the plot's contour intervals to pick out intermediate contours. Another set of low minimum velocities, at about ± 1.52 cm, was also found. These were likely the passage vortices described by Kang and Hirsch (1991) and are marked as points "B" on the plot. The elongated areas of low velocity encompassing points "A" and "B" appeared to be the combined effect of these two vortices. (It may be noted that the wakes don't appear to be horizontal in the contour plots, this is due to the traversing mechanism being aligned slightly off the 'z' axis by about 2.8°).

If the three vortices on each side of the passage were rotating as depicted in Figure 6, the corner and passage vortices should have tended to rotate around each other as they travelled downstream. The concentrated shed vortices would also have tended to rotate around the passage vortices. If this was the case, the shape of the low velocity regions would change when successive downstream planes were examined. A comparison of the velocity contour plots for 0.05c and 1.37c seemed to show this happening (Figures 22.a, 22.b). The corner vortex seemed to move up slightly as seen by what appear to be the edges of it visible from about y = -0.16 cm to 0.24 cm in Figure 22.b (areas "C"). The passage vortex seemed to move lower with the center of the right one moving from -0.16 cm to about -0.76 cm in the pitch direction, area "A" in Figure 22.b. The concentrated shed vortices may be the elongated parts of areas "A" that extend slightly up into the middle of the passage, labeled areas "B". This movement is what would be expected from the interaction of the counter-rotating flows of the three vortices in Figure 6. Looking at the overall shape of the low velocity regions, Figure 22.b shows them to be longer in the pitch direction than the span direction. This is opposite to the situation immediately behind the blade (Figure 22.a). This change adds credence to the idea that these areas of low velocity may correspond to the vortices described by Kang and Hirsch (1991), and that the flow directions of individual vortices were at least partly responsible for the movement of these areas. These regions of low velocity constituted the most significant three-dimensional flows visible in the contour plots.

57

Large Crenulations (Blade 2). As is discussed below, the large crenulation geometry produced significantly better wake mixing than either the straight blades or the hole geometry. An examination of the interaction between the vortices it generated and the three-dimensional flows in the channel provided some insight as to why this may have been so.

A comparison of the 0.05c velocity plot for this geometry with that of the straight blades showed significant differences (Figures 22.a, 23.a). Where the straight blade had the elongated areas of low velocity, apparently caused by the passage and concentrated shed vortices, the large crenulation geometry had no similar areas. Instead this geometry had two distinct areas of low velocity further out from the walls at about ± 0.76 cm from centerline (Figure 23.a). These areas were both smaller, and less intense, with higher minimum velocity contours. As may be seen in Figures 22.a and 23.a, the minimum velocity contours were 75 m/s for Blade 2 as opposed to 45 m/s for straight blades. When these areas of low velocity were correlated with the placement of the crenulations, they were found to be located downstream of the solid portion of trailing edge. Figure 27 depicts the trailing edge of the large crenulated blade with its associated vortices. The areas of low velocity from the straight blades which are super-imposed on it will be discussed below. It appeared likely that the low velocity areas for blade 2 were the result of vortices generated by the high pressure air coming up through the crenulations.

58

This movement of the air up and through the crenulation seemed to move and/or diminish the passage vortices. The areas of low velocity associated with the straight blades were drawn on Figure 27 for reference. It seems that the vorticity generated by the crenulations displaced and diminished these areas of low velocity. A manipulation of the contour intervals showed two local minimums located in the approximate positions occupied by the passage vortices associated with the straight blades, areas "A" in Figure 23.a. These areas may have been the passage vortices, but were considerably less intense and were difficult to discern. Both the diminished passage vortices and the vortices generated by the crenulations were relatively weak.

A comparison of the 1.37c contour plot for Blade 2 with that of the straight blades, Figures 22.b and 23.b, shows the wake associated with Blade 2 to have dissipated slightly more than that of the straight blades. The contours of low velocity occupy more of the passage, for Blade 2, and have a slightly less regular structure. The contours associated with the straight blades, on the other hand, maintained their shape somewhat better, indicating less mixing. Though there are differences in the plots, the differences are much less noticeable at the 1.37c plane than immediately behind the blade.

The velocity contours depicted in both Figure 23.a and 23.b show the velocity gradients to be shallower and the minimum velocities to be higher, for Blade 2 than for the straight blades. This difference was also reflected in the graphs of wake velocity deficit and velocity variance (Figures 34, 35). These graphs showed the large crenulation geometry, along with the long narrow geometry, to be considerably better

59

at wake mixing than the other two. This improvement was the greatest at the 0.05c location and seemed to be due to the partial break-up, or displacement, of the passage and concentrated shed vortices by the crenulation generated vortices.

Long Narrow Crenulations (Blade 3). As mentioned above, the long narrow crenulation geometry produced wake mixing results similar to those of the large crenulation geometry (Figures 34, 35). The overall boundary of the blade wake was also similar between these two geometries. A detailed look at the contour plots of the blade wake, however, showed significant differences (Figures 24.a, 24.b).

For Blade 3, the areas of low velocity associated with the passage vortices were more apparent, areas "A" in Figure 24.a. In this case they were distorted and tended to merge with the outer two, of three areas of low velocity adjacent to the suction surface of the blade, areas "B" in Figure 24.a. The crenulated trailing edge of this blade was also plotted with the areas of low velocity from the straight blades superimposed (Figure 28). The locations of the crenulations correlated well with the positions of the three areas of low velocity adjacent to the suction side of the blade. These areas appeared to be vortices generated by the crenulations, areas "B" in Figure 24.a.

For Blade 3, the place where the passage vortex should have been was just below the solid part of the trailing edge, as opposed to just below a crenulation for Blade 2. This difference in crenulation location seemed to be at least partially

responsible for the difference in the size of the low velocity areas associated with the passage vortex. It is also likely that the larger size of the Blade 2 crenulations played a role in the dissipation and displacement of the passage vortices.

The similarity in performance between these two blades, as measured by wake mixing, was likely due to the similar velocity gradients and low minimum velocities within the blade wakes. This was particularly evident in the contour plots of the 0.05c sampling plane (Figure 24.a). The downstream plots, however, showed the vortices to be interacting somewhat differently for the long narrow crenulations.

While the vortices seemed to dissipate for Blade 2, the vortices for Blade 3 reacted differently depending on which side of the passage they started on. The vortices on the left side of the passage acted much like those of Blade 2. In this case it appears that the crenulation generated vortex and the passage vortex interacted in a way that dissipated both of them (Figures 24.a, 24.b). On the right side of the passage, however, these vortices seemed to remain more distinct with a more cohesive structure apparent at the 1.37c location. The reason for this difference is not clear.

While the details of the interactions between the passage vortices and those associated with the crenulations were not totally clear, Blade 3 was virtually the same as Blade 2 in terms of wake mixing. It was total pressure losses and turning angle, discussed below, that showed the long narrow crenulations to be better.

Hole Geometry (Blade 4). The velocity contour plots of the wake produced by this geometry looked a lot like that of the long narrow crenulations at first glance (Figures 25.a, 25.b). It had areas of low velocity at approximately the same locations,

61

areas "A" and "B" in Figure 25.a, and seemed to cover about the same amount of the passage. These low velocity areas were located downstream of the areas between the holes through the blade and were possibly due to vortices similar to those generated by crenulations. In this case, like that of the large crenulations, there were no discernable passage vortices. It looked like the passage vortices may have merged into the outer two low velocity areas just below the blade and near each wall, areas "A" in Figure 25.a. This may be the reason that these areas were wider than the one between the middle two holes, area "B". Another distinct difference was the steepness of the velocity gradients and the values of the lowest velocities. These gradients were much steeper and the velocities were much lower than those of Blade 3. These velocity gradients seemed to more than offset any benefit gained by the possible disruption of the passage vortex. This last fact may be seen in the *WVD* and velocity variance where this geometry had the worst overall performance of any blade tested (Figures 34, 35).

Turbulence Levels. The last aspect of the cascade flow conditions to be examined was the turbulence level. The plot of turbulence level against downstream position showed that each blade geometry produced essentially the same values, ranging from 1.68% to 1.93%. From this, it seems that crenulation geometry has little influence on the turbulence intensity for this incidence angle.

From this examination of the interactions between the crenulation geometries and the three-dimensional flow fields of the channel passage, it is apparent that the precise way in which the crenulations interacted with these flows had an impact on the

62

performance of the blades. The next step is to evaluate the cascade performance parameters and see how the crenulations affected them.

Performance Parameters

Total Pressure Losses. The pressure loss coefficient (ω) is a critical performance parameter. It reflects the losses in total pressure experienced in the cascade and provides a measure of the feasibility of each blade configuration. If the gains in wake mixing mentioned above were at the expense of large increases in total pressure losses, there would be little justification for using the crenulated blades. This was the case for the corner crenulations discussed in Appendix E, fortunately this wasn't always the case.

The total pressure losses were evaluated in two ways. The first was an examination of the pressure loss coefficient contours for each blade configuration, at each downstream sampling plane. The second was a comparison of the mass averaged pressure loss coefficient for each configuration at each downstream location.

Straight Blades. In evaluating the pressure loss coefficient it was logical to start with the straight blades. An examination of the ω contours revealed a situation much like that of the velocity contours (Figure 29.a). There were elongated areas of high ω corresponding the previously noted areas of low velocity, areas "A" in Figure 29.a. This is logical since the centers of the passage vortices indicated by the areas of low velocity would also be areas of low total pressure. These areas were seen to have

63

relatively high peak values of ω and steep gradients. As with the velocity contours, these concentrated areas dissipate as they travel downstream. An examination of the 1.37c contour plot showed the peak ω contours to have decreased from 0.75 near the blade (areas "A" in Figure 29.a), to about 0.35 (Figure 29.b).

Large Crenulations. The large crenulation geometry showed the same trends as the straight blades as the flow progressed downstream. Near the blade, however, the flow structure was again different. The biggest difference was that the peak values of ω were found in different locations, areas "A" in Figure 30.a. As with the straight blades, these areas of high ω corresponded to areas of low velocity. When compared, the peak values of ω for this geometry were slightly lower at about 0.45. These areas of high ω were also smaller and had flatter gradients for Blade 2, than for the straight blades. The dissipation of these areas between the 0.05c and 1.37c locations, however, was not as pronounced as for the straight blades. A result of this slower dissipation was identical values for the maximum contours at 1.37c, although the gradients for the straight blades were still steeper and moderately high contours reached further out into the passage. This is clearly seen if the areas encompassing values of ω greater than 0.2 are compared (Figures 29.b, 30.b). Overall, the large crenulation geometry appears to have more dispersed flow, and slightly lower values for ω, particularly near the blade. This would seem to indicate that Blade 2 would have a slightly lower mass averaged ω.

Long Narrow Crenulations. Blade 3 also had flatter gradients and lower maximum values of ω. This is readily apparent in the contour plots of ω (Figures 31.a, 31.b). In Figure 31.a, areas "A" and "B" are the local maximums of ω. Areas "A" are enclosed by contours with a value of 0.6 while area "B" is enclosed by a contour of 0.45. All of these areas are noticeably smaller in size than areas "A" of Figure 29.a, which were enclosed by contours with a value of 0.75. In addition, the percentage of the passage taken up by areas of even moderately higher ω appeared to be less than that for the straight blades, and slightly less than that for Blade 2. The rate at which these areas dissipated, on the other hand, was similar to Blade 2. The plot of the 1.37c plane, showed that the maximum values for ω weren't much lower, although the areas encompassing moderately higher values of ω were somewhat smaller. As before, this is seen if areas encompassing values of ω greater than 0.2 are compared (Figures 29.b, 30.b, 31.b). Overall, it would be expected for Blade 3 to have a mass averaged value of ω less than that of the straight blades.

Hole Geometry. The hole geometry produced ω contours superficially similar to those of the long narrow crenulation geometry (Figures 32.a, 32.b). When the steepness of the gradients and the size of the maximum values were evaluated, however, this geometry was seen to be more like that of the straight blades. The peak values of ω were just as high, but were located nearer the edges of the passage. The contours enclosing values of ω greater than 0.6 encompassed almost as much of the passage as those for the straight blades (Figure 32.a). The biggest difference between them was the division of these contours into three slightly smaller areas as opposed to

65

one large area spanning the passage. It would be expected for these areas to produce mass averaged values similar to those of the straight blades.

Mass Averaged ω. The mass averaged values of ω were plotted against downstream distance for all crenulation geometries (Figure 33). Also depicted on this graph are the error bars indicating the 2% range of values expected from the equipment. This graph bears out most of the observations made above with the possible exception of those of the large crenulation geometry.

The Blade 2 produced values of ω essentially the same as for the straight blades. This seems a little odd in light of the differences in the contour plots noted above. The discrepancy is most likely due to the weighting given the high ω areas by the mass averaging. For Blade 2 the hotfilm values for the velocity may have given more weight to the areas of high ω than for similar areas from the straight blades, which had lower velocities and took up less of the passage. When mass averaged, these lower velocities and smaller areas would tend to off-set the higher values of ω associated with them. In light of the apparent dissipation of the passage vortices, the higher mass averaged ω was not expected. One conclusion may be that the break-up of the passage vortices was made at the expense of total pressure. The long narrow crenulations, on the other hand, didn't seem to break up the passage vortices and produced lower total pressure losses.

In line with the analysis of the contour plots, the mass averaged ω is lower for the long narrow crenulations than the other geometries at all downstream locations. While there was a very slight overlap of the error bars for this and the straight

66

geometries at the 0.05c and 0.56c locations, the values for the long narrow crenulation geometry are most likely lower than those of the straight blades. The reason for this lower mass averaged ω, given the similarity in contour plots between this and Blade 2, is not entirely clear. A possible explanation may be that the areas of higher ω produced by Blade 3 encompass slightly less of the passage than do those of Blade 2. This fact along with similar low values for ω in these areas may be the reason for the reduction in the mass averaged ω. This slight reduction in total pressure losses makes the long narrow geometry an apparent improvement over the straight blades. The final determination will depend on the other performance parameters.

The hole geometry produced disappointing results and looked much as expected with values of ω slightly higher than any of the other geometries. This was evidenced by the relatively large areas of high ω seen in the contour plots. On the basis of this factor alone, this geometry is not a good candidate for future investigations.

Wake Mixing

As mentioned above, the wake mixing characteristics of the blades were evaluated using two parameters, the outlet velocity deficit and the wake velocity variance. These two parameters showed the long narrow crenulation and the large crenulation geometries to have distinct advantages over both the hole geometry and the straight blades (Figures 34, 35). In fact both of the former geometries produced almost the same results. The hole geometry, on the other hand, was worse than even the straight blades when these parameters were evaluated.

Blade C_p and Cascade Turning Angle

The blade C_p is a parameter which indicates the lift of the blade and hence the ability of the cascade to turn the flow. This parameter is presented as a non-dimensional pressure distribution along each of the blade's surfaces. The C_p distribution for each crenulation geometry is plotted along with that of the straight blades in Figures 36, 38 and 39. The area between the two series of points reflects the lift generated by the blade.

The cascade turning angle was effectively the flow deflection angle (ε). This parameter confirmed the long narrow geometry as better than the large crenulation geometry. The flow turning angle for each of the geometries is plotted, with error bars indicating the accuracy of the measurements, in Figure 40. The following sections evaluate each geometry's performance using both C_p and turning angle.

Large Crenulation Geometry. The large crenulation geometry appeared to have a distribution along the suction surface that was much like that of the straight blades (Figure 36). The only difference was a slightly smaller suction peak near the leading edge of the blade. The pressure surface depicted a more pronounced difference. In this case the pressure distribution started off slightly lower, than that of the straight blades, and the difference gradually increased for the first 60% of the blade. After this point, however, there was a rapid drop in pressure. This rapid drop was probably due to the large crenulation located at the midspan location. It should be noted that this geometry was the only one with a crenulation in this position, and that because of it the blade ends at about 0.75c at mid-span. The rapid drop in pressure near the

68

trailing edge along with the generally lower pressure on the pressure surface indicate that this geometry should produce less lift, and hence less turning, than straight blades.

The reduced turning produced by Blade 2 is readily apparent in Figure 40. The difference with respect to the straight blades ranged from about 3° near the blade to about 2.3° at the 1.37c location. This reduction in turning angle would require the blade to be placed at a higher incidence angle in order for it to yield as much turning as the straight blades. This higher incidence would increase the total pressure losses which would offset the improvements in wake mixing.

Long Narrow Crenulations. The long narrow crenulations produced a C_p distribution much like that of the large crenulations. This is apparent in Figure 37 which depicts both of these plotted together. Figure 38, meanwhile, shows the long narrow crenulations compared with the straight blades. This geometry produced a pressure difference on suction surface virtually identical to that of the Blade 2. On the pressure surface, however, there is some difference. The long narrow crenulations produced pressures slightly lower than those of either the large crenulations or the straight blades. The drop off in pressure at the trailing edge, on the other hand, was not quite a severe as that of the large crenulations. These differences between the long narrow crenulations and the large crenulations may be due to the fact that there is no crenulation at the mid-span for the former. If there was, the pressure distributions may have looked the same. When compared with the straight blades, it was thought likely that the lower pressures on the pressure surface would cause the long narrow crenulations to produce less turning.

69

This loss is seen in Figure 40 where differences ranged from about 1.9° at 0.05c to about 1.2° at 1.37c. These losses in turning angle are much less than those for the large crenulations. This is somewhat unexpected given the C_p distributions. These distributions were taken at the center span, however, and may not reflect the lift generated by crenulated blades as well as they reflect the lift generated by straight blades. It is also possible that the greater amount of blade area removed in making the large crenulations may have a larger influence on the turning produced by those blades than the C_p distribution indicates. This latter point is examined more carefully below. The wake mixing characteristics of Blades 2 and 3, on the other hand, were almost identical. Additionally, the better ω for the long narrow crenulations leaves room for it to rise if the incidence angle is increased to produce the turning angle of the straight blades.

Hole Geometry. The hole geometry produced a C_p distribution very much the same as that of the straight blades (Figure 39). The only significant difference is seen on the pressure surface after about 0.50c. In this case there is a slight drop, but much less than that of either Blades 2 or 3. The turning angle produced by this geometry was much nearer to that of the straight blades was more in line with the blade C_p distributions. With losses in turning angle ranging from about 1.1° to 0.5°, this geometry came the closest to the performance attained by the straight blades. The other performance parameters, however, showed no advantages for this geometry.

Loss of Blade Area

In the crenulation design phase of this investigation, it was thought that the blade area near the trailing edges lost to crenulations might have been partly responsible for the loss of flow deflection found in DeCook's investigation (1991). In order to investigate this possibility, the amount of blade area lost to the crenulations was calculated for each geometry. This area was then divided by the area of the blade and plotted against the turning angle (Figure 41). As can be seen in the graph there does appear to be a trend of decreasing flow deflection with decreasing blade area. This information is used in the next chapter when recommendations for future research are made.

Static Pressure Rise (C_p)

The last performance parameter considered is the non-dimensional static pressure rise. The exit C_p for each geometry is plotted against downstream location in Figure 42. In this case the hole geometry and the large crenulation geometry had essentially the same characteristics. The straight blade and the long narrow crenulation geometries were slightly different from each other and were higher than either of the other two. When the error bars are taken into consideration, the actual values for all of the geometries are likely very close. The only conclusion which may be drawn from this parameter is that the static pressure rise produced by the long narrow crenulations is the close to that of the straight blades. The static pressure rise of the

71

other two configurations are the same and possibly somewhat less. This parameter appears to confirm the earlier determination of the long narrow crenulations being better than the other two crenulation geometries, but worse than the straight blades.

Summary

The results discussed above show that while the long narrow crenulation geometry lost 2° of flow turning, it produced the best performance of the crenulated blades. The large crenulations, meanwhile, yielded good wake mixing but suffered from a greater loss of flow turning. Finally, the hole geometry produced virtually no improvements over the straight trailing edge blades. The conclusions arrived at from these results and recommendations for future investigations are discussed in the next chapter.

VI. Conclusions and Recommendations

Conclusions

From the results discussed in the previous chapter, it is evident that crenulations on the trailing edge of blades in a linear cascade can increase the rate of wake dissipation. It is also apparent that the geometry of the crenulations have a direct impact on the manner and effectiveness of the wake dissipation.

Of the geometries tested, both Blade 2, the large crenulation geometry, and Blade 3, the long narrow crenulation geometry, produced better wake mixing than the straight blades. The manner in which the wakes were dissipated seemed to be different, and depended on the interaction between the crenulation generated vortices and the three-dimensional flows present in the passage. Blade 2 seemed to produce the enhanced wake mixing by either dissipating or displacing the passage and concentrated shed vortices. Blade 3, on the other hand, seemed to produce the enhanced wake mixing by reducing the strength of these vortices with more moderate changes in the flow structure. This difference in the manner in which three-dimensional flows were affected by the crenulations appeared to impact the total pressure losses generated by a particular geometry. The manner in which Blade 3 reduced the strength of the vortices allowed it to produce lower total pressure losses

73

than Blade 2. The reason for this difference in total pressure losses is not entirely clear, but is likely due to greater losses associated with the large changes in the three-dimensional flow fields caused by the large crenulations.

Another relationship noted in the previous chapter was that between the amount of blade area removed in making the crenulations and the blades' ability to turn the flow. When larger amounts of blade area were removed, there seemed to be larger losses in flow deflection (Figure 41). In particular Blade 3 lost about 30% less flow deflection than Blade 2 while producing almost exactly the same amount of wake mixing. The loss in flow turning produced by both of the geometries is still excessive and appears to be the cost of the increased wake mixing.

Of the blades tested, the long narrow crenulation geometry produced the best results. It had the enhanced wake mixing characteristics of the large crenulation geometry while producing about 1° more turning. It was also the only geometry to produce lower total pressure losses than the straight blades. In spite of the advantages when compared with the large crenulation geometry, the long narrow geometry still has unacceptable losses in turning angle when compared with the straight blades. In order for the long narrow geometry to be considered better than straight blades, it would have to produce nearly the same amount of flow turning. This can be accomplished with an increase in incidence angle, but the increased incidence will lead to increased total pressure losses. The suitability of the long narrow crenulation geometry awaits testing to determine the magnitude of the increased total pressure losses.

74

Recommendations

The recommendations for further research fall into two categories. The first is recommendations concerning further research which should be conducted using the long narrow crenulation geometry of this investigation. The second is recommendations concerning designs attempting to improve on the performance of this geometry.

Further Investigations Using Blade 3. Further investigations into the performance of the long narrow crenulation geometry should center on two areas. The first is a closer investigation of the interaction between the crenulation generated vortices and the three-dimensional flow fields present in the passage. The second area of investigation should focus on the performance of these blades at different incidence angles.

Investigations into the interactions between the crenulation generated vortices and the three-dimensional flow fields should include a detailed survey of the wake region using a finer spanwise grid than that used in this investigation. This finer grid would allow more of the details of the flow field to be discerned. The best downstream locations for this survey appear to be the 0.05c and 0.30c planes used in this investigation. The close proximity of these planes to the trailing edge of the blade should make the flow interactions easier to discern. Another survey that should be included would be a survey of the spanwise flows in these two sampling planes. These spanwise surveys, when correlated with the pitchwise surveys, would provide a more complete picture of the flow field interactions. This comprehensive investigation

75

of the blade wake would allow better decisions to be made in the design of new crenulation geometries. Similar investigations of the large crenulation geometry might also be useful. If the causes of the increased total pressure losses could be determined, future designs could avoid reproducing them.

The other area of investigation that should be pursued with the long narrow crenulation geometry is the performance of these blades at the other incidence angles listed in Table 2. An investigation which ran concurrently with this one looked at the performance of the large crenulation geometry at these other incidence angles (Costello, 1993). Based on Costello's results, it seems likely that the long narrow crenulations will produce favorable performance at both increased and decreased incidence angles. This performance needs to be investigated and hopefully verified.

Optimization of Crenulation Geometry. The examination of the interaction between the crenulation generated vortices and the secondary flows in the passage showed the location of crenulations to be of particular importance (Chapter V and Appendix E). Additionally, the amount of blade area removed in making the crenulations should be minimized if the flow deflection angle is to be maintained. These two conclusions were kept in mind when the proposed blade geometries discussed below were conceived.

The first design attempts to regain some of the lost flow deflection by proposing the same number and depth for the crenulations, but only half of the width (Figure 43.a). This design would reduce by about half the amount of material removed, but would hopefully retain the wake mixing and total pressure losses of the

76

current long narrow design. The placement of the crenulations was deemed critical and the area of low velocity associated with the passage vortex should be between crenulations. This constraint may be met by placing the inner edges of the outer crenulations and the outer edges of the inner crenulations in the same locations as those of the current design. This placement was determined using Figures 22, 24, and 28, and attempts to make the same changes in the passage vortices as the current long narrow crenulations.

The next design uses the same philosophy of increasing the blade area over that of the long narrow crenulation. In this case, however, two crenulations of the same size are used with two crenulations with half of the width (Figure 43.b). The two outer crenulations would be the same size and be located in the same place as the current geometry. The two inner crenulations would have half the width and be placed with their outer edges at the same locations as those of the current inner crenulations. This design would have approximately 25 percent less blade area removed than the present long narrow crenualtions.

Another geometry would use three crenulations half as wide as the present long narrow geometry (Figure 43.c). These crenulations would be placed so that the inner edge of the outer crenulations are in the same place as inner edges of the current outer crenulations. This placement also attempts to produce changes in the passage vortices similar to those of the long narrow crenulations. The third crenulation would be placed at the midspan location. This geometry would have only about one third as much blade area removed as the current design.

77

The last proposed geometry is based on the same philosophy as those above. In this case the current long narrow geometry would be changed to leave only the two outer crenulations (Figure 43.d). These crenulations would hopefully produce the same positive effects on total pressure losses and wake mixing as the current design. This geometry would have half as much blade area removed as the present long narrow geometry.

Each of the designs proposed above has the potential to improve the flow turning while keeping most of the advantages of the present design. The additional tests of the current geometry recommended above would likely narrow down or possibly eliminate these proposals. If the equipment and software modifications needed to perform these tests are made, then these additional tests are the next logical step. Another option is to manufacture and test the new designs using the current software and equipment. This latter alternative would entail the least amount of set-up and would likely produce the quickest results.

References

Allison, Dennis M. Design and Evaluation of a cascade Test Facility. MS Thesis GAE/AA/81D-2. School of Engineering, Air Force Institute of Technology (AU), Wright-Patterson AFB, OH, June 1982.

Costello, Michael J. Off-Design Performance of Crenulated Blades in a Linear Compressor Cascade. MS Thesis GAE/ENY/93D-1. School of Engineering. Air Force Institute of Technology (AU), Wright-Patterson AFB OH, June 1989. (Unpublished Thesis).

DeCook, S.J., P.I. King and W.C. Elrod. "Wake Mixing and Performance of a Compressor Cascade with Crenulated Trailing Edges," Journal of Propulsion and Power, Volume 9, Number 2: 293-300 (March-April 1993).

DeCook, S.J. Experimental Investigation of Trailing Edge Crenulation Effects on Losses in a Compressor Cascade. MS Thesis GAE/ENY/91D-1. School of Engineering, Air Force Institute of Technology (AU), Wright-Patterson AFB OH, December 1991.

Dixon, S.J. Fluid Mechanics, Thermodynamics of Turbomachinery. Oxford: Pergamon Press, 1986.

Erwin, John R., and James C. Emery. Effect of Tunnel Configuration and testing Technique on Cascade Performance. NACA TN-2028. Washington: National Advisory Committee for Aeronautics, 1950.

Eschbach, Ovid W. and others. Handbook of Engineering Fundamentals. New York: John Wiley & Sons, 1975.

Freymuth, Peter. A Bibliography of Thermal Anemometry. St Paul, MN. TSI Incorporated, 1982.

Gostelow, J.P. Cascade Aerodynamics. Oxford: Pergamon Press, 1984.

Kang, Shun and Ch Hirsch. "Three Dimensional Flow in a Linear Compressor Cascade at Design Conditions," ASME Paper 91-GT-114, Orlando, FL, June 1991.

Klein, Armin and Norbert Scholz. Aerodynamics of Cascades. Neuilly sur Seine, France: Advisory Group for Aerospace Research and Development, 1977 (AGARD-AG-220).

Lieblein, Seymour. "Experimental Flow in Two-Dimensional Cascades", Aerodynamic Design of Axial Flow Compressors Revised, edited by Irving A. Johnson and Robert O. Bullock. NASA SP-36. Washington: National Aeronautics and Space Administration, 1965.

PSI 8400 Pressure Scanner User's Manual, Hampton VA: Pressure Systems, Incorporated, March 1993.

Tang, Y.P., F. Chen, M.Z. Chen. "Experimental Investigation of Vortex Structure in Corner Region of a Linear Compressor Cascade," ASME Paper 91-GT-158, Orlando, FL, June 1991.

Veesart, J.L. Wake Dissipation and Total Pressure Loss in a Two-Dimensional Compressor Cascade With Crenulated Trailing Edges. MS Thesis GAE/AA/89J-3. School of Engineering. Air Force Institute of Technology (AU), Wright-Patterson AFB OH, June 1989.

Wennerstrom, Arthur J. "Vane Configuration for Fluid Wake Re-energization", United States Patent Number 4,318,669 1982.

White, Frank M. Viscous Fluid Flow (Second Edition). New York: McGraw-Hill, Inc., 1991.
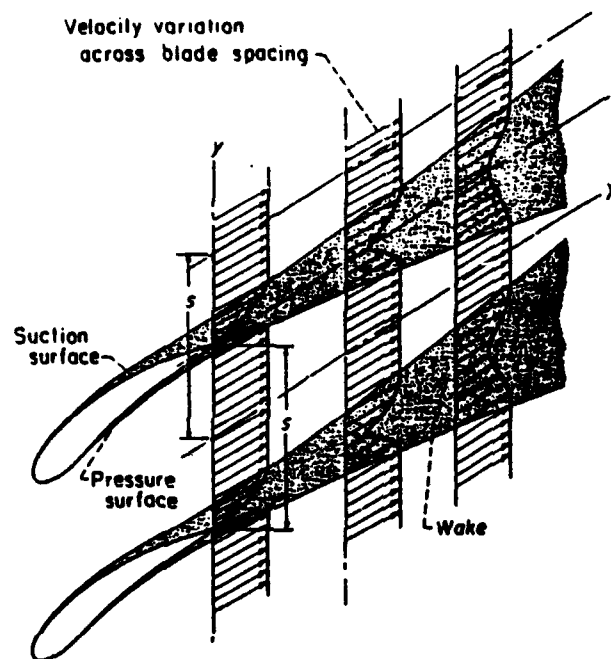
Figure 1. Blade Wakes

81
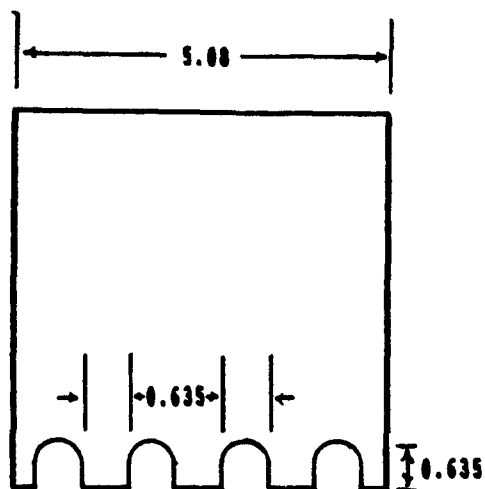
Figure 2.a.
Small Crenulation
Geometry
(Not Tested)
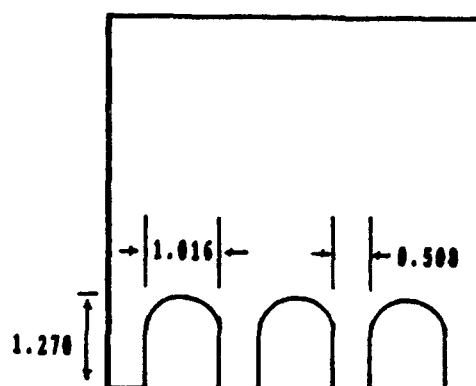
Figure 2.b.
Large Crenulation
Geometry
(Blade 2)
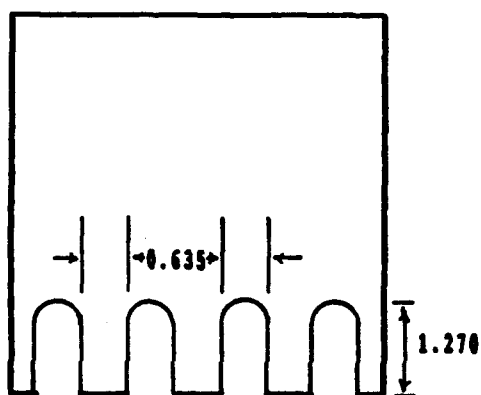
Figure 2.c.
Long Narrow Crenulation
Geometry
(Blade 3)
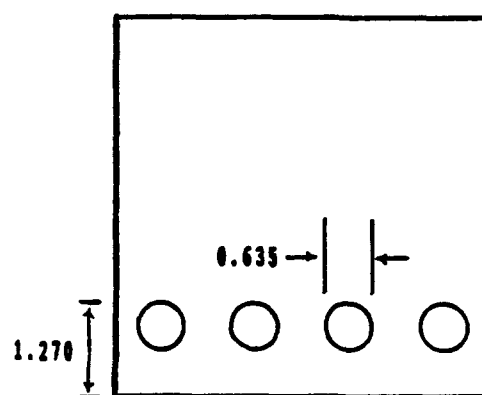
Figure 2.d.
Hole
Geometry
(Blade 4)
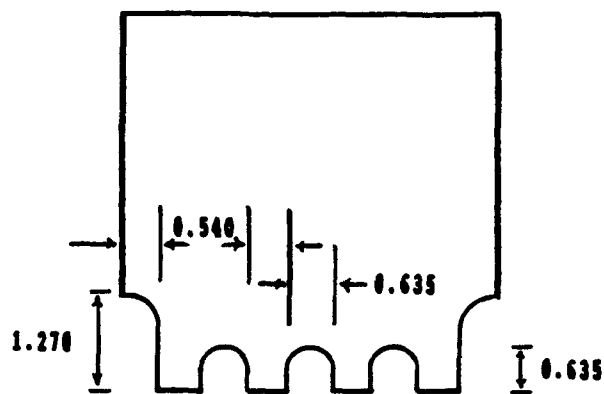
Figure 2.e.
Corner Crenulation
Geometry
(Blade 5)

82

Figure 3. Crenulation Generated Vortices

α_1' = blade inlet angle
α_2' = blade outlet angle
θ = blade camber angle
$\quad = \alpha_1' - \alpha_2'$
ζ = setting or stagger angle
s = pitch (or space)
ϵ = deflection
$\quad = \alpha_1 - \alpha_2$
α_1 = air inlet angle
α_2 = air outlet angle
V_1 = air inlet velocity
V_2 = air outlet velocity
i = incidence angle
$\quad = \alpha_1 - \alpha_1'$
δ = deviation angle
$\quad = \alpha_2 - \alpha_2'$
c = chord
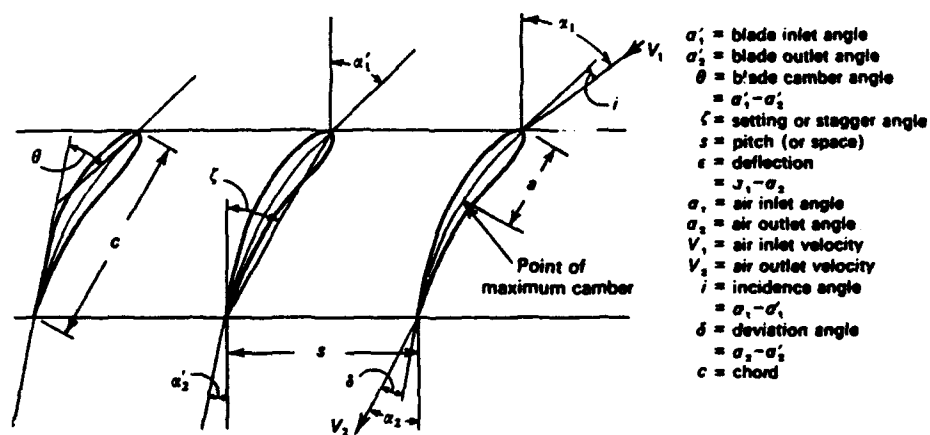
Figure 4. Cascade Nomenclature

83
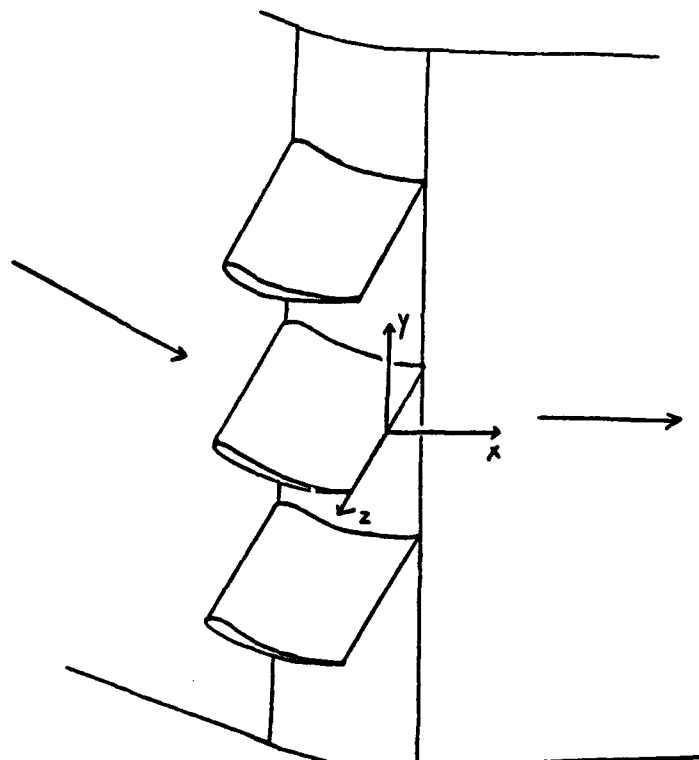
Figure 5. Cascade Coordinate System
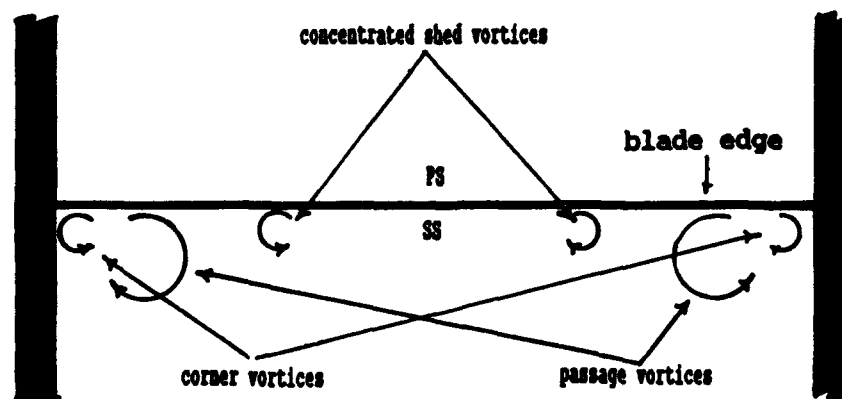
Figure 6. Cascade Vortices, (adapted from Kang and Hirsch, 1991)
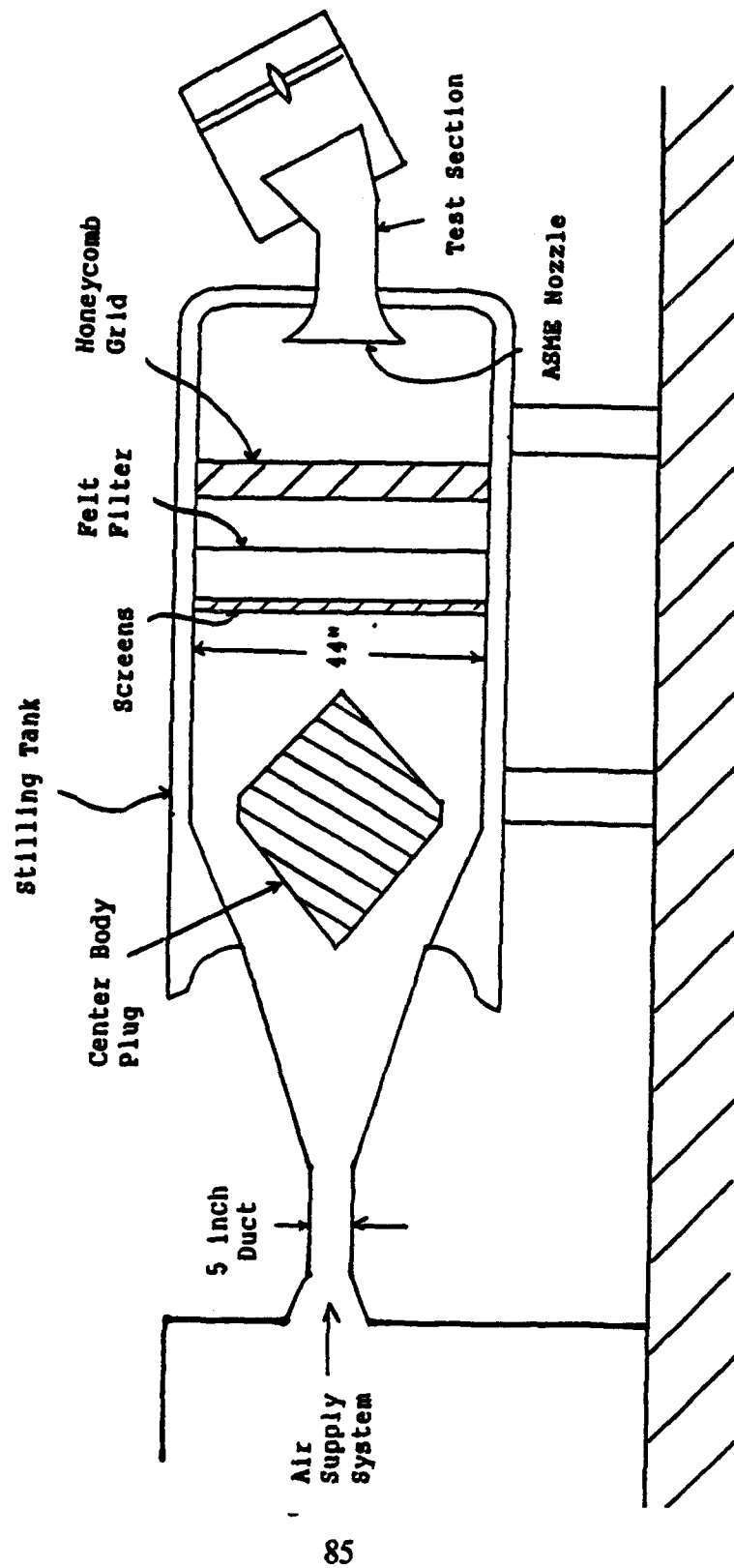
Figure 7. Air Supply System
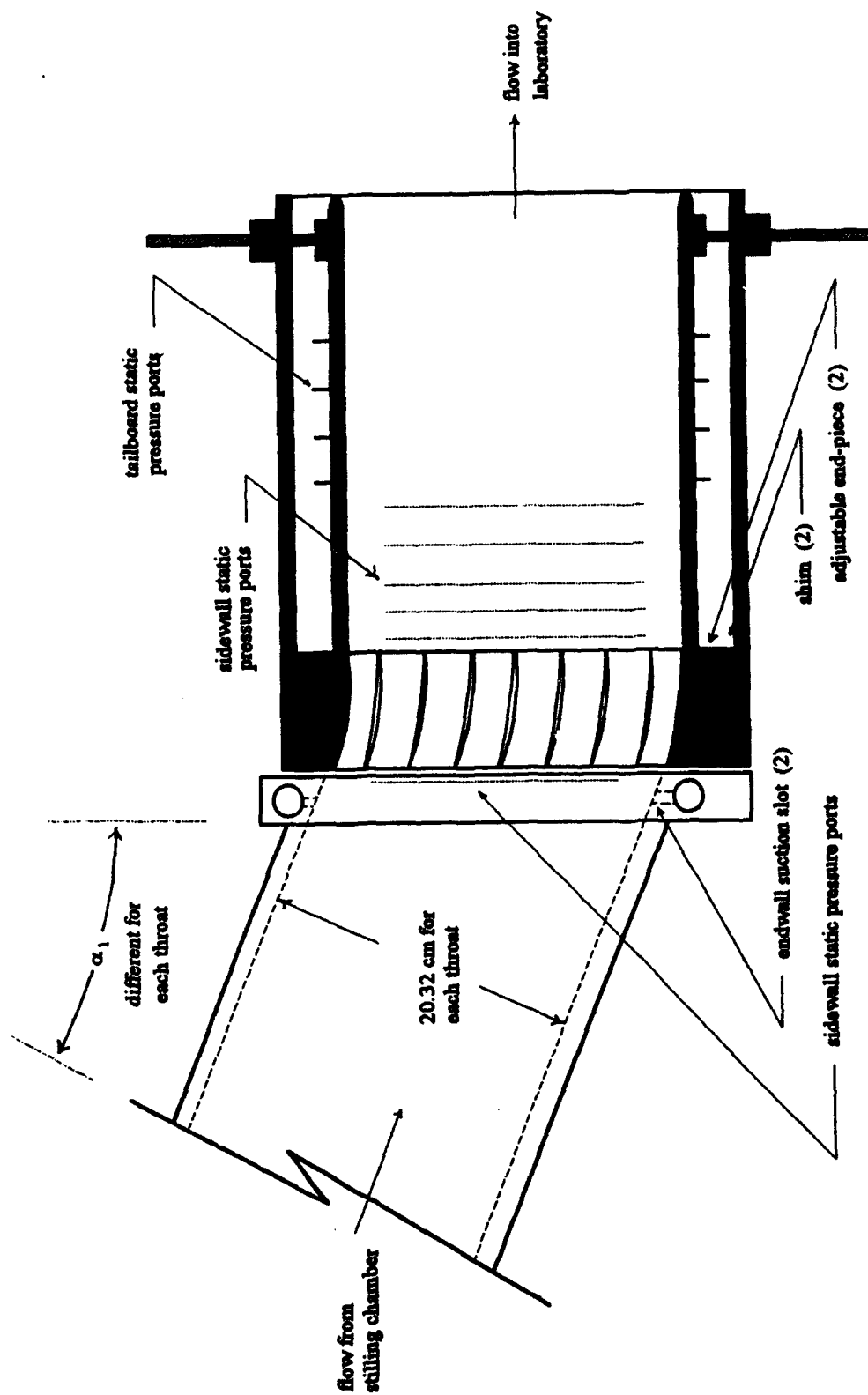
Figure 8. Cascade Test Section

86
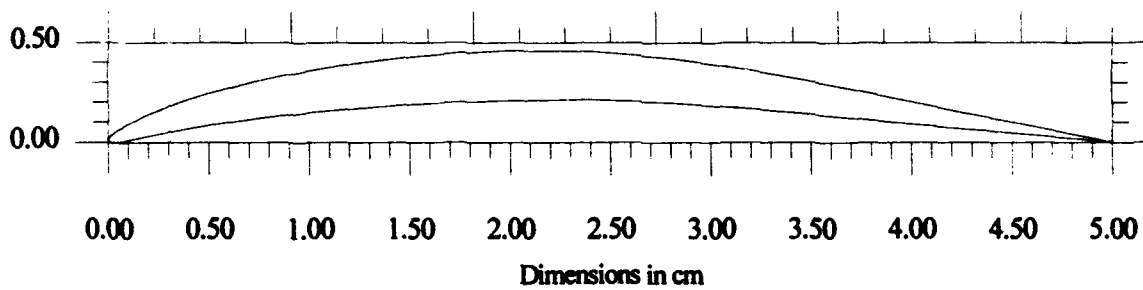
Figure 9. Compressor Blade Dimensions
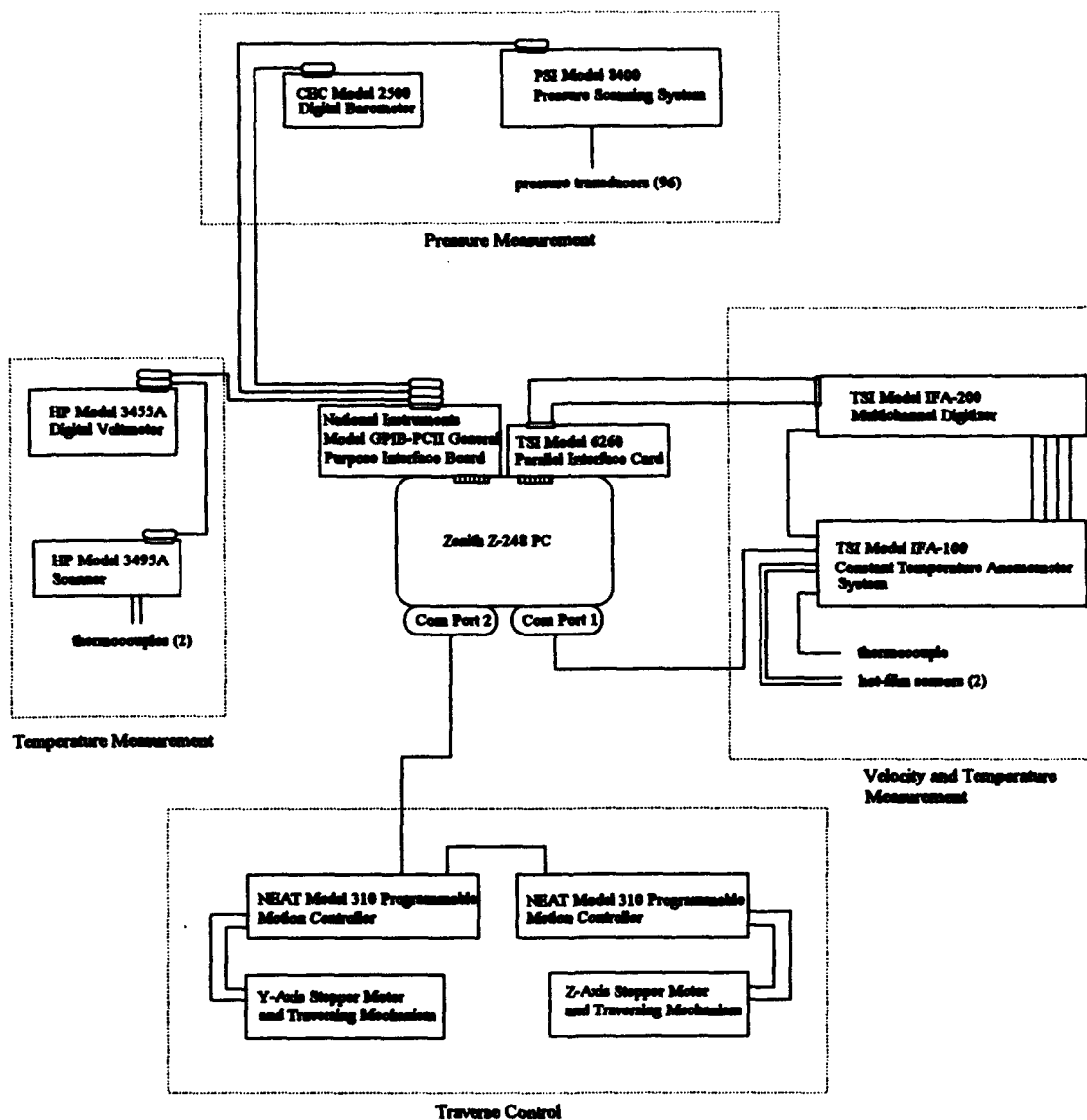
Figure 10. Digital Data Acquisition System

88

— 78.7 cm —
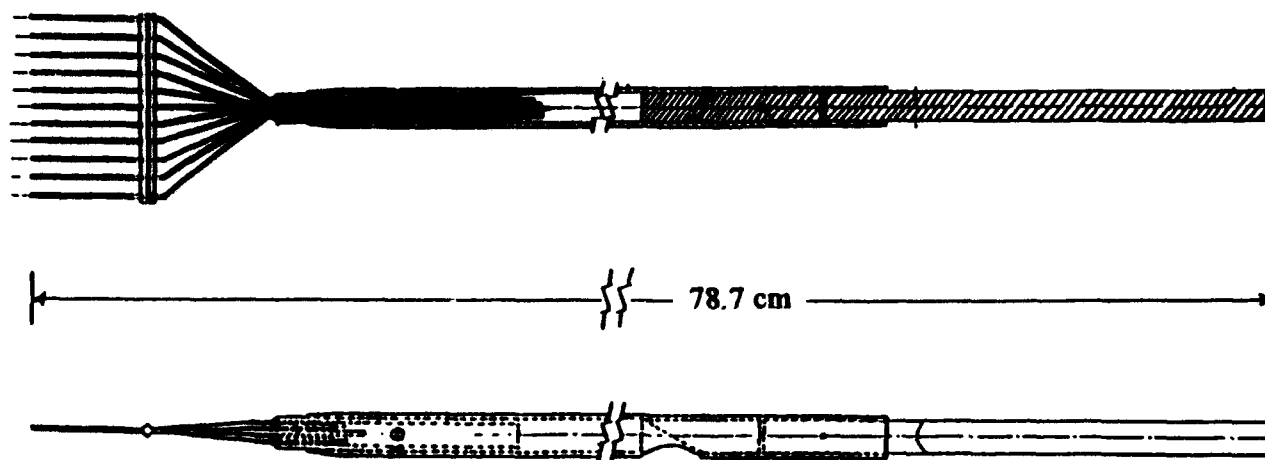
Figure 11. Total Pressure Rake

SENSOR #1
SENSOR #2
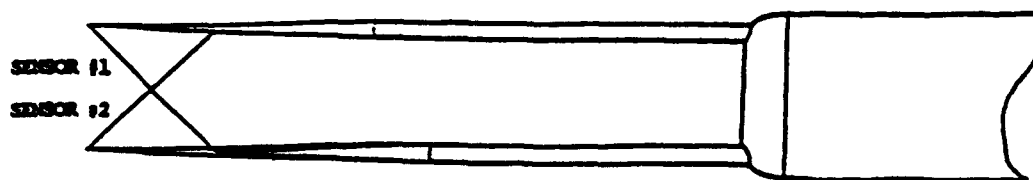
Figure 12. Hot-Film Anemometer
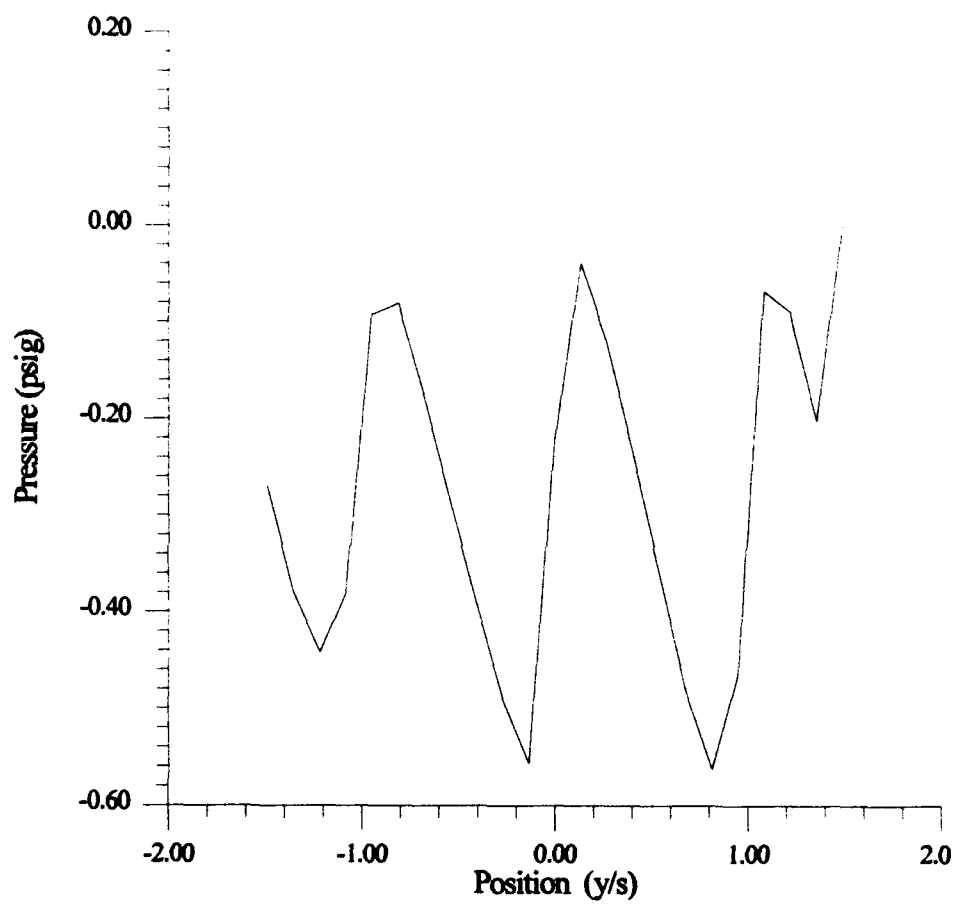
Figure 13. Inlet Periodicity, $i = 4.49°$
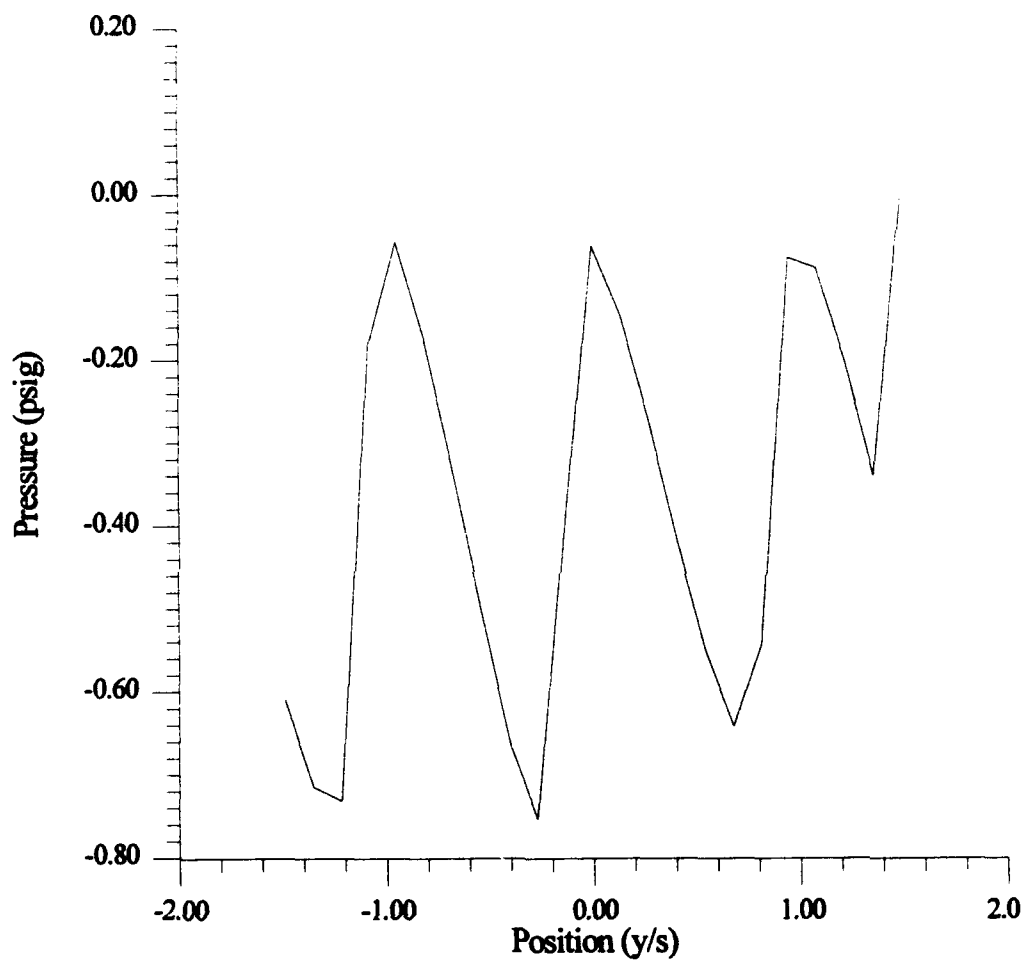
Figure 14. Inlet Periodicity, $i = 12.44°$

91
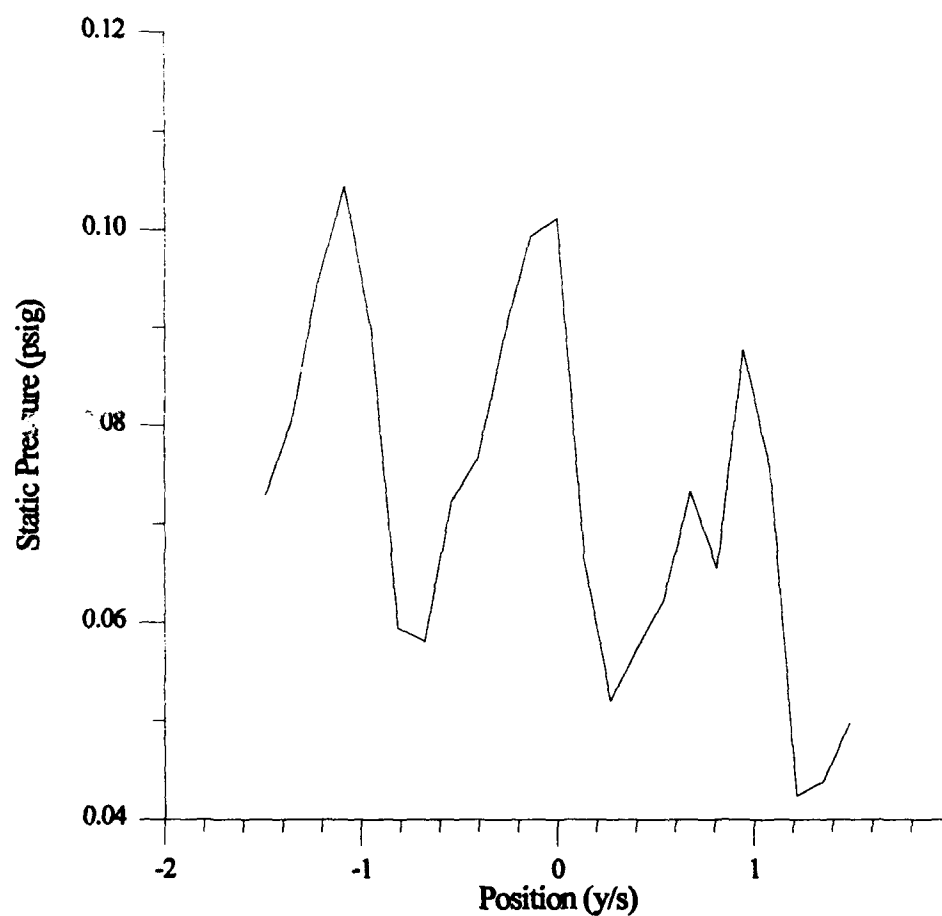
Figure 15. Skewed Exit Periodicity

92
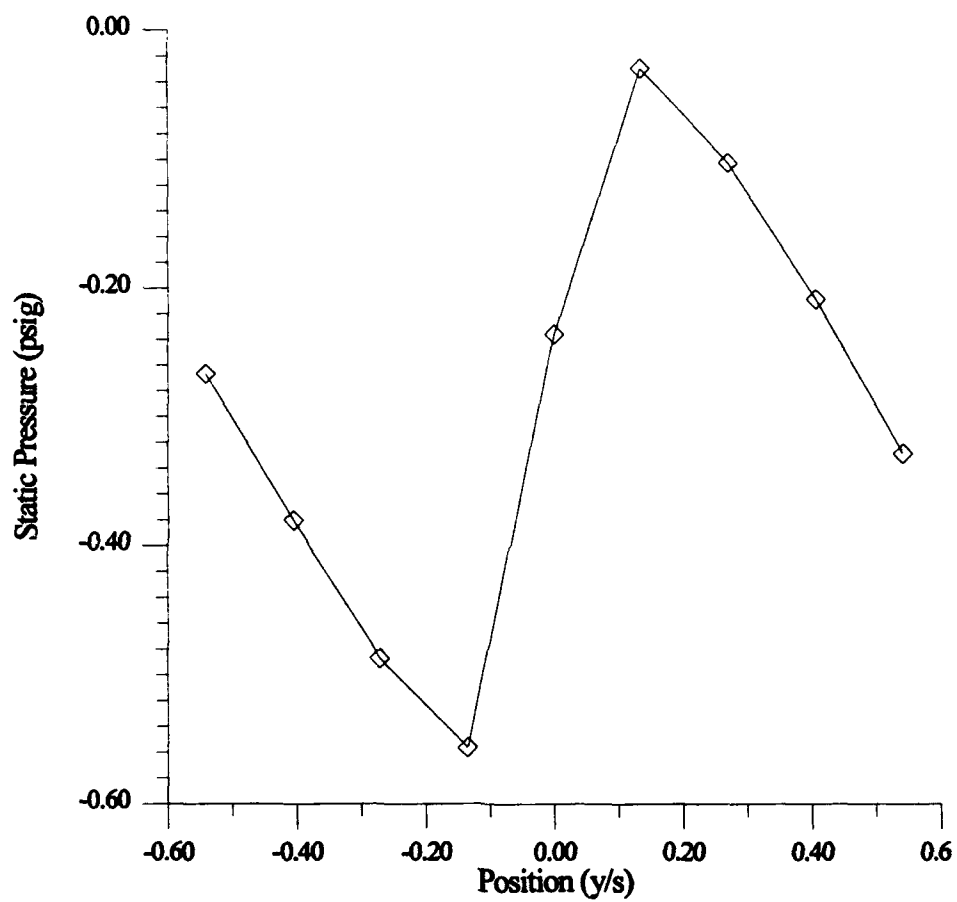
Figure 16. Inlet Period (9 ports ≈ 1 blade spacing)
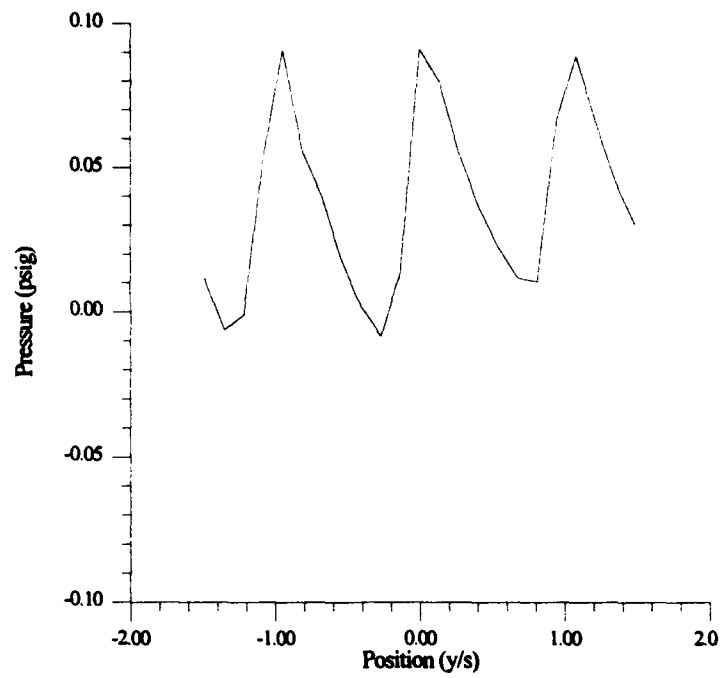
Figure 17. Exit Periodicity (23 ports)
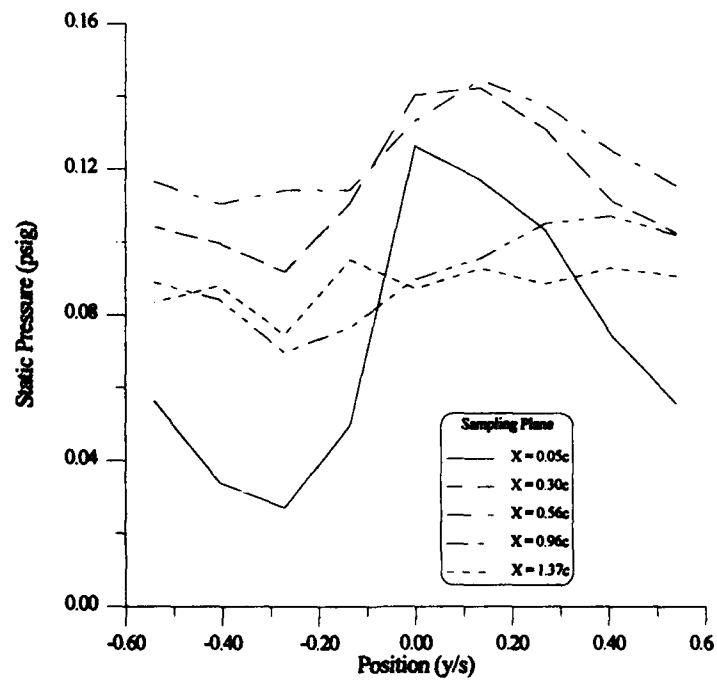
Figure 18. Sampling Plane Periodicity

94
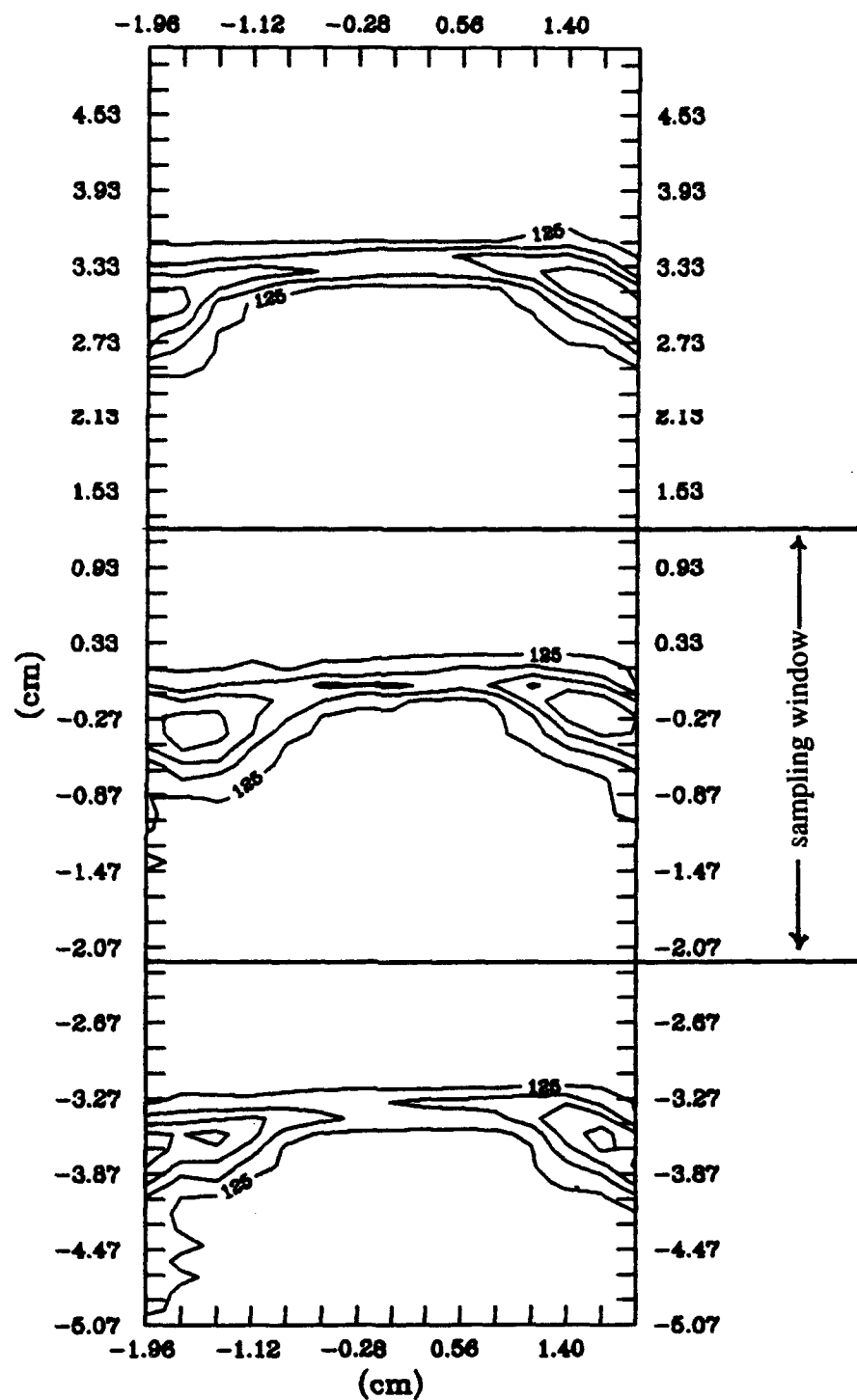
Contour Interval: 15 m/s

Figure 19. Straight Blade Velocity Profile, 3 channels, 0.30c
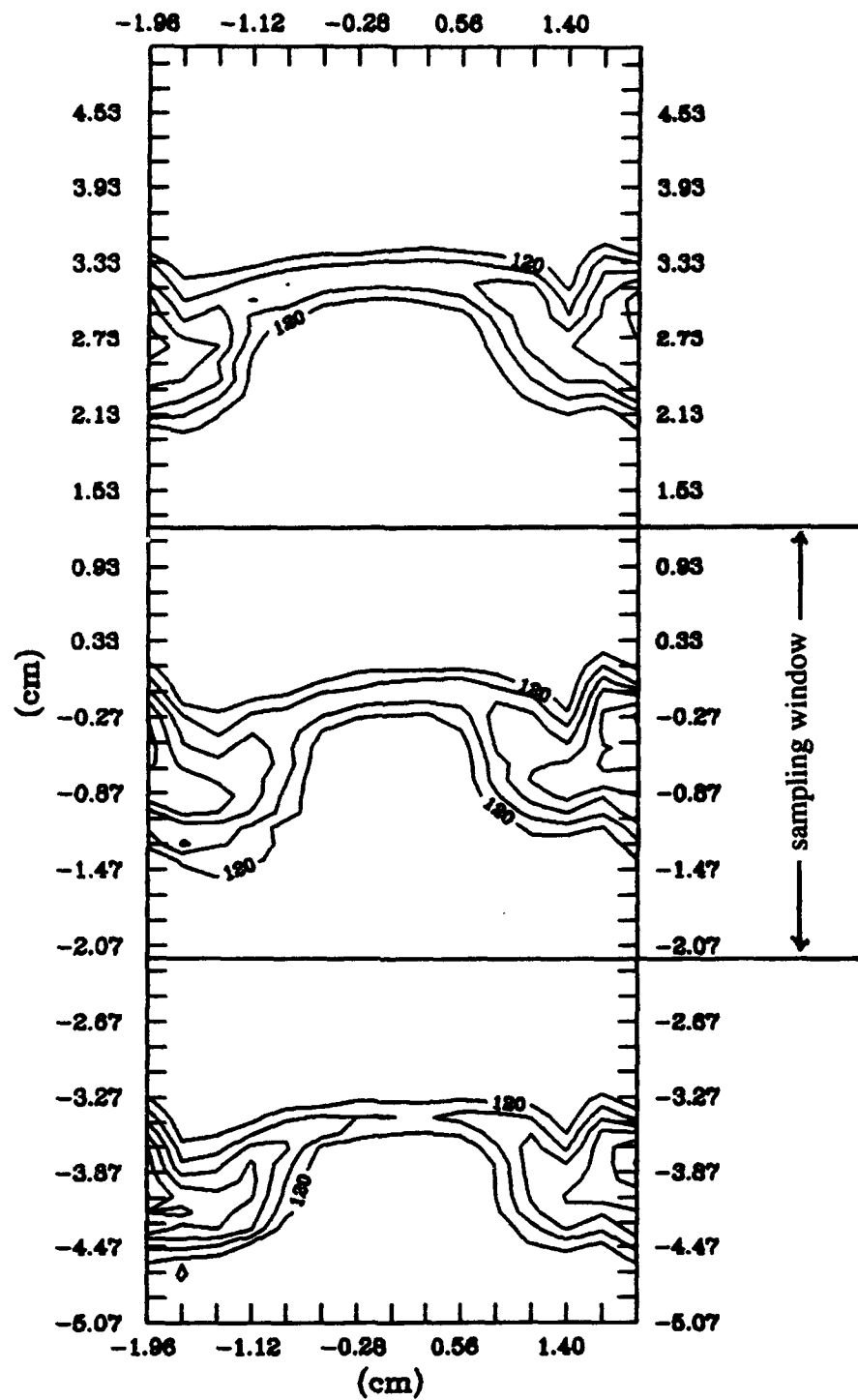
Contour Interval: 5 m/s

Figure 20. Straight Blade Velocity Profile, 3 channels, 1.37c

96
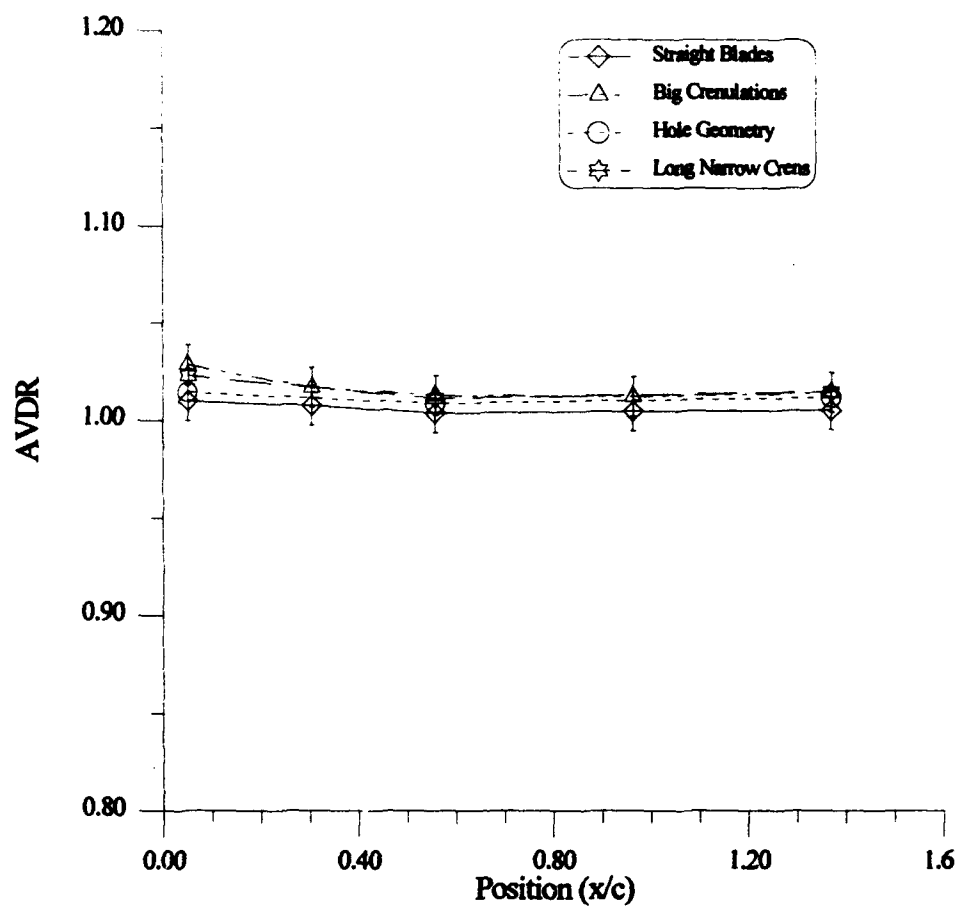
Figure 21. Axial Velocity Density Ratio

97

Contour Interval: 15 m/s   Minimum Velocity: 36 m/s
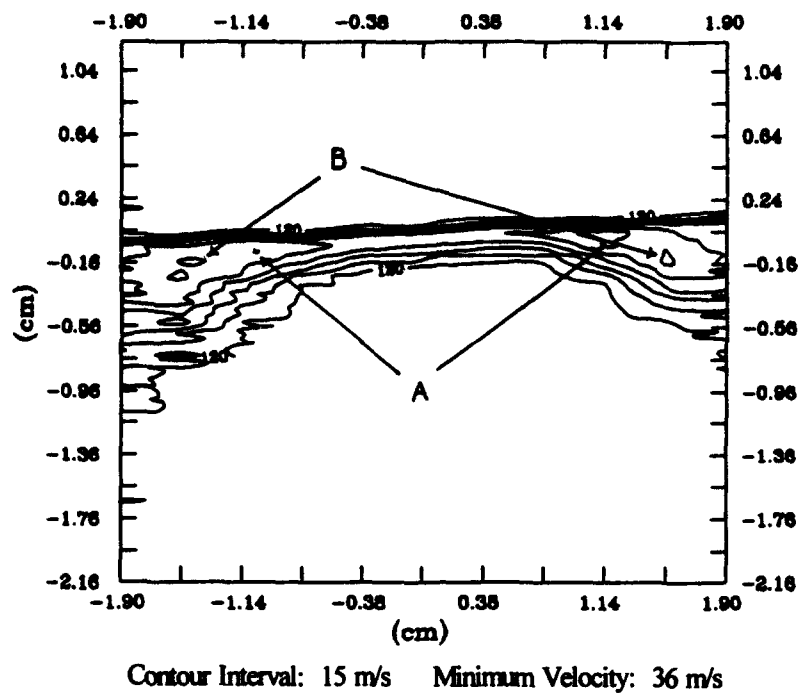
Figure 22.a. Straight Blades, Velocity Contours, 0.05c

Contour Interval: 5 m/s   Minimum Velocity: 91 m/s
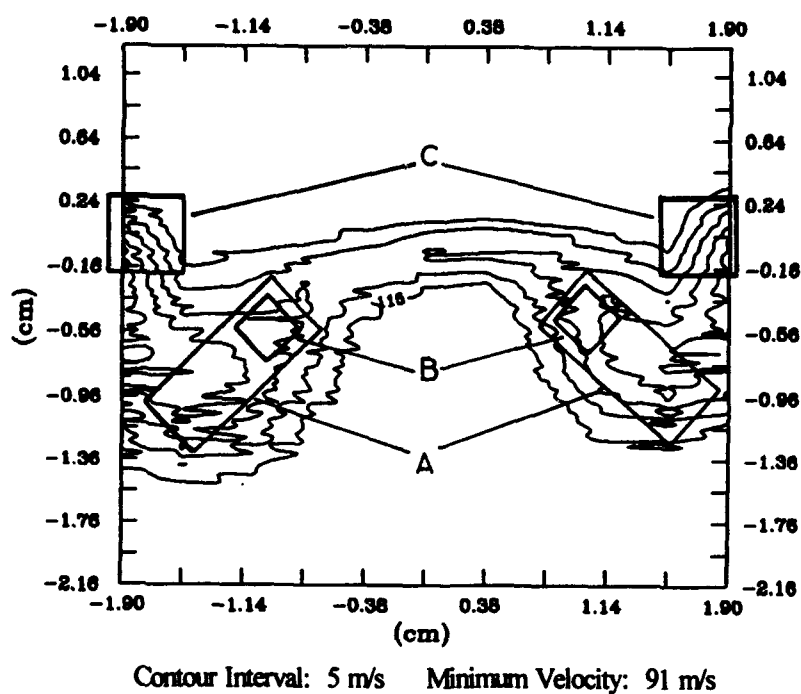
Figure 22.b. Straight Blades, Velocity Contours, 1.37c

98

Contour Interval: 15 m/s   Minimum Velocity: 53 m/s
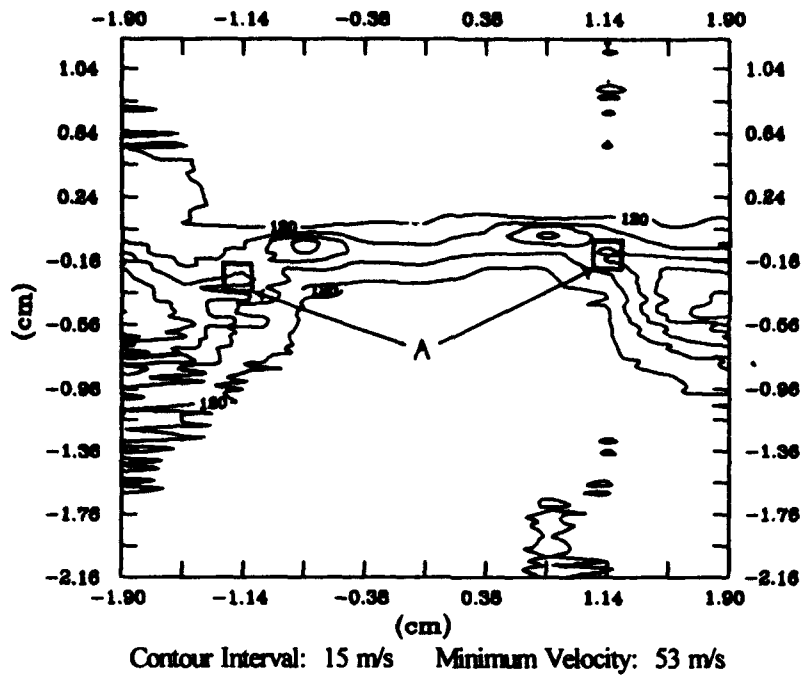
Figure 23.a. Blade 2, Velocity Contours, 0.05c

Contour Interval: 5 m/s   Minimum Velocity: 88 m/s
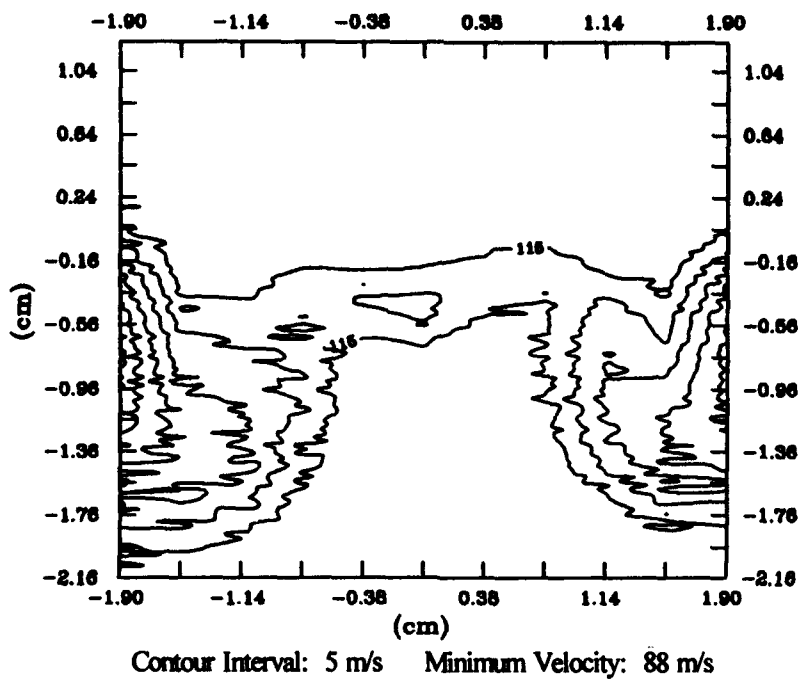
Figure 23.b. Blade 2, Velocity Contours, 1.37c

99

Contour Interval: 15 m/s   Minimum Velocity: 52 m/s
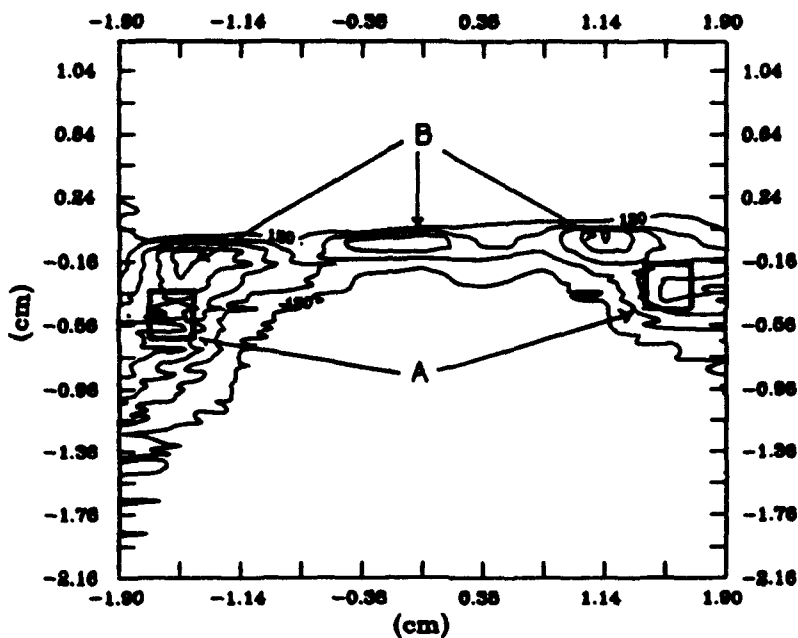
Figure 24.a. Blade 3, Velocity Contours, 0.05c

Contour Interval: 5 m/s   Minimum Velocity: 89 m/s
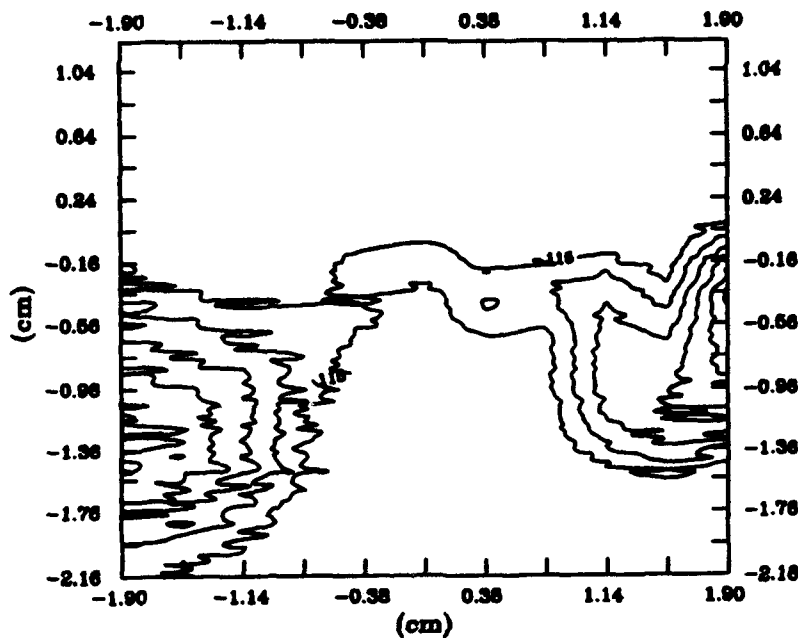
Figure 24.b. Blade 3, Velocity Contours, 1.37c

100

Contour Interval: 15 m/s   Minimum Velocity: 42 m/s
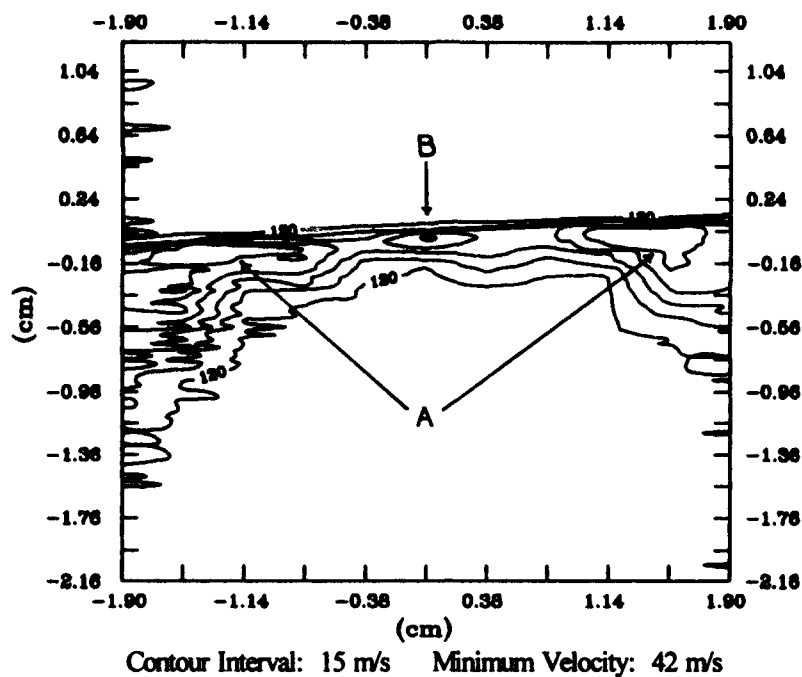
Figure 25.a. Blade 4, Velocity Contours, 0.05c

Contour Interval: 5 m/s   Minimum Velocity: 86 m/s
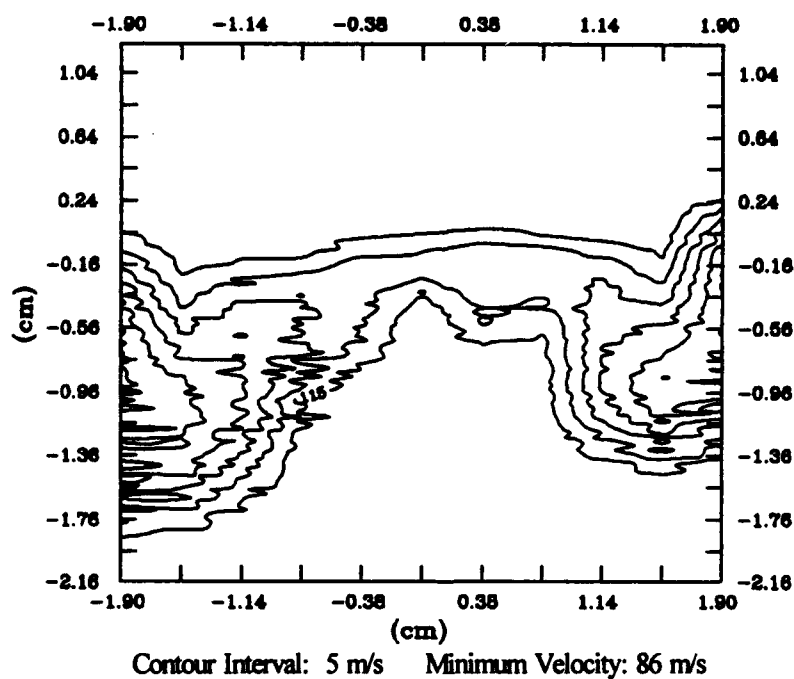
Figure 25.b. Blade 4, Velocity Contours, 1.37c

101
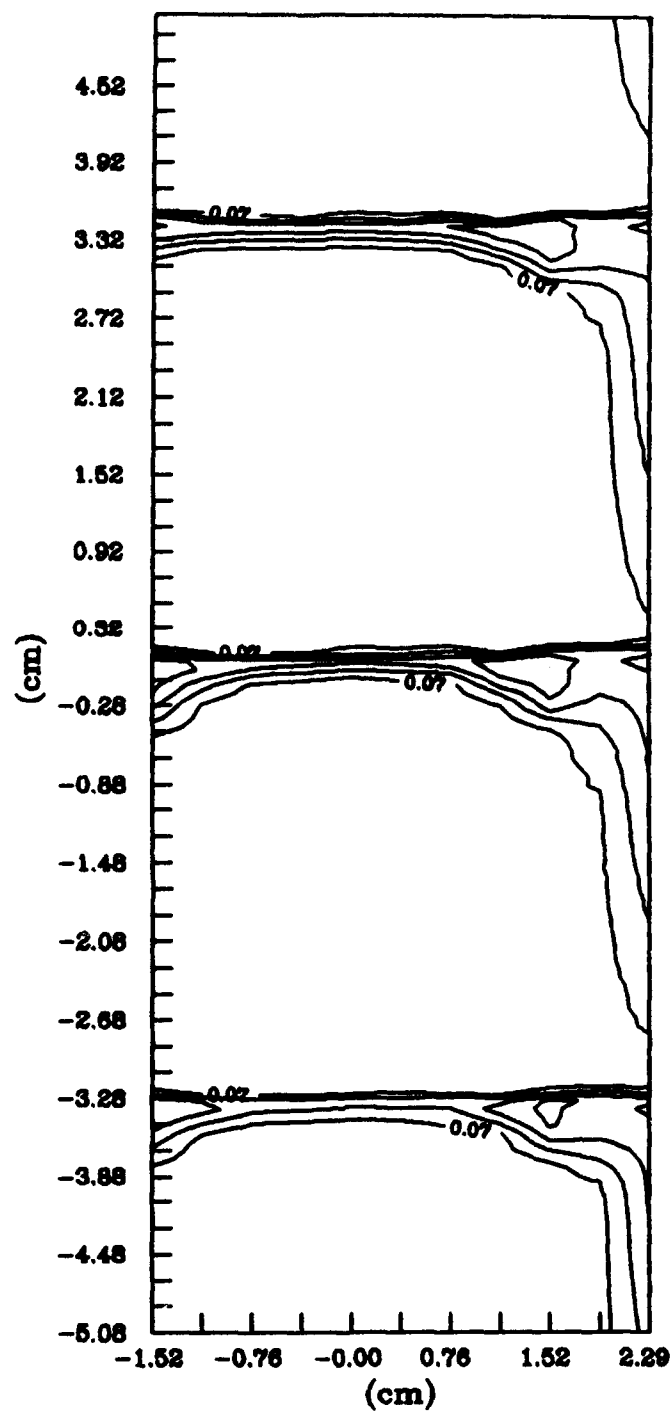
Contour Interval: 0.2

Figure 26. Corner Vortices (ω Contours, Three Straight Blades, 0.05c)

102
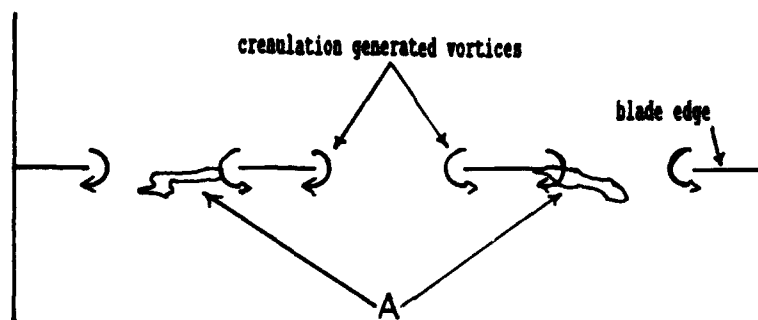
Figure 27. Blade 2 Trailing Edge Vortices
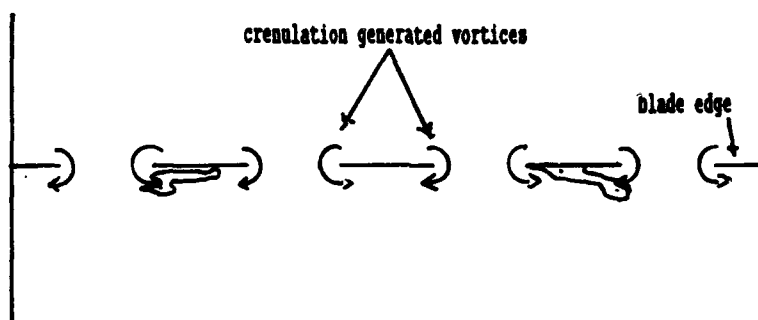
Figure 28. Blade 3 Trailing Edge Vortices

103

Contour Interval: 0.15   Max ω: 0.81
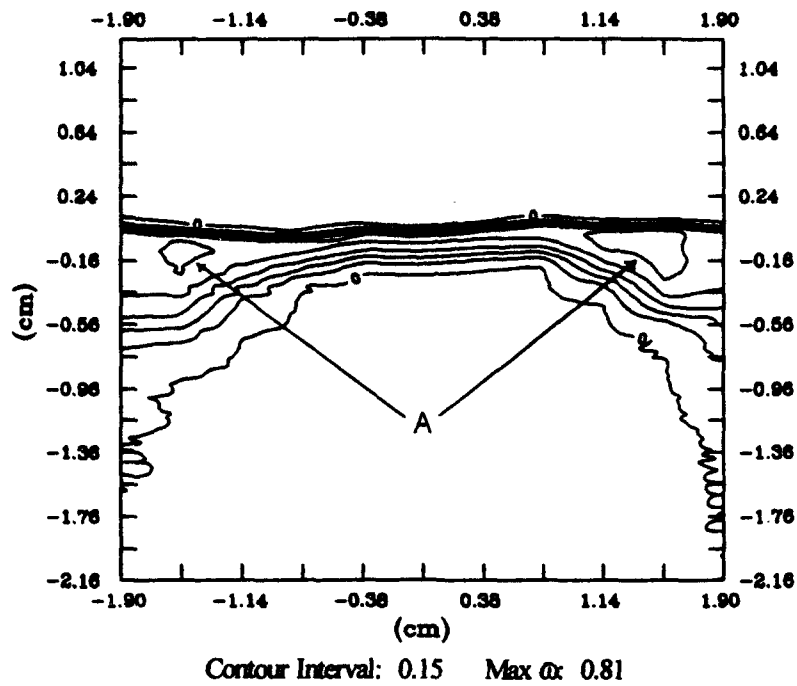
Figure 29.a. Straight Blades, ω Contours, 0.05c

Contour Interval: 0.05   Max ω: 0.38
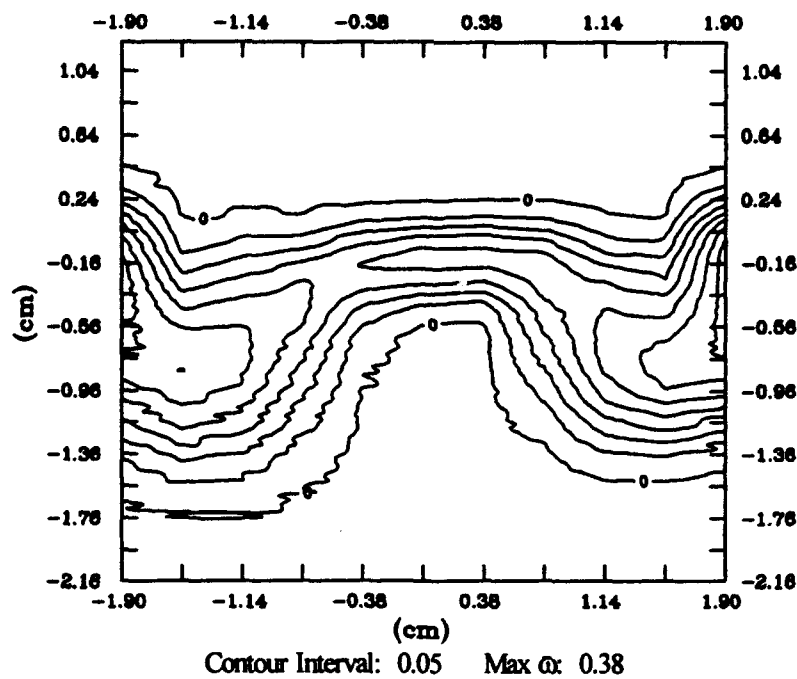
Figure 29.b. Straight Blades, ω Contours, 1.37c
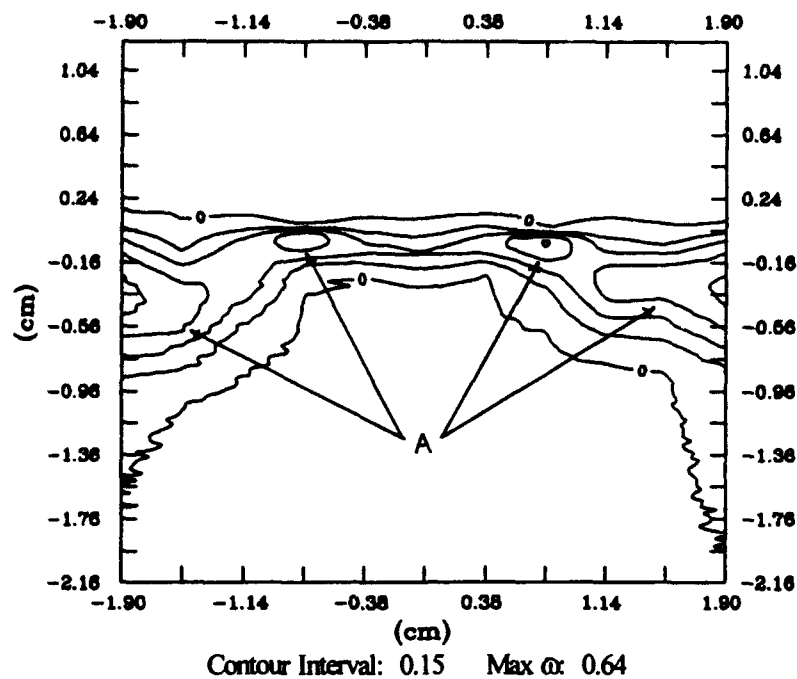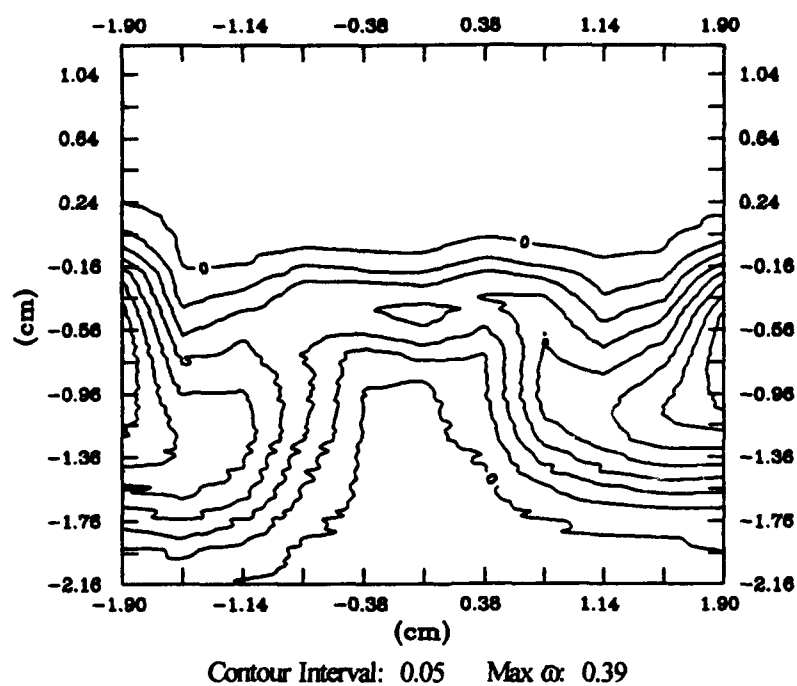
104

Contour Interval: 0.15   Max ω: 0.64

Figure 30.a. Blade 2, ω Contours, 0.05c

Contour Interval: 0.05   Max ω: 0.39

Figure 30.b. Blade 2, ω Contours, 1.37c

105

Contour Interval: 0.15   Max ω: 0.72

Figure 31.a.   Blade 3, ω Contours, 0.05c

Contour Interval: 0.05   Max ω: 0.38

Figure 31.b.   Blade 3, ω Contours, 1.37c

106

Contour Interval: 0.15   Max ω: 0.81

Figure 32.a. Blade 4, ω Contours, 0.05c

Contour Interval: 0.05   Max ω: 0.42

Figure 32.b. Blade 4, ω Contours, 1.37c

107
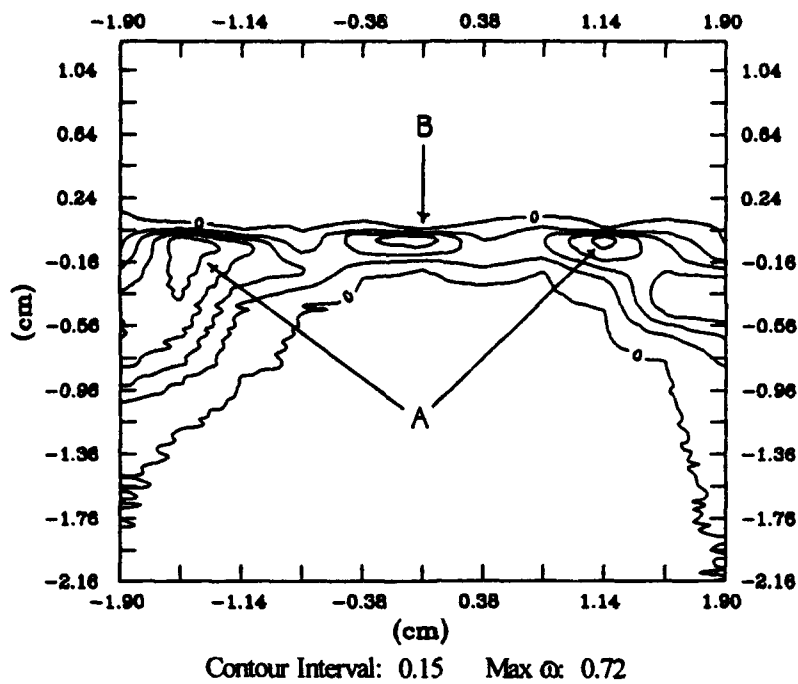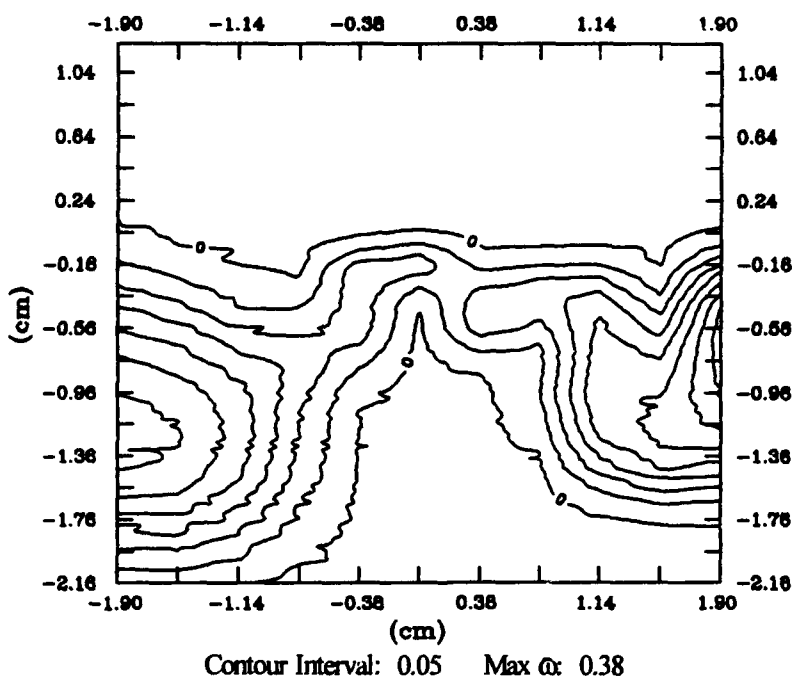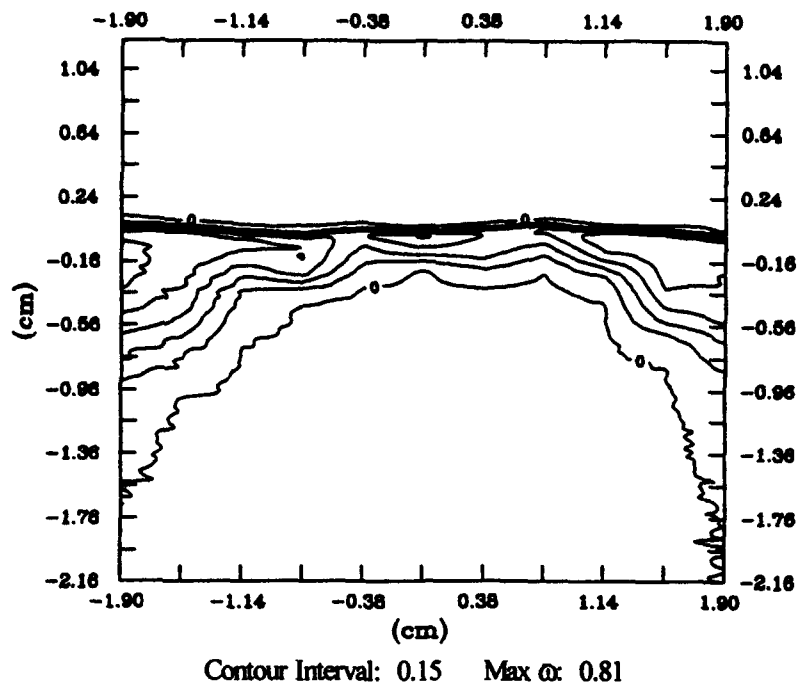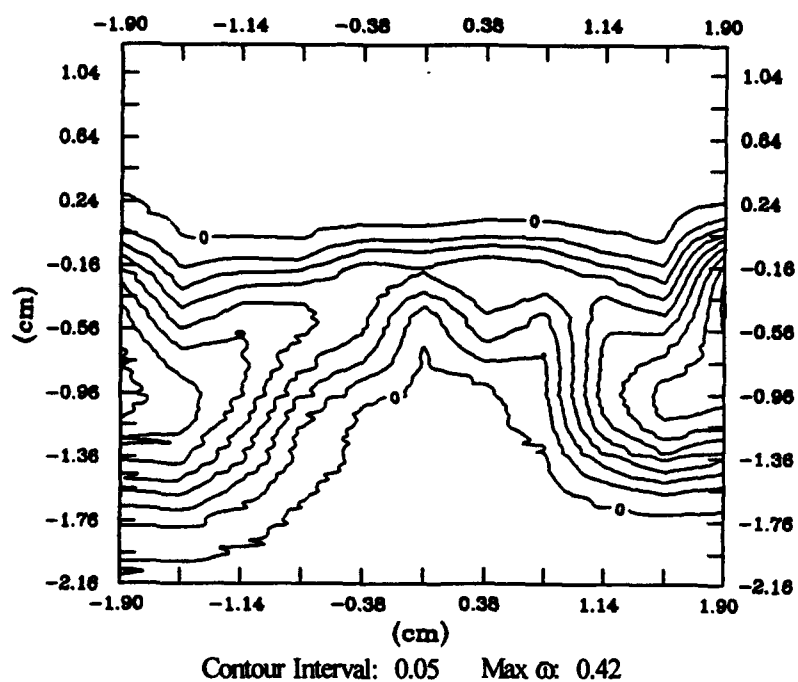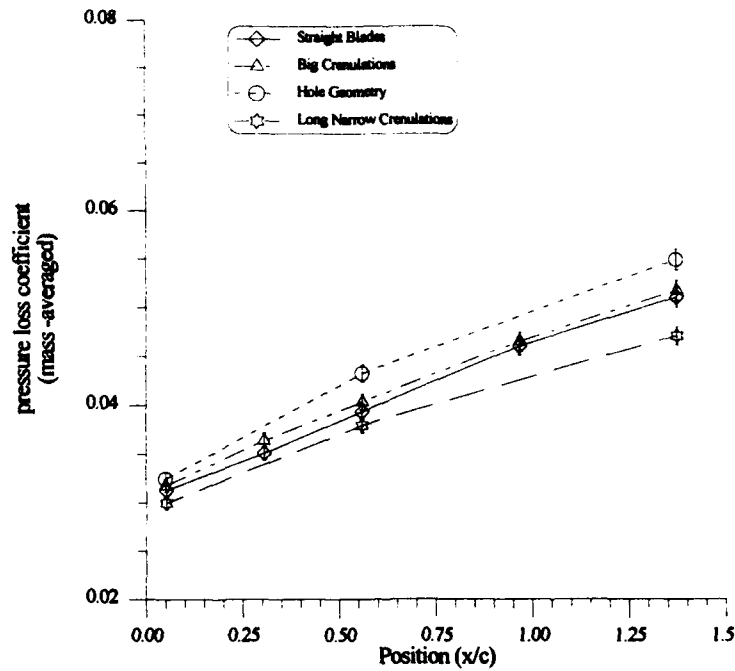
Figure 33. Pressure Loss Coefficient
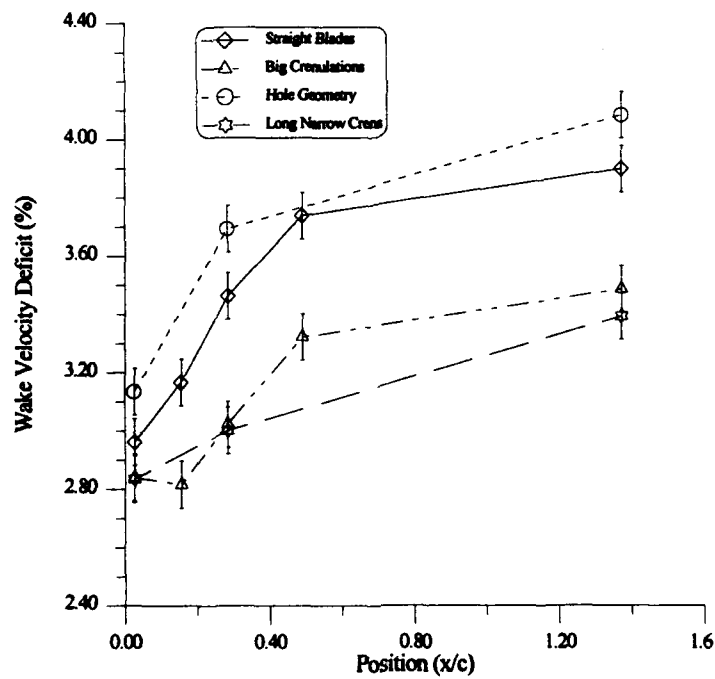
Figure 34. Wake Velocity Deficit

108
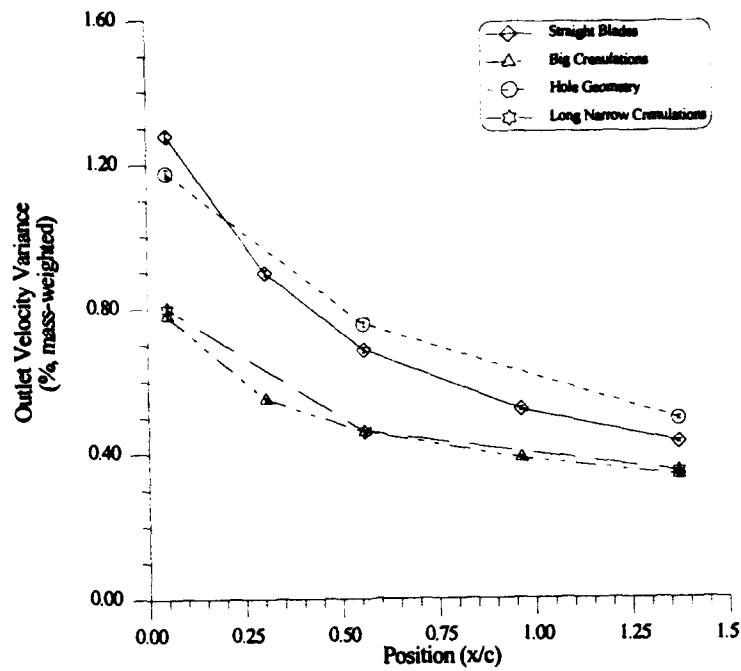
Figure 35. Outlet Velocity Variance
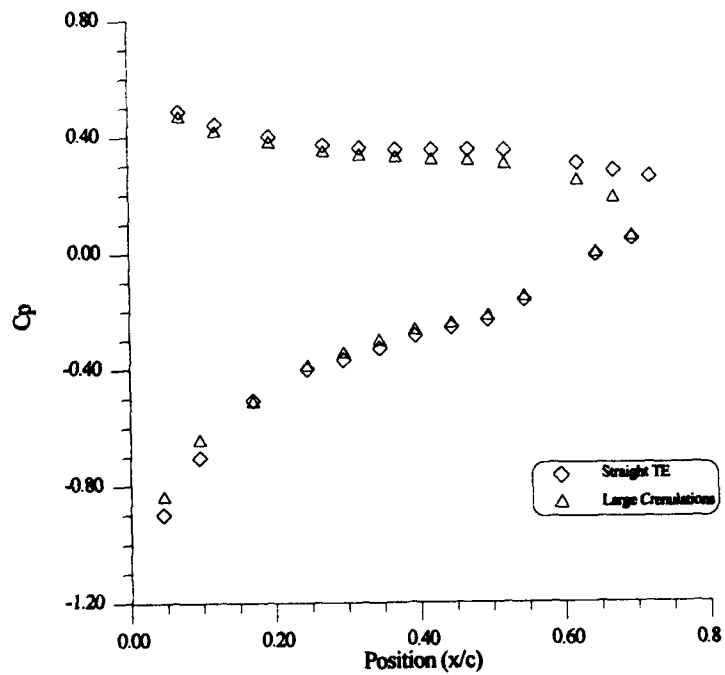
Figure 36. Blade 2 C_p Distribution

109
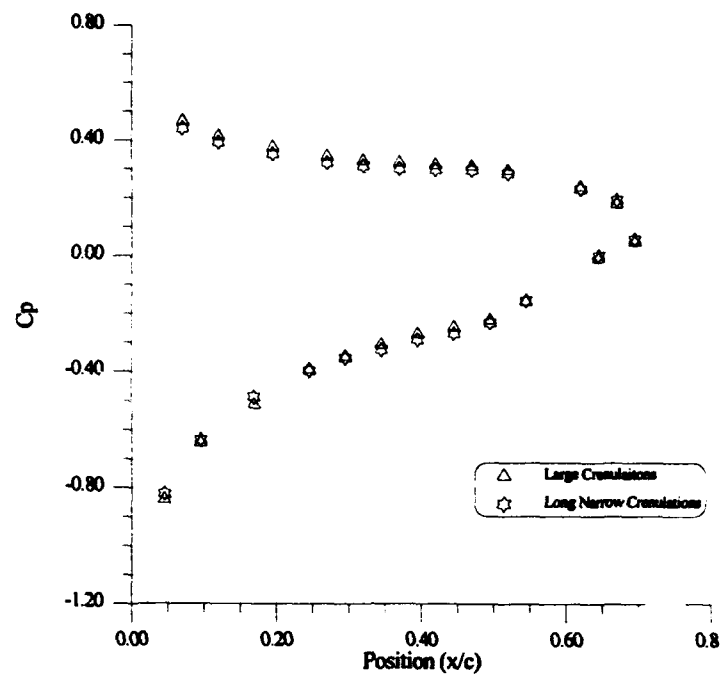
Figure 37. C_p Distribution Blades, 2 and 3
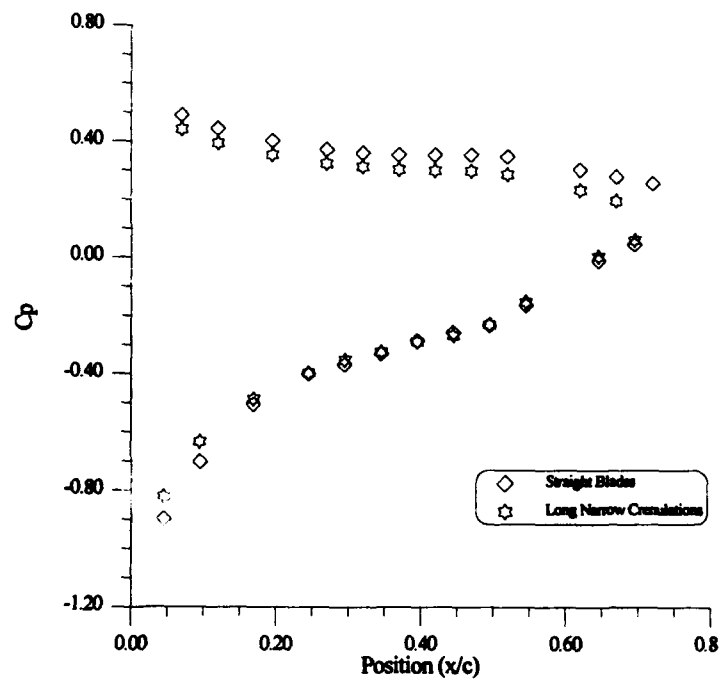
Figure 38. Blade 3 C_p Distribution

110
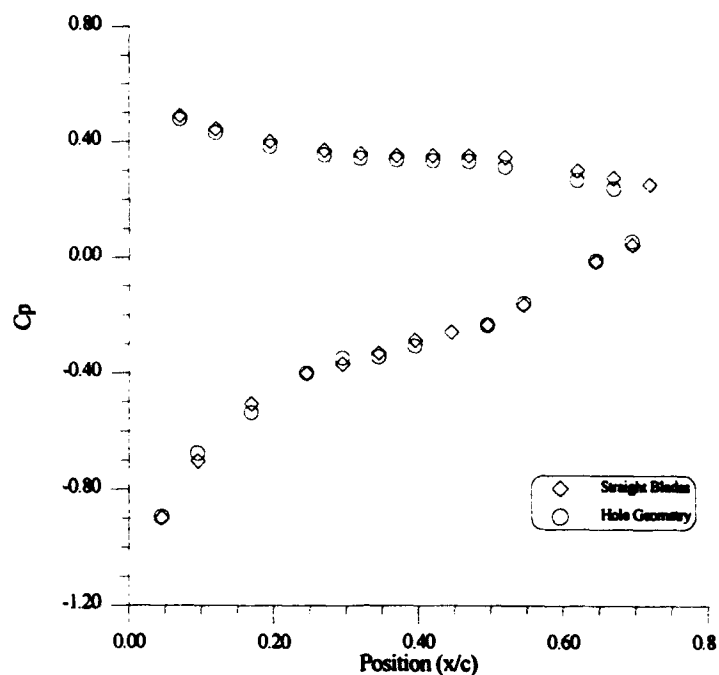
Figure 39. Blade 4 C_p Distribution
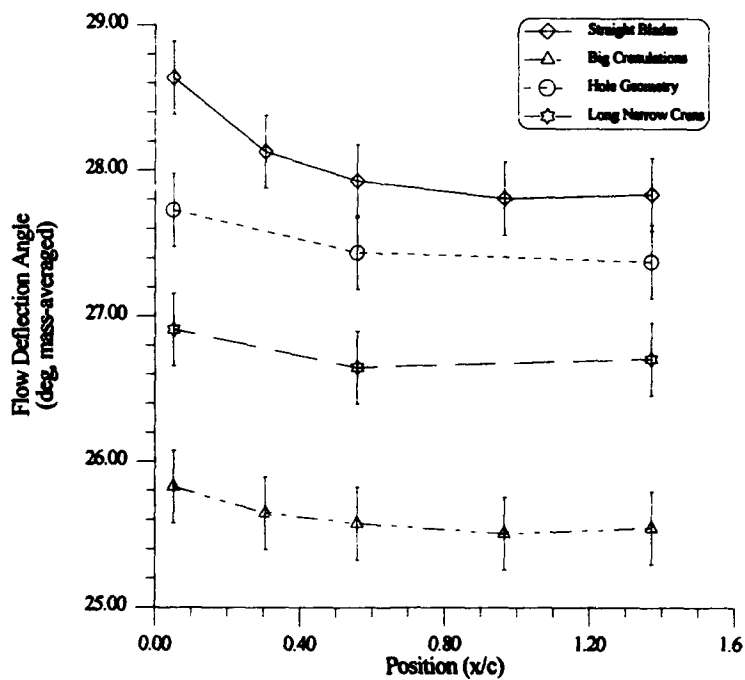
Figure 40. Flow Deflection Angle
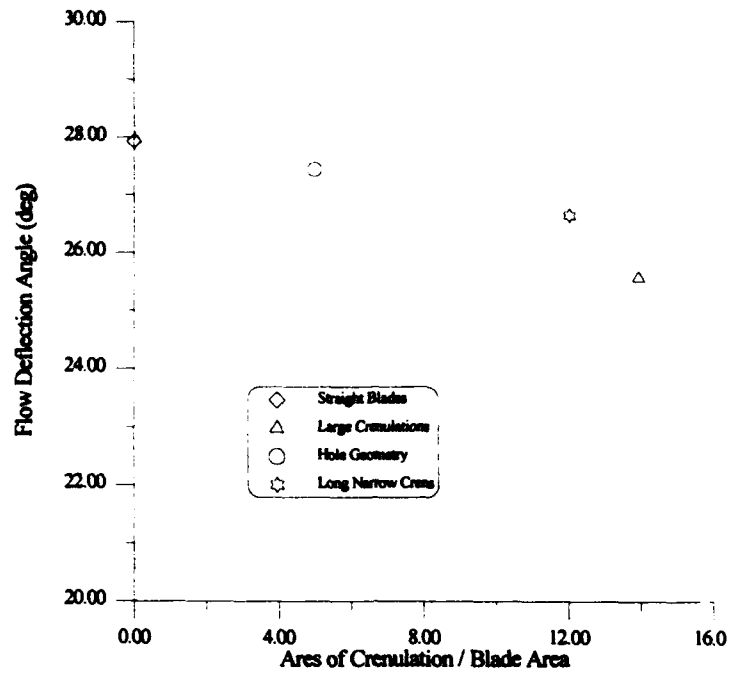
Figure 41. Blade Area vs Turning Angle
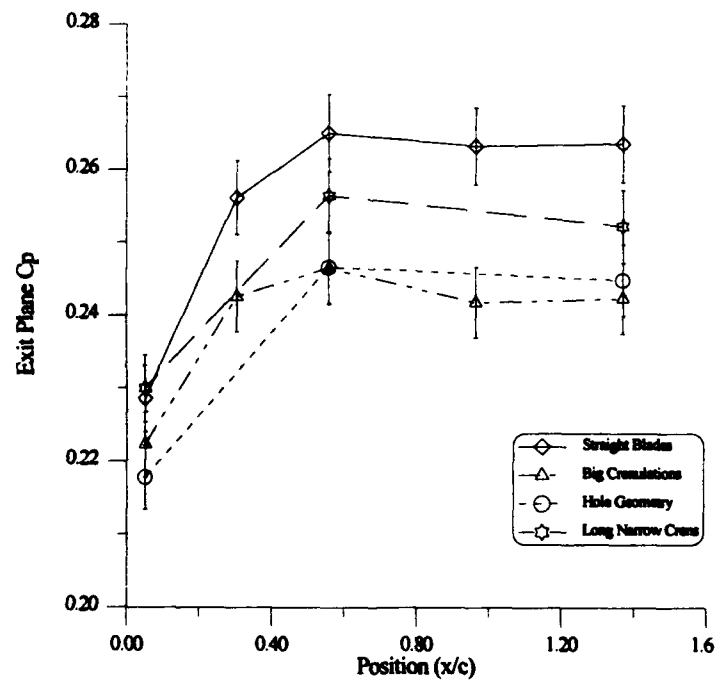
Figure 42. Exit Plane C_p

112
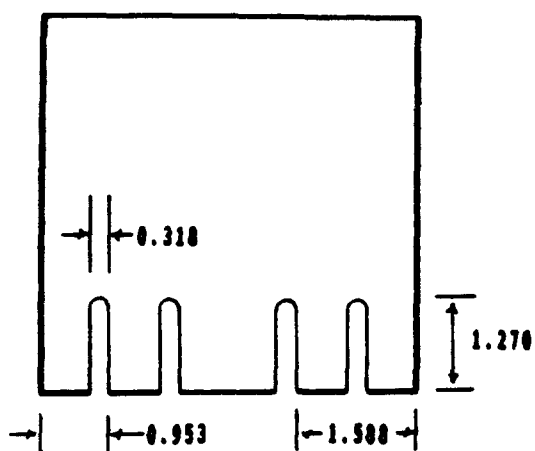
Figure 42.a.
Design 1
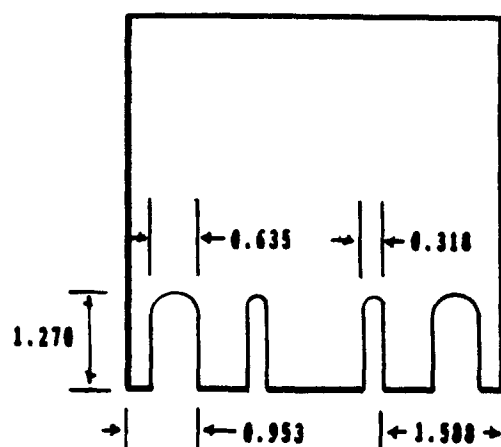
Figure 42.b.
Design 2
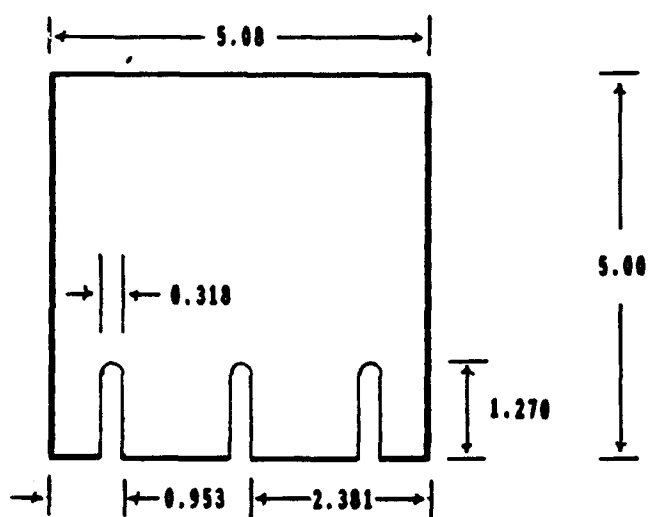
Figure 42.c.
Design 3
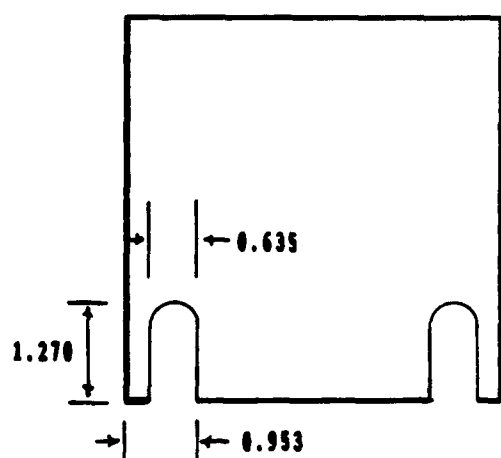
Figure 42.d.
Design 4

113

Appendix A. Blade Geometry

The compressor blades used in this investigation were NACA 64-A905 a=0.5 blades slightly modified to smooth the transition from the curved part of the upper surface to the straight tail section (Figure 9). The blades were locally manufactured out of aluminum, using a computer controlled milling machine programmed with the blade surface coordinates. The resulting blade was essentially a NACA 64-A905 a=0.5 for the first 80% of its length. The modified last 20% of the blade caused changes in the blade angles essential for cascade research.

The angles of interest to cascade investigations are the camber angle (θ) and the angles between the mean camber line and the entry and exit of the cascade (α_1', α_2') (Figure 4). These angles are normally defined by tangents to the mean camber line at the leading and trailing edges of the blade. For NACA blades with a=0.5, the mean camber line has infinite slope at the leading edge so the use of an alternate method was needed to determine the camber angle. The previously mentioned modification also needed to be accounted for since it changed the camber line at the trailing edge.

Several approaches were tried in the search for an acceptable solution to this problem. The method yielding the best results was a combination of physically measuring the slope of the training edge meanline on a computer generated plot of the airfoil, and approximating the airfoil with an equivalent circular arc. This method was a modification of the method outlined by Lieblein (1965) and entailed passing a

circular arc through the leading edge, the trailing edge and the maximum camber displaced to the mid-chord. This method was used only to determine the camber of the airfoil and not the other angles. Using it to determine α_1' led to unacceptable errors in estimating the deflection using Howell's correlation. Instead the measured α_2' was used and α_1' was determined using the relationship:

$$\alpha_1' = \theta + \alpha_2' \qquad \textbf{(27)}$$

In order to calculate the value for θ a circular arc was calculated which passed through the leading edge, the trailing edge and a point at the mid-chord displaced upward a distance equal to that of the maximum camber (Figure 44). The coordinates for these points were taken from the data file used to machine the blade. The coordinates of the three points were found to be (x,y):

Leading Edge = (0,0)

Maximum Camber = (2.50,0.335)

Trailing Edge = (5.00,0)

The equation for the circle passing through these three points was found to be:

$$(x-2.50)^2 + (y+9.17)^2 \approx 90.34 \qquad \textbf{(28)}$$

115

The equation for the tangent to a circle at a point is given by Eschbach (1975) as:

$$xx_1 + yy_1 + g(x+x_1) + f(y+y_1) + c = 0 \qquad \textbf{(29)}$$

The equation for the circle was put into the required format and Equation (29) was solved for the leading and trailing edges of the blade. The resulting angles between the respective tangents and the chord line were found to be:

$$\phi_1 = 15.254 \text{ degrees}$$
$$\phi_2 = -15.254 \text{ degrees}$$

Which resulted in a camber angle of 30.51 degrees. With this value calculated the next step was to find the angle between the mean camber line at the trailing edge and the chord line.

The angle between the mean camber line and the chord line at the trailing edge (ϕ_2) was found by measuring it on a computer generated plot of the airfoil (Figure 45). This angle was found to be 11.5 degrees. The value for α_2' was found using the equation:

$$\alpha_2' = \zeta - \phi_2 \qquad \textbf{(30)}$$

Where the symbol ζ in Equation (30) is the stagger angle.

The preceding series of computations was carried out and applied to a blade mounted in the configuration for α_1=31.00°. The pertinent blade angles were found to be:

$$\theta = 30.51°$$

$$\alpha_2' = -4.00°$$

$$\alpha_1' = 26.51°$$

$$i = 4.49°$$

The accuracy of this approximation was determined by using the angles calculated with this method in the equations for Howell's generalized performance curves as outlined by Dixon(1978). This process was used to estimate the expected deflection angle for each turning angle configuration. In order to perform this evaluation, it was first necessary to calculate the required nominal values for deflection (ε^*) and incidence (i^*). The nominal deflection is defined as 80% of stall deflection and i^* is the incidence angle required to produce this deflection. These angles are defined as:

$$\varepsilon^* = \alpha_1^* - \alpha_2^*$$
$$i^* = \alpha_1^* - \alpha_1' \tag{31}$$

117

In order to compute these values it is necessary to first find the other nominal angles. Following Dixon, these calculations were performed using:

$$\alpha_2^* - \alpha_2' = m\,\theta\,(^s/_l)^{1/2} \tag{32}$$

Where

$$m = 0.23\,(2^a/_l)^2 + \frac{\alpha_2^*}{500} \tag{33}$$

Solving Equations (32) and (33) for α_2^* yield:

$$\alpha_2^* = \frac{0.23*\theta\,(^s/_l)^{1/2}\,(2*^a/_l)^2 + \alpha_2'}{[1 - (\theta\,(^s/_l)^{1/2})/(500)]} \tag{34}$$

Next it is necessary to find α_1^* using:

$$\alpha_1^* = \tan^{-1}\left[\frac{1.55}{1 + 1.5*^s/_l} + \tan\alpha_2^*\right] \tag{35}$$

which approximates Howell's low speed correlation and is applicable for angles of α_1^* between zero and forty degrees (Dixon, 1978).

The preceding equations yielded the following nominal values:

$$\alpha_2^* = 1.86°$$
$$\alpha_1^* = 38.75°$$
$$\epsilon^* = 36.89°$$
$$i^* = 12.24°$$

With the values of i^* and ε^* it is possible to calculate the quantity:

$$\frac{i - i^*}{\varepsilon^*}$$

which is used along with Figure 3.17 in Dixon (p. 78) to yield the quantity:

$$\frac{\varepsilon}{\varepsilon^*}$$

relating the actual deflection angle to the nominal deflection angle. The calculations were carried out and the estimated deflection angles for the four cascade turning angles were computed. These were found to correlate fairly well to the measured deflection angles produced by the straight trailing edge blades. The results are summarized in Table 6 below.

Table 6. Measured and Predicted Flow Deflection Angles

Air Flow Angle (α_1)	Incidence Angle (i)	Measured Deflection (ε)	Modified Circular Arc (ε)
38.95	12.44	35.49	37.40
35.83	9.32	31.92	34.62
31.00	4.49	27.86	30.31
25.43	-1.08	23.52	24.81

It should be noted that Howell's correlation used here was for two dimensional flow while the cascade used in this investigation had strong three dimensional effects (Chap II). Considering this, discrepancies ranging from 1.7 to 2.5 degrees represented a reasonably good correlation between the predicted and measured values.
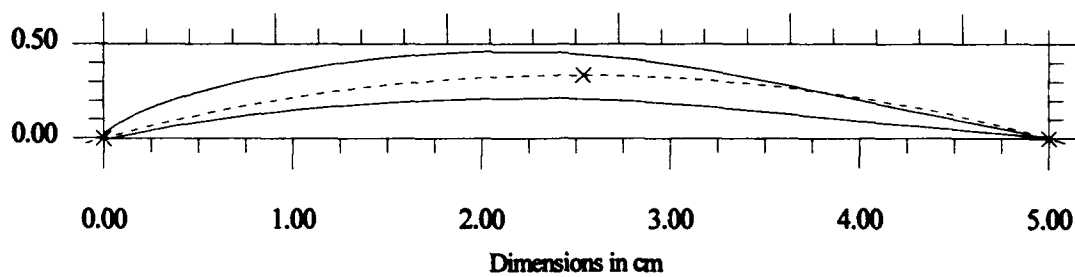
Figure 44. Blade Profile with Circular Arc

chord line

ϕ_2
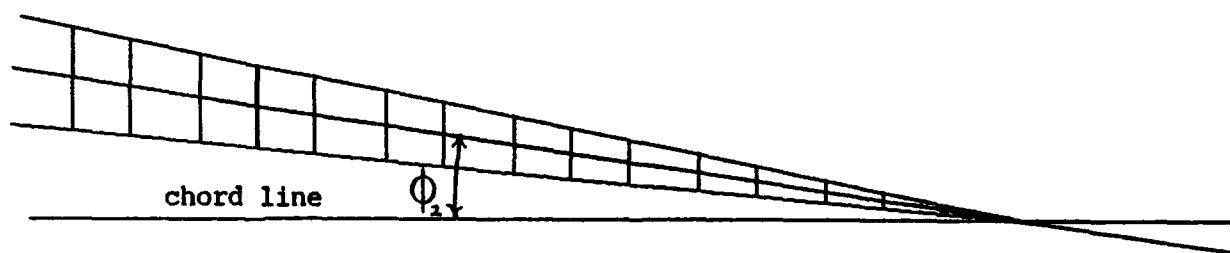
Figure 45. Tail Section of Blade Profile

121

Appendix B.   Equipment Listing

<u>Subsystem</u>   <u>Model Number/Description</u>

Pressure Measurement   Pressure Systems Inc. Model 8400 Pressure
                                                    Scanner (20 kHz maximum sample rate)
                                                       Model 8415 Scanner Interface Unit
                                                       Model 8420 Scanner Digitizer Unit
                                                       Model 8440 Analog Input Unit
                                                       Model 8433 Pressure Calibration Unit
                                                                    (1 psid)
                                                       Model 8433 Pressure Calibration Unit
                                                                    (5 psid)
                                                       Certified Standard Transducer
                                                          (0.2-18 psi range, _0.00001 psi accuracy)

                                                    Transducer block P/N 32RG-0301
                                                          (1 psid range, 0.0005 psi accuracy)

                                                    Transducer block P/N 3201B
                                                          (1 psid range, 0.0005 psi accuracy)

                                                    Transducer block P/N 3205B
                                                          (5 psid range, 0.0005 psi accuracy)

                                                    Pressure Rake (11 ports, spaced 0.381 cm)
                                                          (0.0635 cm ID, 0.0889 cm OD)

                                                    CEC Model 2500 Digital Barometer
                                                          (13.00 psia - 15.51 psia range, 0.005 psi accuracy)

Velocity and Temperature
Measurement   TSI Model IFA 100 System Intelligent Flow
                                                    Analyzer
                                                                Model 140 Temperature Module
                                                                Model 150 Anemometer Modules (2)
                                                                Model 157 Signal Conditioner Module (3)

Subsystem	Model Number/Description
Velocity and Temperature Measurement	TSI Model IFA 200 System Multichannel Digitizer Model 252 Digitizers (3) (50 kHz maximum sample rate, 5 V range, 0.002 V accuracy)
	TSI Model 1241-10 X-Film Sensor
	TSI Model 1241-20 X-Film Sensor
	TSI Model 1155-36 probe support (modified length to 24")
	TSI Model 1125 Probe Calibrator
	Omega T-type Thermocouple (copper-constantan, _0.3°C accuracy)
Temperature Measurement	Hewlett-Packard Model 3455A Digital Voltmeter (0.00002 V accuracy, 24 Hz maximum sample rate)
	Hewlett-Packard Model 3495A Scanner
	Omega T-type Thermocouples (2) (copper-constantan, _0.3°C accuracy)
Traverse Control	New England Affiliated Technologies Model 310 Programmable Motion Controllers (2)
	Oriental Motor Company Stepper Motors (2) (400 steps/revolution resolution)
Central Computer	Zenith Model Z-248 (80286 processor with math co-processor) National Instruments Model GPIB-PCII General Purpose Interface Board) TSI Model 6260 Parallel Interface Board
	Software (developed by AFIT/ENY, written in MS-QuickBasic 4.5)

Appendix C: Effects of Ambient Pressure on Cascade Data

Introduction

This appendix discusses the effects of changes in ambient pressure on the pressures measured in the cascade. It was discovered that the pressures measured at the various locations in the cascade varied directly with ambient pressure. This variation validates the choice of ambient pressure as a reference.

Discussion

The data used in this analysis were taken over a period of approximately eight hours. The tailboard setting, incidence angle, crenulation geometry, probe and sampling plane were the same for all of the data runs. The results of these test runs are depicted graphically in Figure 46. This figure depicts the changes in the tank, inlet, exit and ambient pressures over the course of the six runs. It can be seen that as the ambient pressure first increased and then decreased, the other pressures followed it. Figure 47 shows the same data in terms of psig with ambient as the reference pressure.

The difference between the minimum and maximum ambient pressures was 0.109 PSI. The changes in the other pressures when evaluated in terms of psig were smaller by an order of magnitude. The variation in P_{int} was the largest with a variation of 0.024 psig. The inlet pressure varied by 0.012 psig and the exit pressure

124

by only 0.003 psig. These small fluctuations in the measured pressures are an

indication that changes in ambient pressure will be reflected in all measured pressures.

and justifies the use of ambient pressure as the reference.
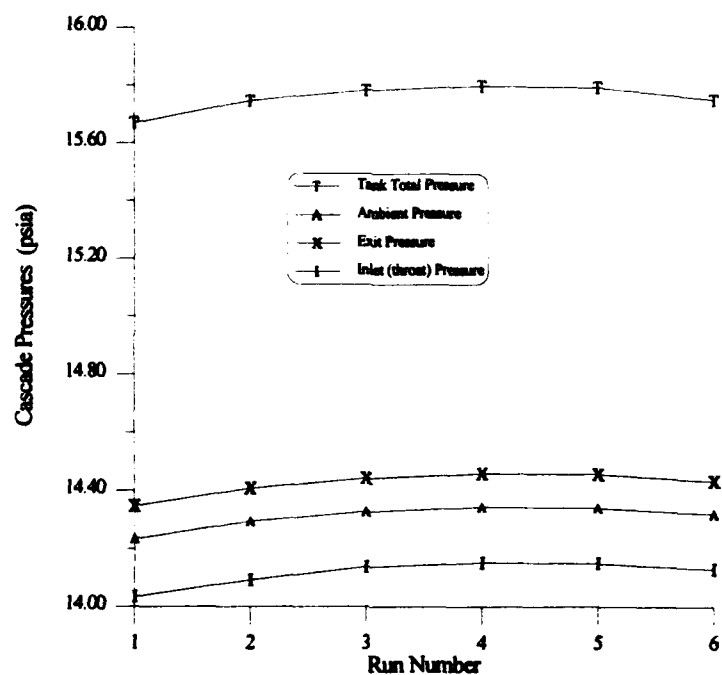
Figure 46. Ambient Pressure Effects (psia)
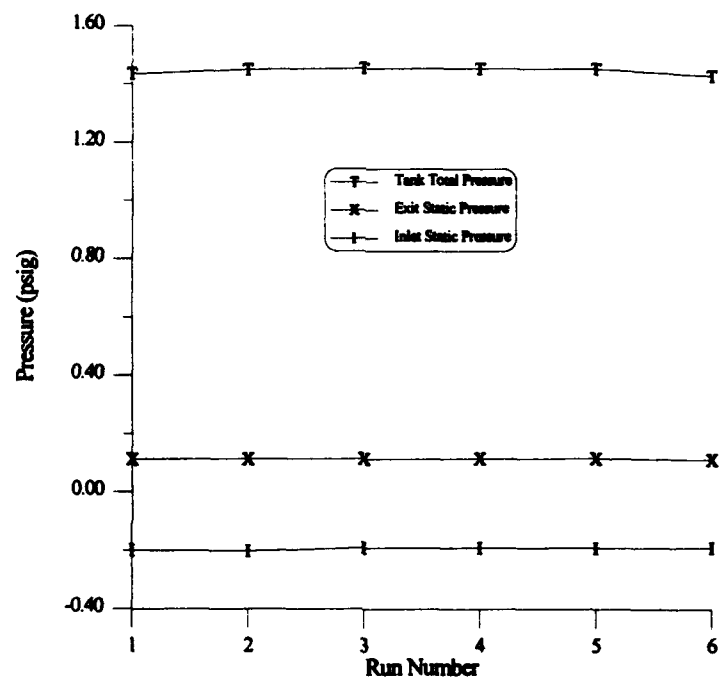
Figure 47. Ambient Pressure Effects (psig)

126

Appendix D: Error Analysis

Equipment Accuracies

The equipment accuracies specified by the manufacturer or determined during calibration procedures are summarized in Table 7. These values are used in the following analysis to estimate the expected error for each of the calculated parameters. The method for determining the errors is demonstrated by example for the pressure loss coefficient. The errors for the other quantities are calculated in a similar manner.

Pressure Loss Coefficient. The error for ω was estimated by evaluating equation (4) for a given set of data taken from an actual test run. The equation was then re-evaluated for the same data changed by the accuracy of the instrumentation used to measure each quantity. The instrument accuracies were either added to the measured reading or subtracted from it so as to create the largest error in the final answer. Once these calculations were made, the percent change in the final answer was calculated using:

$$ERROR = \frac{\overline{\omega} + \varepsilon}{\overline{\omega}} - 1$$

where ε represents the effect of changing all of the measured values individually. If this error is assumed to occur in the same direction at every point of the summation, the largest error will be found. This is a valid assumption since the quantity in the numerator of Equation (4) is a difference in pressures and doesn't vary much in

relation to the size of the error associated with the pressure transducers. The quantities in the denominator, on the other hand, are all throat conditions and don't vary much over the period of the data run. These calculations resulted in an estimated error due to equipment capabilities of 2 percent for ω. The errors that might be introduced by the mass averaging process were found to be largely offsetting and assumed to be negligible.

C_p Analysis. An analysis of the equations for C_p revealed that the error would be the same as for ω. This is because the quantities in the numerator of Equation (3) are again a difference in pressures and are of the same order of magnitude as for ω. The quantities in the denominator, on the other hand, are exactly the same as those for ω. This applies to both the blade C_p distribution and the non-dimensional static pressure rise.

Wake Velocity Deficit. The wake velocity deficit presents a different situation. In this case it was necessary to determine appropriate error for the two velocities in Equation (8). The problem was that these are both either arithmetic or mass averaged values. This problem was made more complex by the fact that the velocities used to compute the freestream velocity were also used to compute the downstream axial velocity. These two facts make it impossible for the numerator to be in error in one direction (i.e. high) by the same amount the denominator is displaced in the opposite. Additional insight was gained when the nature of the error introduced by the hotfilm was examined. The majority of the samples taken were at a negative angle and the

128

errors found in the calibration process were all in the same direction for negative angles. From these two facts, it was determined that the errors should be in the same direction for both the numerator and denominator. The expected error was determined by adding 0.5 m/s to representative values for both of these. The representative values were taken from actual data runs and were 113 m/s for downstream axial velocity and 120 m/s for the freestream velocity. These values resulted in an estimated error of 3 percent for values representative of those measured in the cascade.

Outlet Velocity Variance. The velocity variance is similar but more complicated. If the mass averaging process is ignored, the quantity to be analyzed is:

$$\sum_{j=1}^{n} \left(\frac{V_{2_j}}{\overline{V}_2} - 1 \right)^2$$

In this case it is possible to have a local exit velocity with a -0.5 m/s error while the arithmetic average of all of the exit velocities has a total error near +0.5 m/s. Since most of the local values must be near +0.5 m/s for the average error to be +0.5 m/s, the errors are much more likely to be in the same direction by nearly the same amount once the summation process is completed. For error estimation purposes, an error value of 0.5 m/s was added to the representative values of the numerator and denominator. The values used for this evaluation were an average velocity of 116 m/s and an individual value of 99 m/s which was one standard deviation below the average value. This method resulted in an estimated error of 1 percent for the velocity

129

variance.

Axial Velocity Density Ratio. The approach to estimating the error in the *AVDR* was essentially the same as that followed for the other parameters, with Equation (2) being evaluated term by term. In this case the velocity in the denominator was calculated from upstream quantities. These quantities should have identical errors for each data point since the same instrument was used, in virtually the same conditions, to measure the quantities. This evaluation applies equally well to the densities. The errors for these values were calculated in the same way as those for the ω discussed above. The velocity in the numerator was evaluated in a manner similar to the velocity variance and velocity deficit discussed above. In this case, since there is less vorticity at the center span for all configurations, virtually all of the velocities were taken at similar flow angles. When representative value were used for each quantity and then perturbed by the appropriate error, the resulting overall error was calculated to be 1 percent.

Table 7. Component Accuracies

Component	Accuracy
Pressure Transducers	0.0005 psid
Digital Barometer	0.005 psia
Thermocouples	0.3°C (meas)
Hotfilm Velocity	0.5 m/s (meas)
Hotfilm Angles	0.25° (meas)

Appendix E: Corner Crenulation Geometry

Introduction

The reasoning behind the choice of this geometry is given in Chapter III. Unfortunately the placement of the large crenulations at the edges of the blade did not produce the desired results. As described below, this geometry suffered from large total pressure losses and was therefore not extensively tested. The data presented in this appendix, for the corner crenulations, were the result of one acquisition run at each location with each probe. There were no attempts to verify the results and they were used only to discern general trends.

Results

An evaluation of the velocity contour plots of the blade wakes show the corner crenulations to have a distribution similar to that of the straight blades (Figures 22, 48). There are minor vortices in the middle of the blade, but these are evidently too weak to either disrupt or reduce the passage or concentrated shed vortex. While the velocity gradients aren't as steep as those of the straight blades, and the minimum velocities aren't as low, the WVD is virtually the same and the velocity variance is better only near the blade (Figures 49, 50). This lack of improvement in wake

mixing makes the use of these crenulations questionable. The performance parameter that led to the final elimination of this geometry from consideration was the pressure loss coefficient.

The pressure loss coefficient for all of the blades tested is plotted against downstream location in Figure 51. The pressure loss contour plotted in this figure was determined differently than the ω used to evaluate the other geometries. In this case the additional data runs required merge the velocities from the hotfilm runs with the data from the pressure rake were not made. The ω plotted in Figure 51 is based entirely on the pressure rake data. This reduction method incorporates the artificially low velocities derived from the pressure data in the mass averaging scheme. For comparison purposes, the data for the other geometries was reduced in the same way. An examination of Figure 51 shows that the corner crenulation geometry has larger total pressure losses at all locations. These large total pressure losses are the reason further tests were not made.

Contour Interval: 15 m/s   Minimum Velocity: 49 m/s
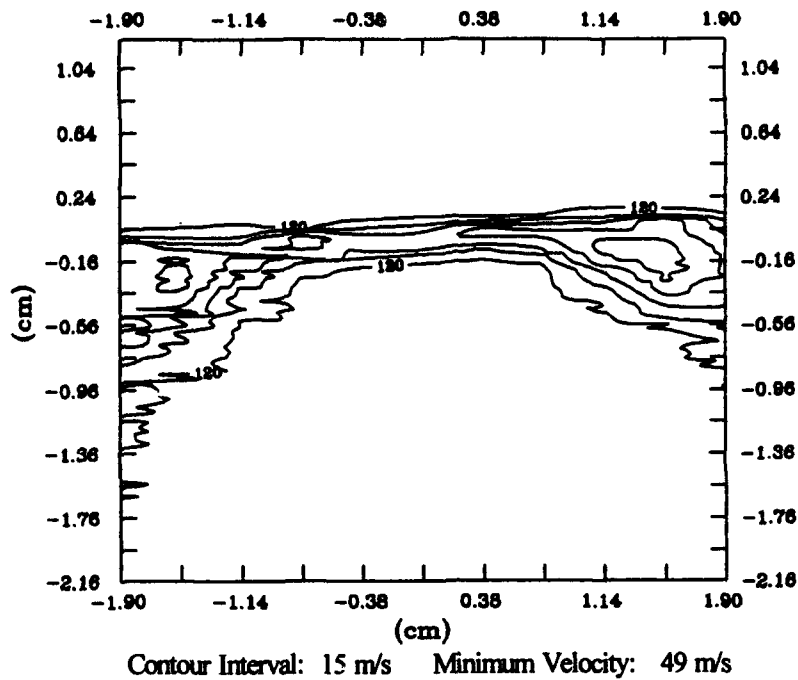
Figure 48.a. Blade 5, Velocity Contours, 0.05c

Contour Interval: 5 m/s   Minimum Velocity: 90 m/s
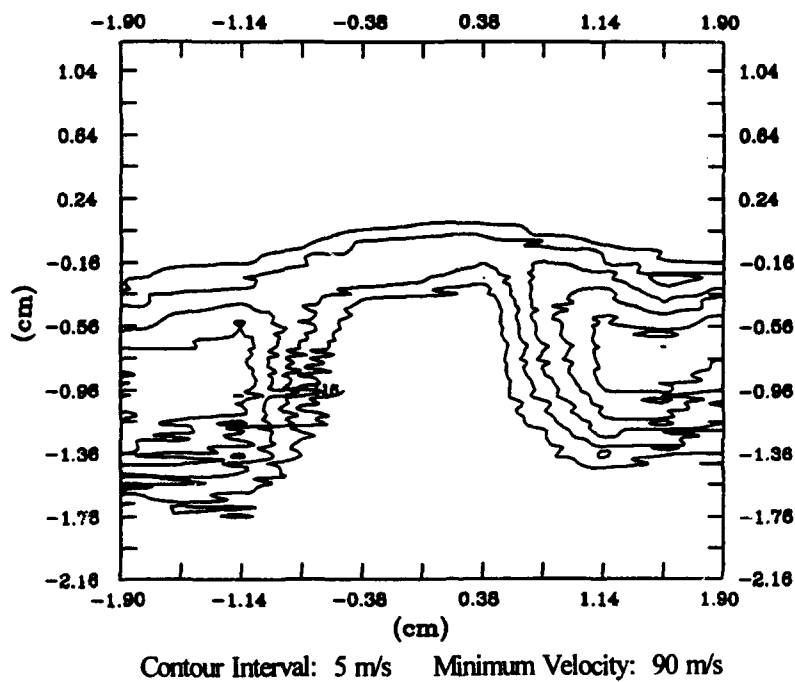
Figure 48.b. Blade 5, Velocity Contours, 1.37c

134
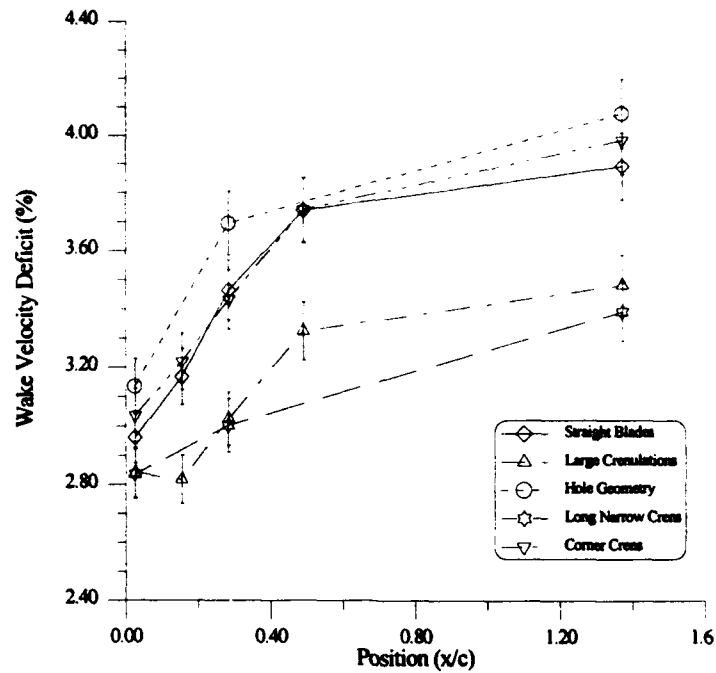
Figure 49. Wake Velocity Deficit
(including corner crenulations)
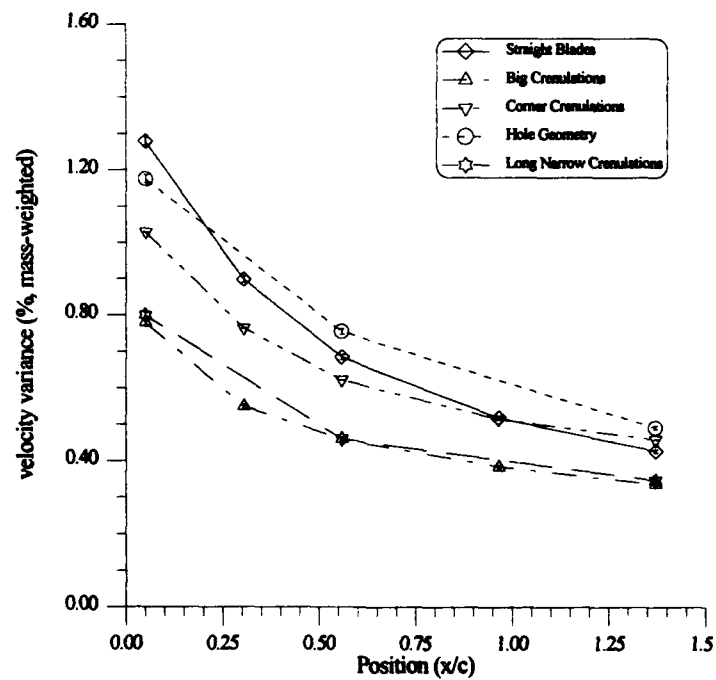
Figure 50. Outlet Velocity Variance
(including corner crenulations)

135
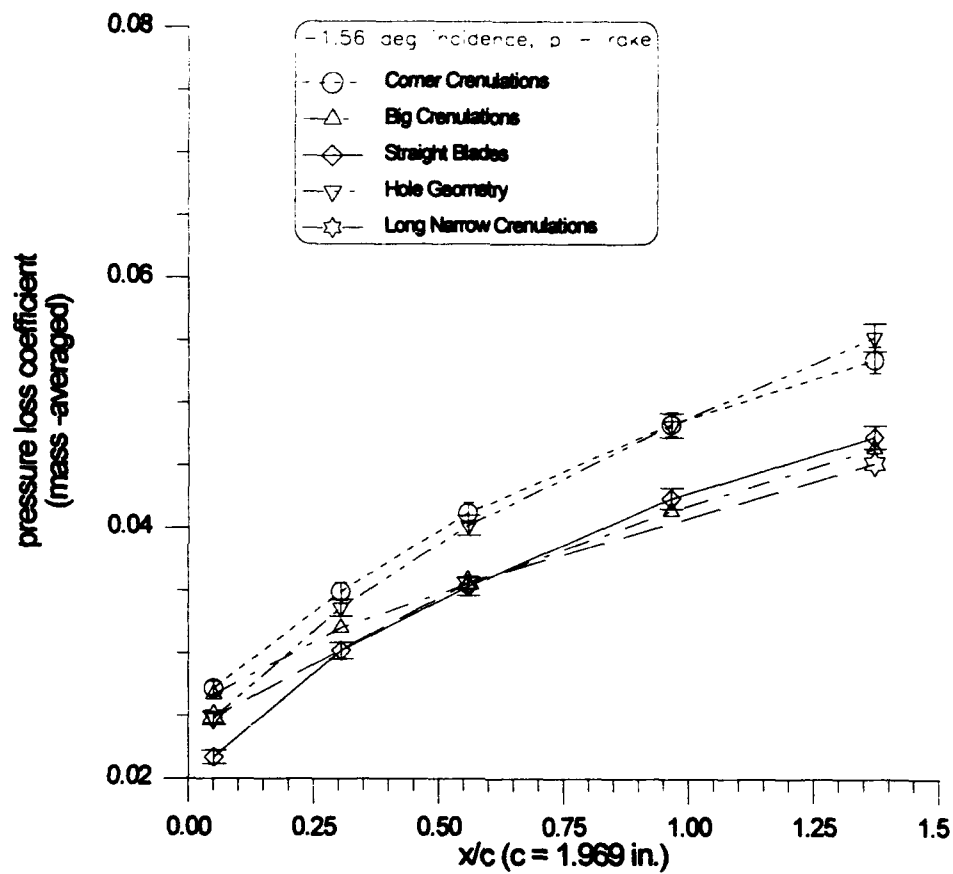
Figure 51. Pressure Loss Coefficient
(from pressure data only)

136

Appendix F: Contour Plots

This appendix contains a complete set of contour plots for each of the configurations tested. These plots include velocity and ω for all of the sampling planes and contour plots of turning angle at the 0.05c and 1.37c locations. The contour plots for Blade 5 are not included since the data was not verified with repeat runs.

Velocity Contours, Straight Blades, 0.05c
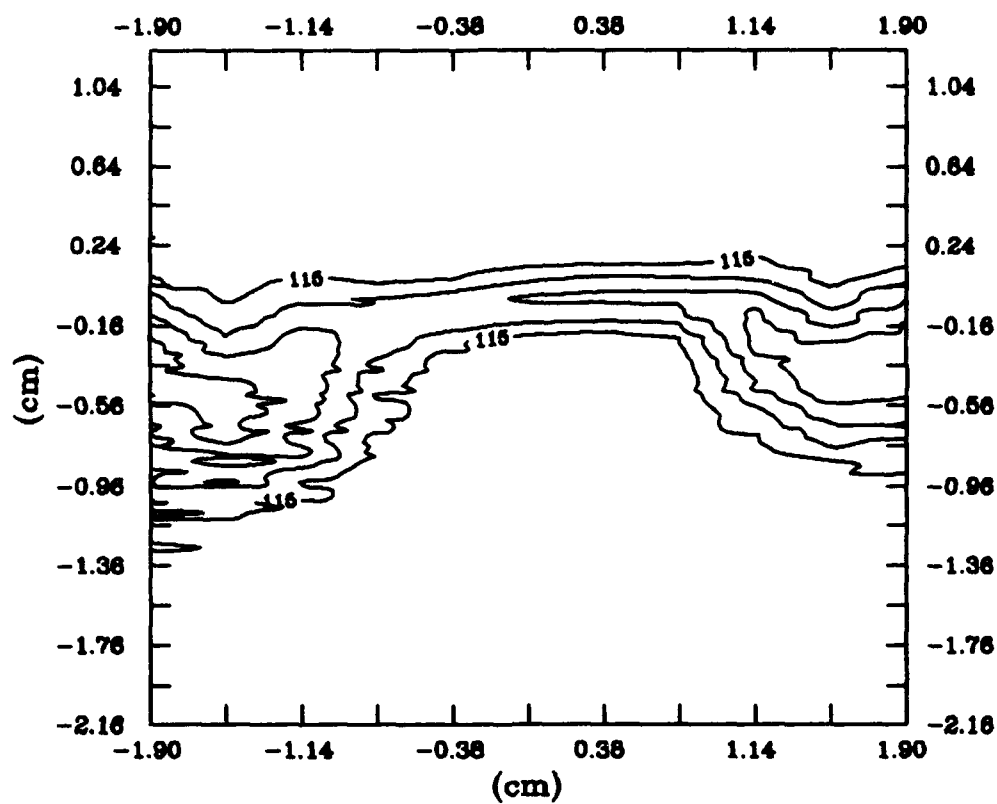
(Contour Interval: 15 m/s, Minimum Velocity: 36 m/s)

Velocity Contours, Straight Blades, 0.30c

(Contour Interval: 10 m/s, Minimum Velocity: 59 m/s)

139

Velocity Contours, Straight Blades, 0.56c

(Contour Interval: 10 m/s, Minimum Velocity: 75 m/s)
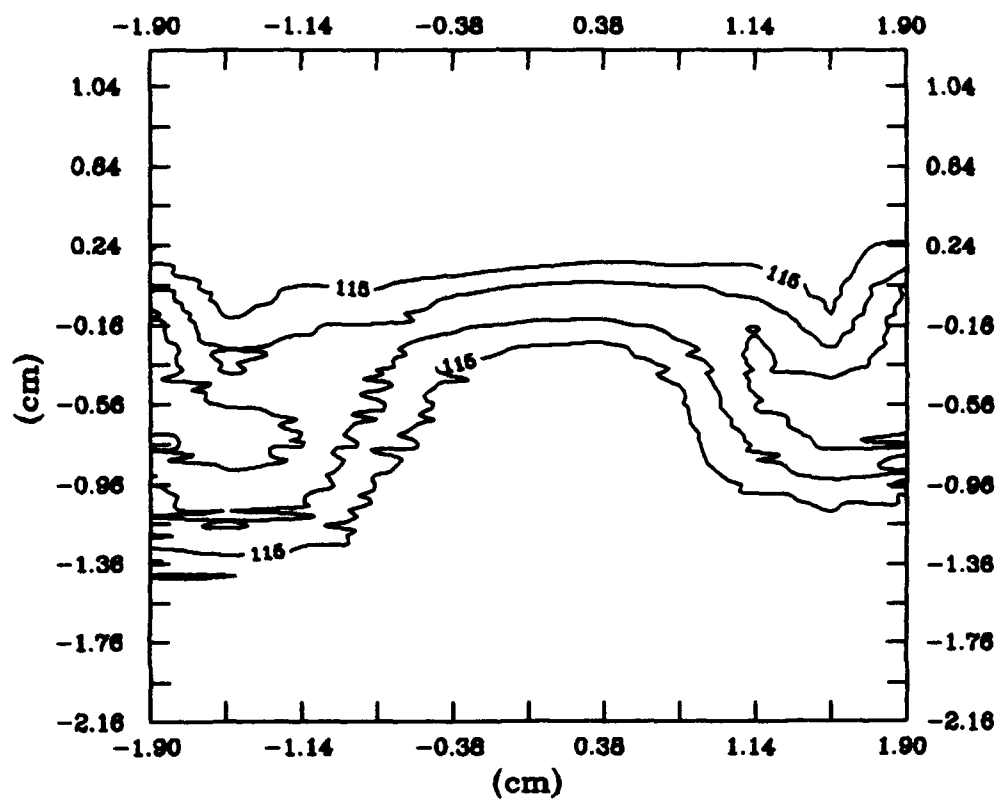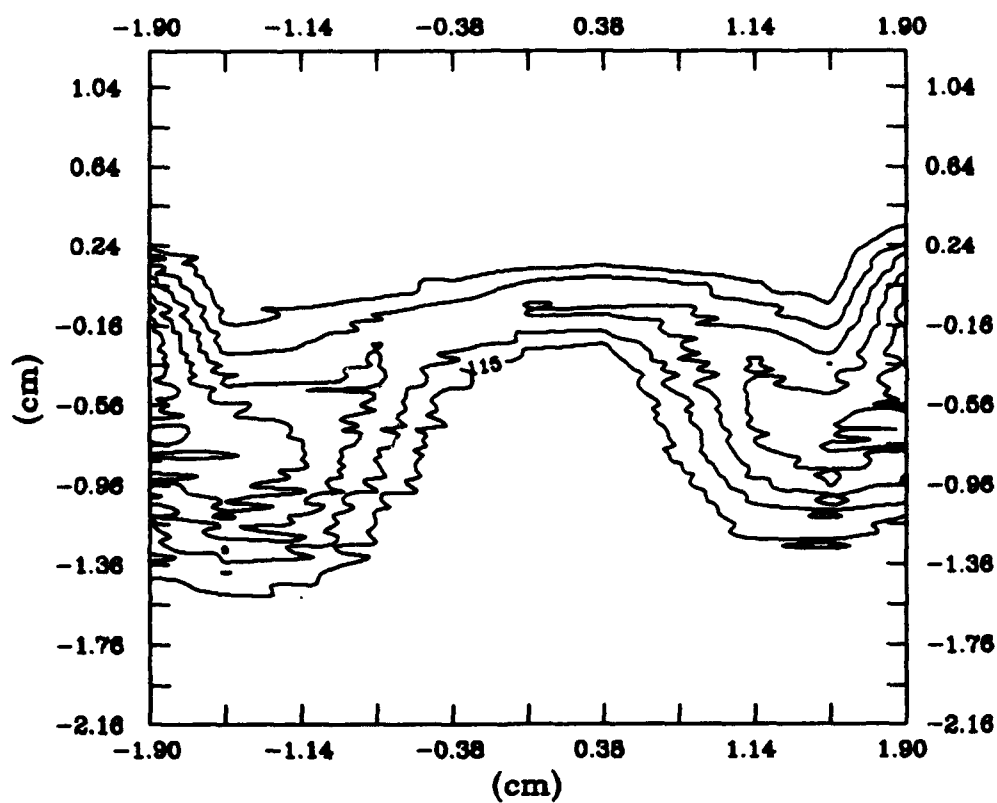
140

Velocity Contours, Straight Blades, 0.96c

(Contour Interval: 10 m/s, Minimum Velocity: 85 m/s)

141

Velocity Contours, Straight Blades, 1.37c

(Contour Interval: 5 m/s, Minimum Velocity: 91 m/s)

142

Velocity Contours, Blade 2, 0.05c

(Contour Interval: 15 m/s, Minimum Velocity: 53 m/s)

143
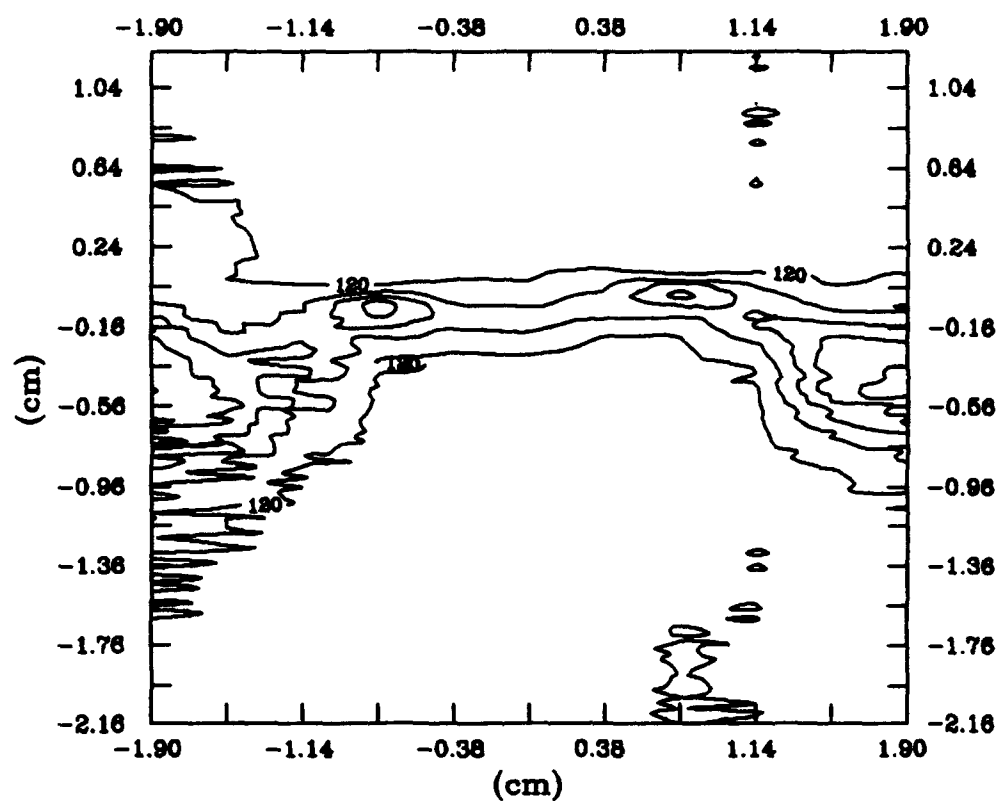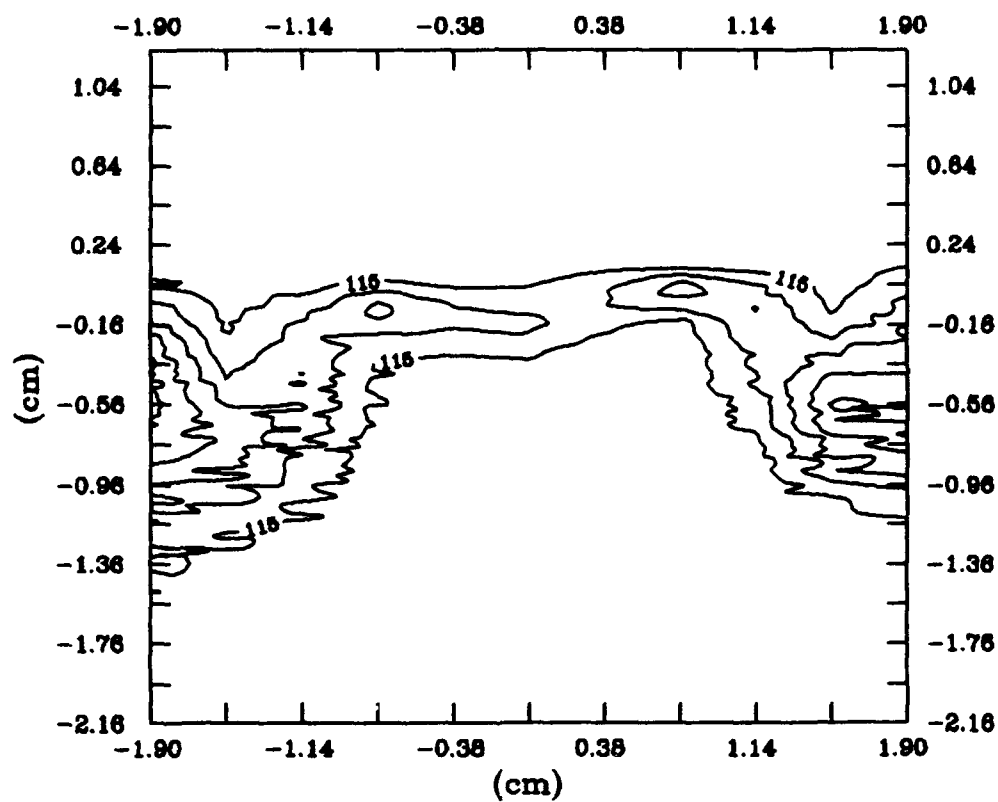
Velocity Contours, Blade 2, 0.30c

(Contour Interval: 10 m/s, Minimum Velocity: 69 m/s)

144
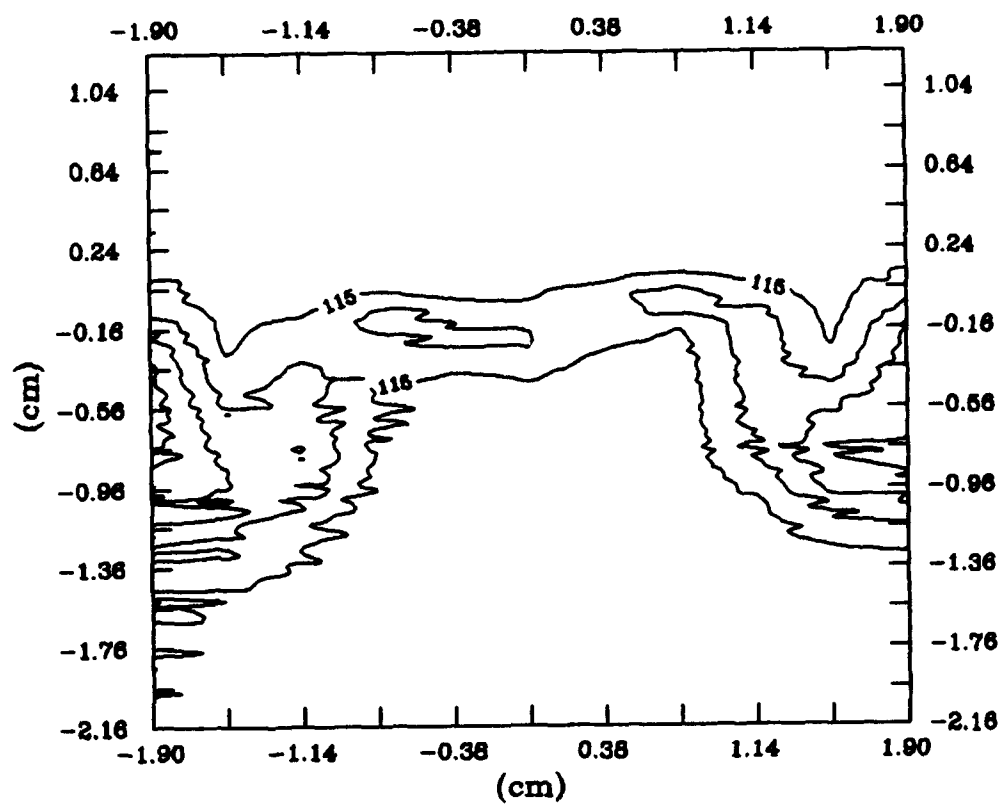
Velocity Contours, Blade 2, 0.56c

(Contour Interval: 10 m/s, Minimum Velocity: 77 m/s)
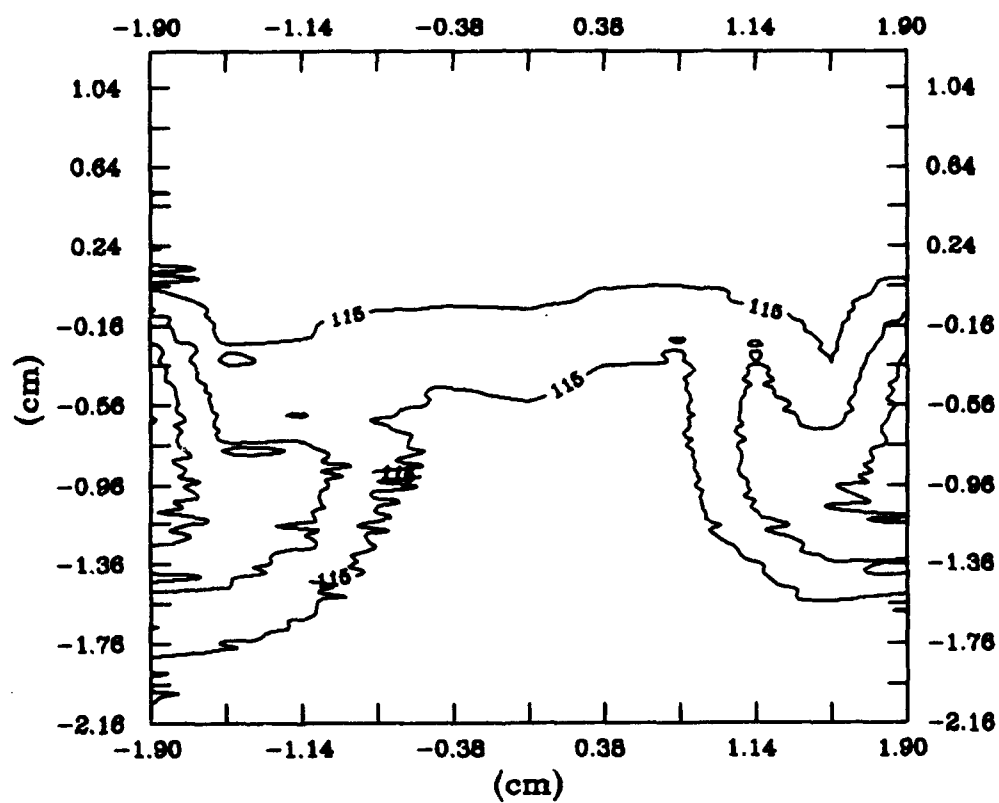
Velocity Contours, Blade 2, 0.96c

(Contour Interval: 10 m/s, Minimum Velocity: 83 m/s)
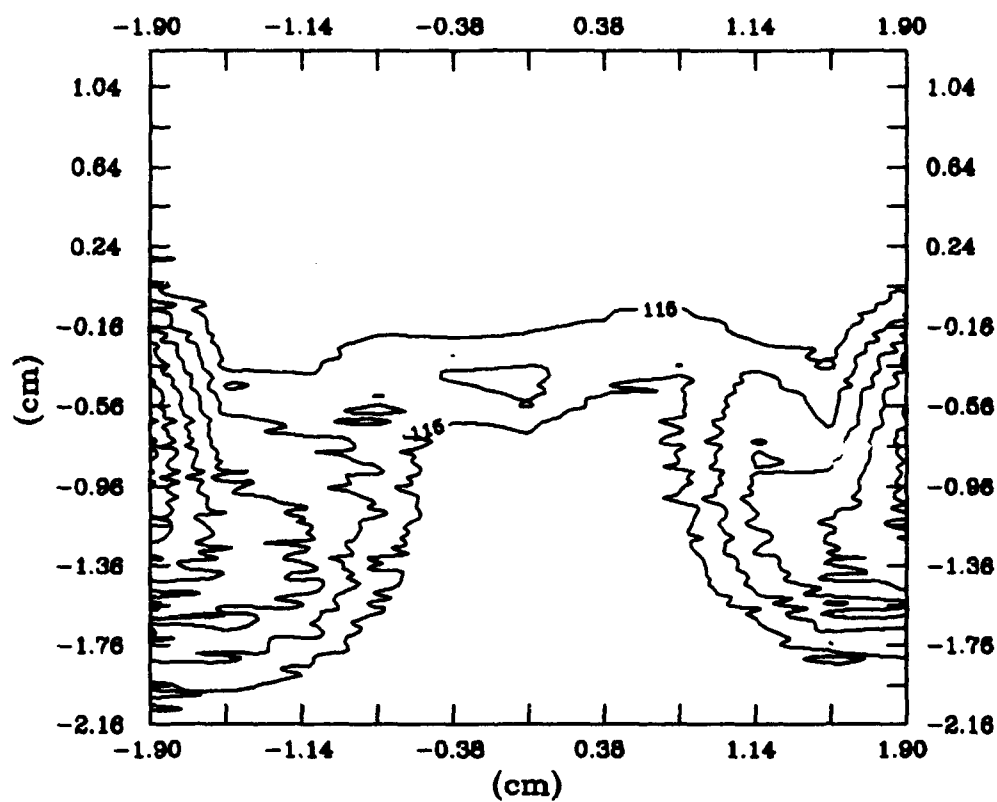
Velocity Contours, Blade 2, 1.37c
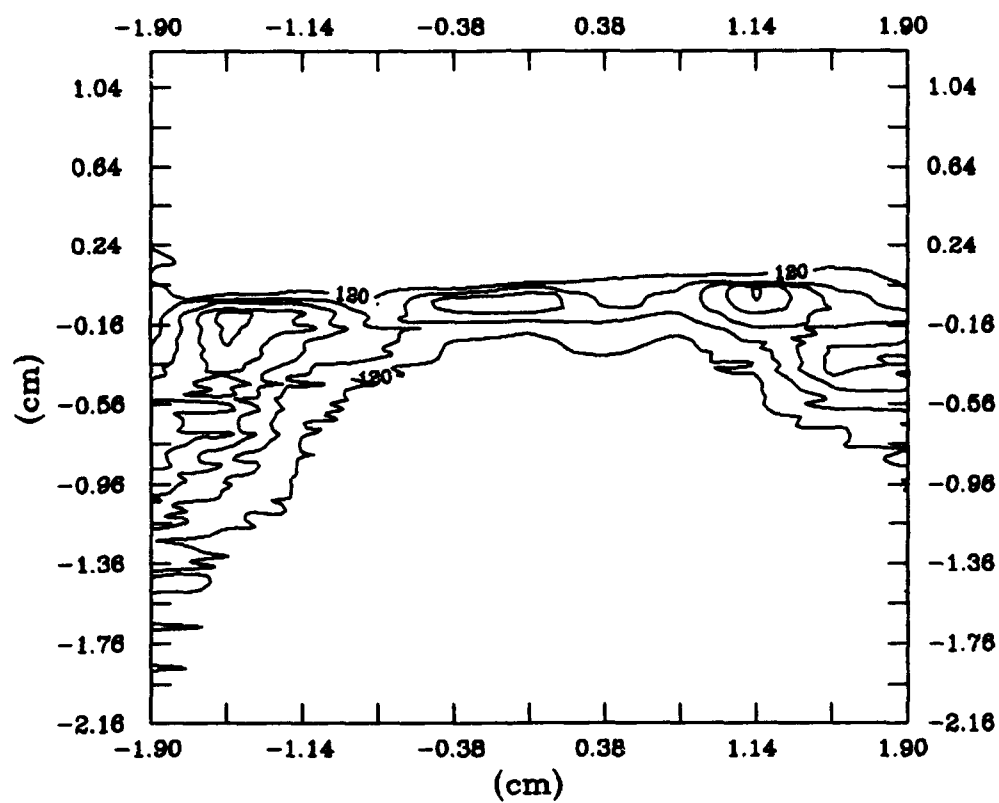
(Contour Interval: 5 m/s, Minimum Velocity: 88 m/s)

147

Velocity Contours, Blade 3, 0.05c

(Contour Interval: 15 m/s, Minimum Velocity: 52 m/s)

148
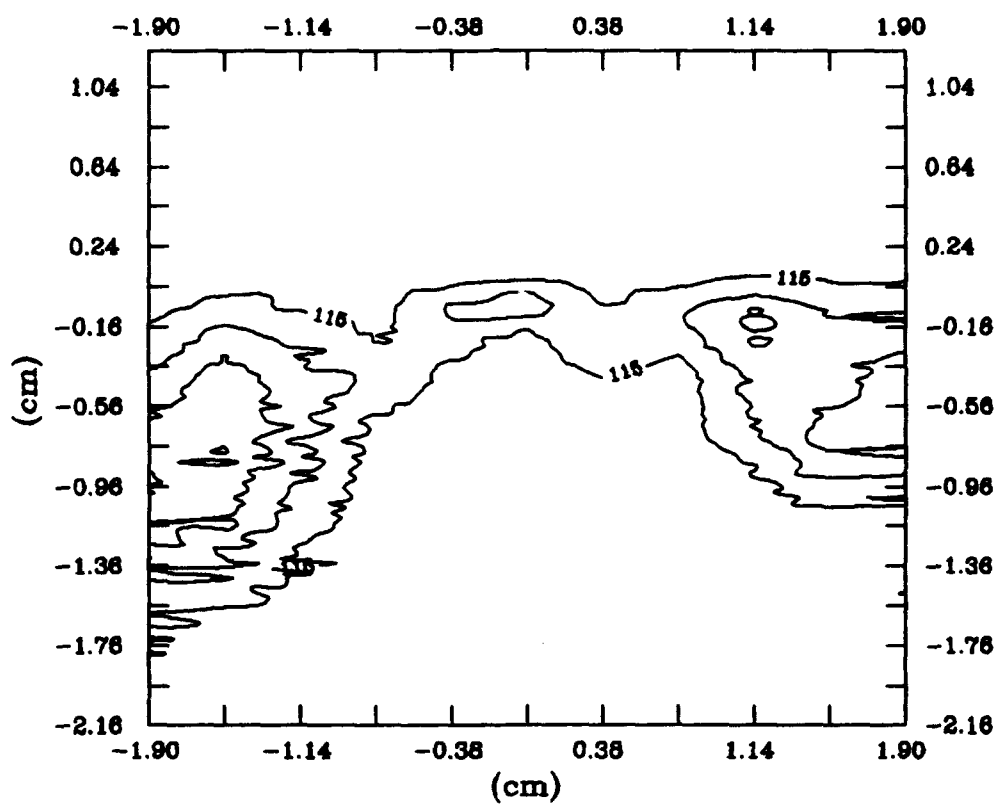
Velocity Contours, Blade 3, 0.56c

(Contour Interval: 10 m/s, Minimum Velocity: 82 m/s)

149
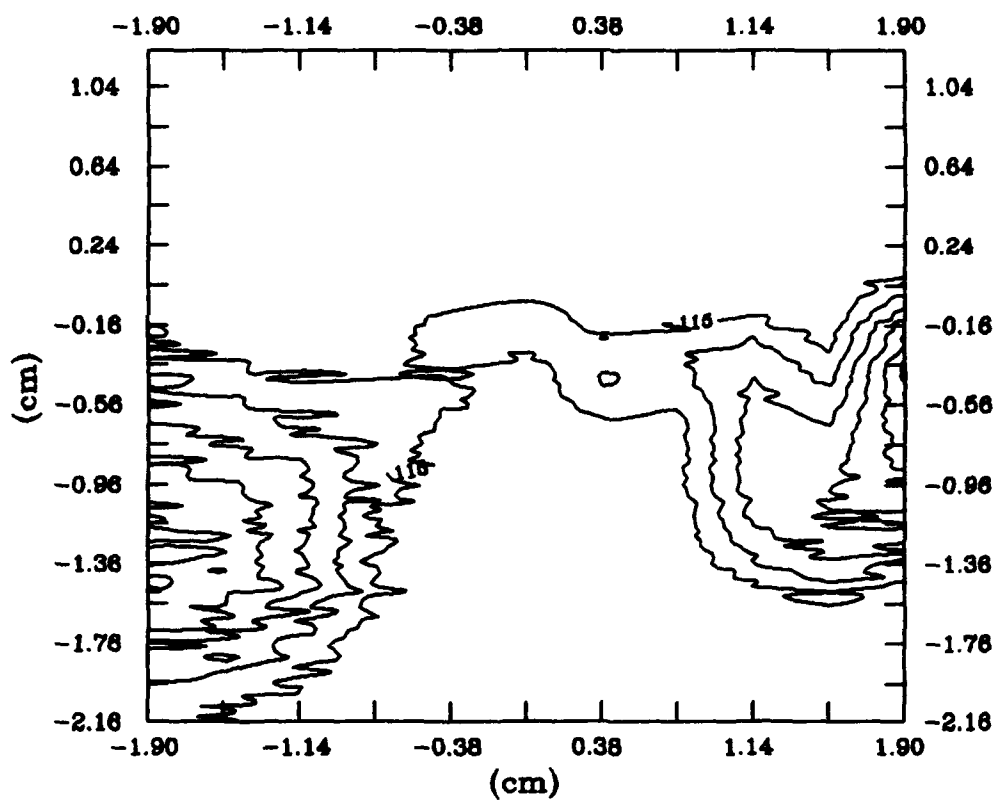
Velocity Contours, Blade 3, 1.37c

(Contour Interval: 5 m/s, Minimum Velocity: 89 m/s)

150
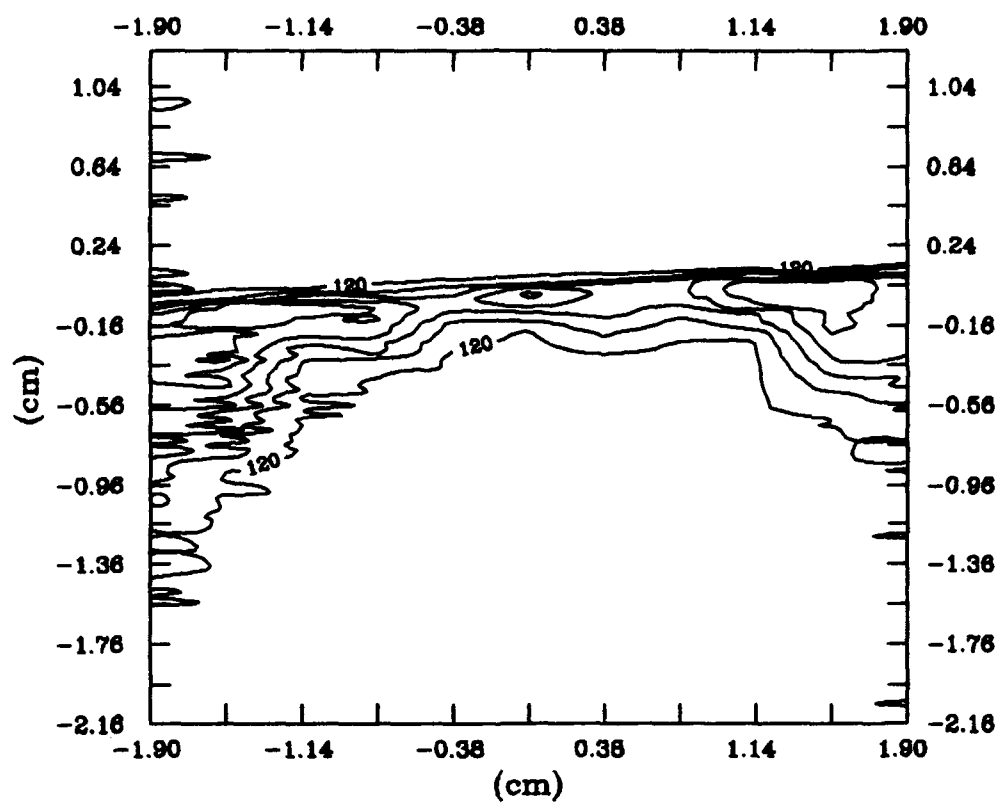
Velocity Contours, Blade 4, 0.05c

(Contour Interval: 15 m/s, Minimum Velocity: 42 m/s)

Velocity Contours, Blade 4, 0.56c

(Contour Interval: 10 m/s, Minimum Velocity: 68 m/s)

Velocity Contours, Blade 4, 1.37c

(Contour Interval: 5 m/s, Minimum Velocity: 86 m/s)

153

ω Contours, Straight Blades, 0.05c

(Contour Interval: 0.15, Maximum ω: 0.81)

154

ω Contours, Straight Blades, 0.30c

(Contour Interval: 0.15, Maximum ω: 0.64)

155

ω Contours, Straight Blades, 0.56c

(Contour Interval: 0.10, Maximum ω: 0.52)

156

ω Contours, Straight Blades, 0.96c

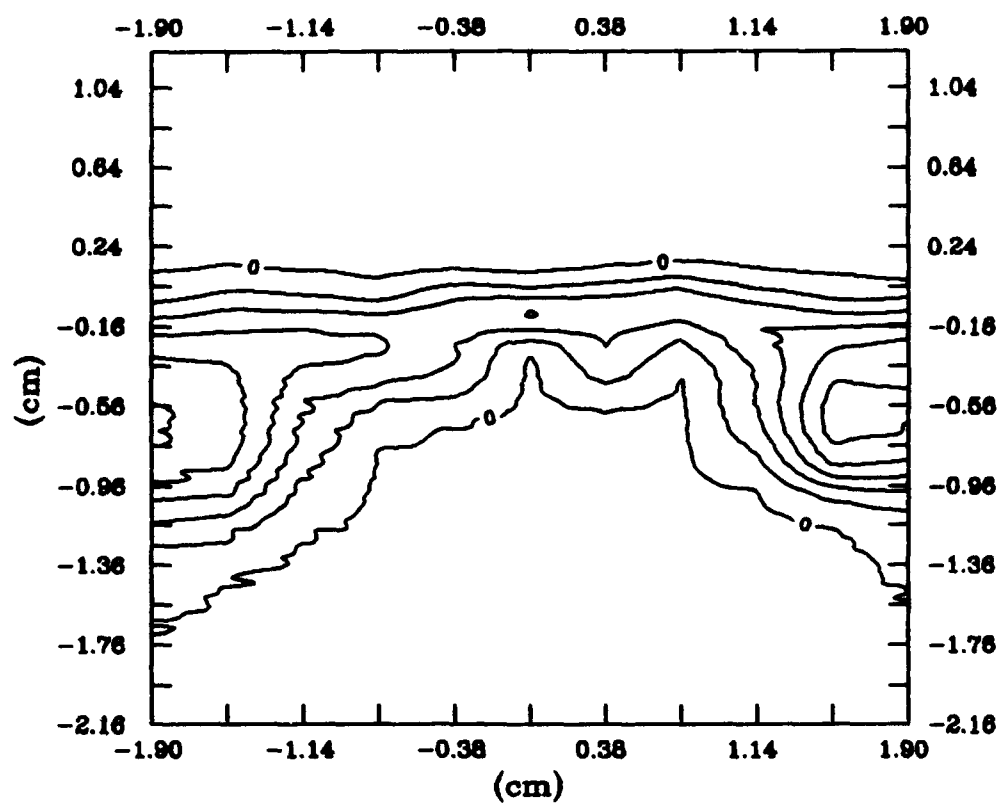(Contour Interval: 0.10, Maximum ω: 0.42)

157

ω Contours, Straight Blades, 1.37c

(Contour Interval: 0.05, Maximum ω: 0.38)

158

ω Contours, Blade 2, 0.05c

(Contour Interval: 0.15, Maximum ω: 0.64)

ω Contours, Blade 2, 0.30c

(Contour Interval: 0.15, Maximum ω: 0.52)

ω Contours, Blade 2, 0.56c

(Contour Interval: 0.10, Maximum ω: 0.47)

161

ω Contours, Blade 2, 0.96c

(Contour Interval: 0.10, Maximum ω: 0.43)

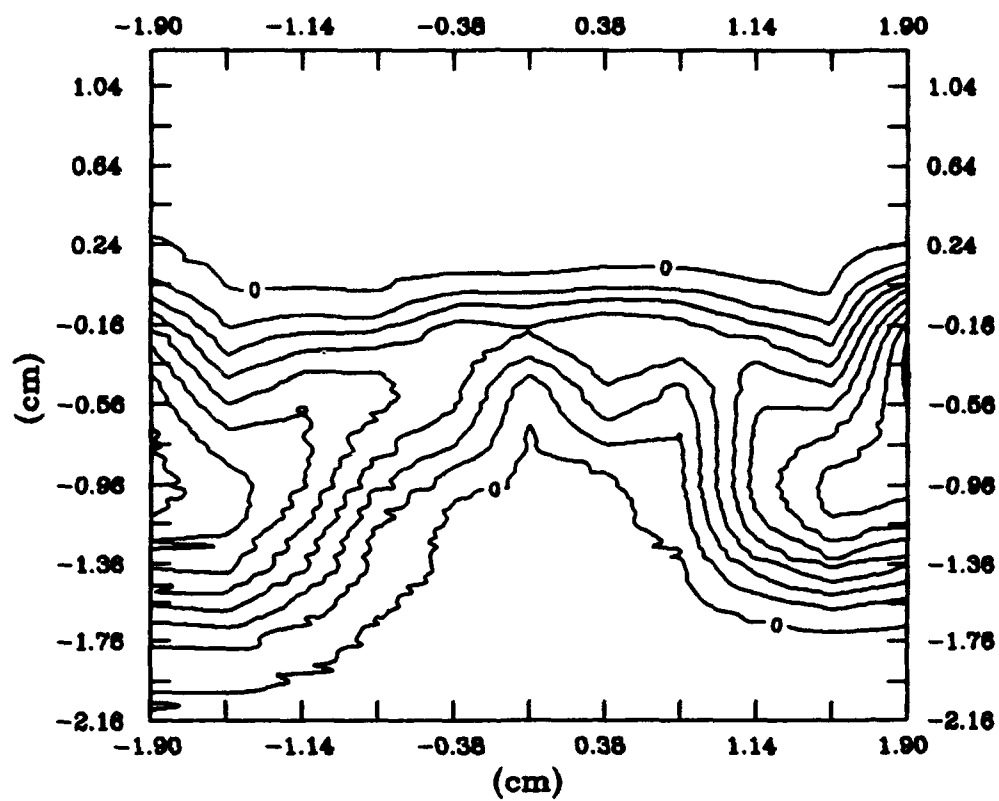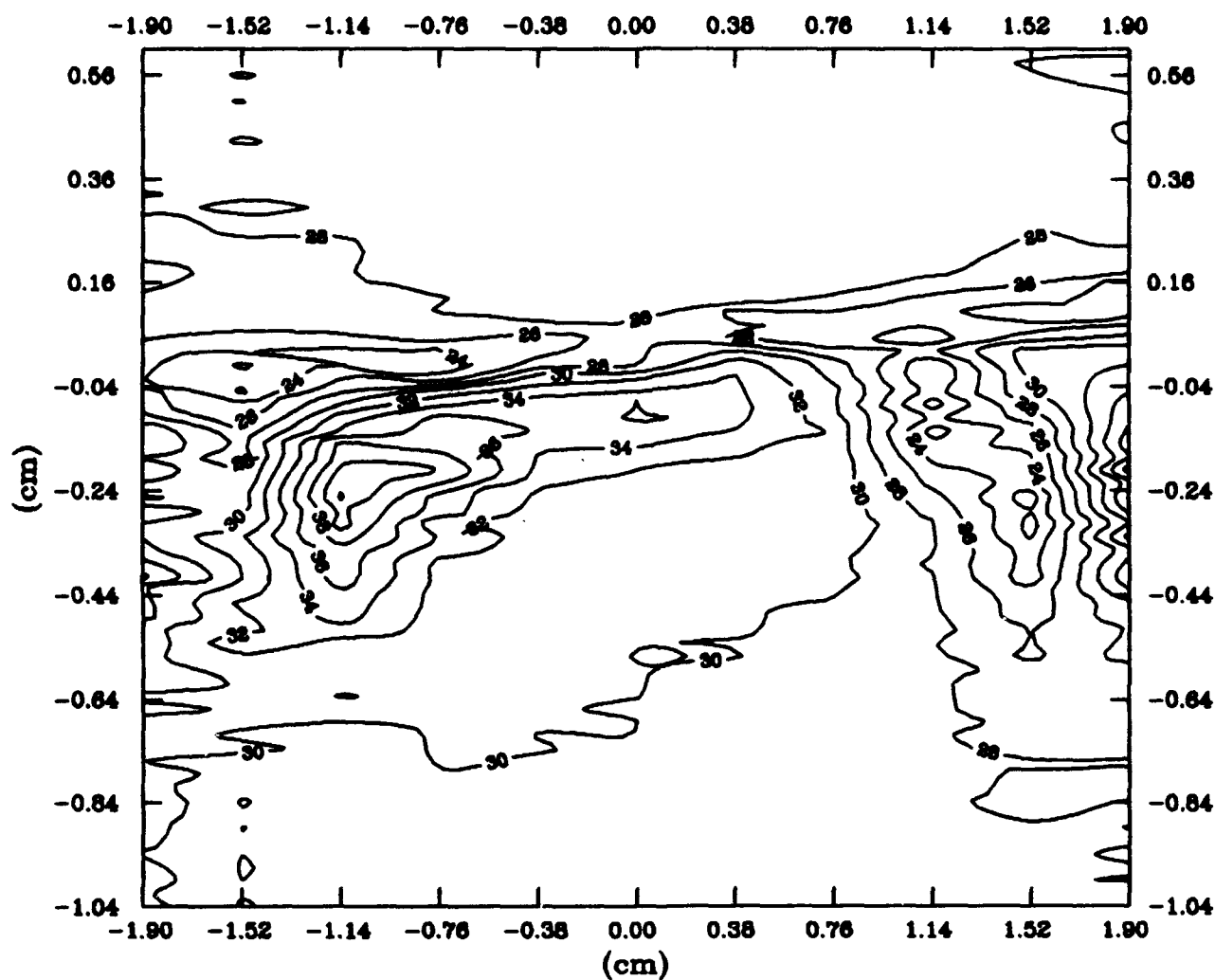ω Contours, Blade 2, 1.37c

(Contour Interval: 0.05, Maximum ω: 0.39)

163

ω Contours, Blade 3, 0.05c

(Contour Interval: 0.15, Maximum ω: 0.72)

164

ω Contours, Blade 3, 0.56c

(Contour Interval: 0.10, Maximum ω: 0.43)

ω Contours, Blade 3, 1.37c

(Contour Interval: 0.05, Maximum ω: 0.38)

ω Contours, Blade 4, 0.05c

(Contour Interval: 0.15, Maximum ω: 0.81)

167

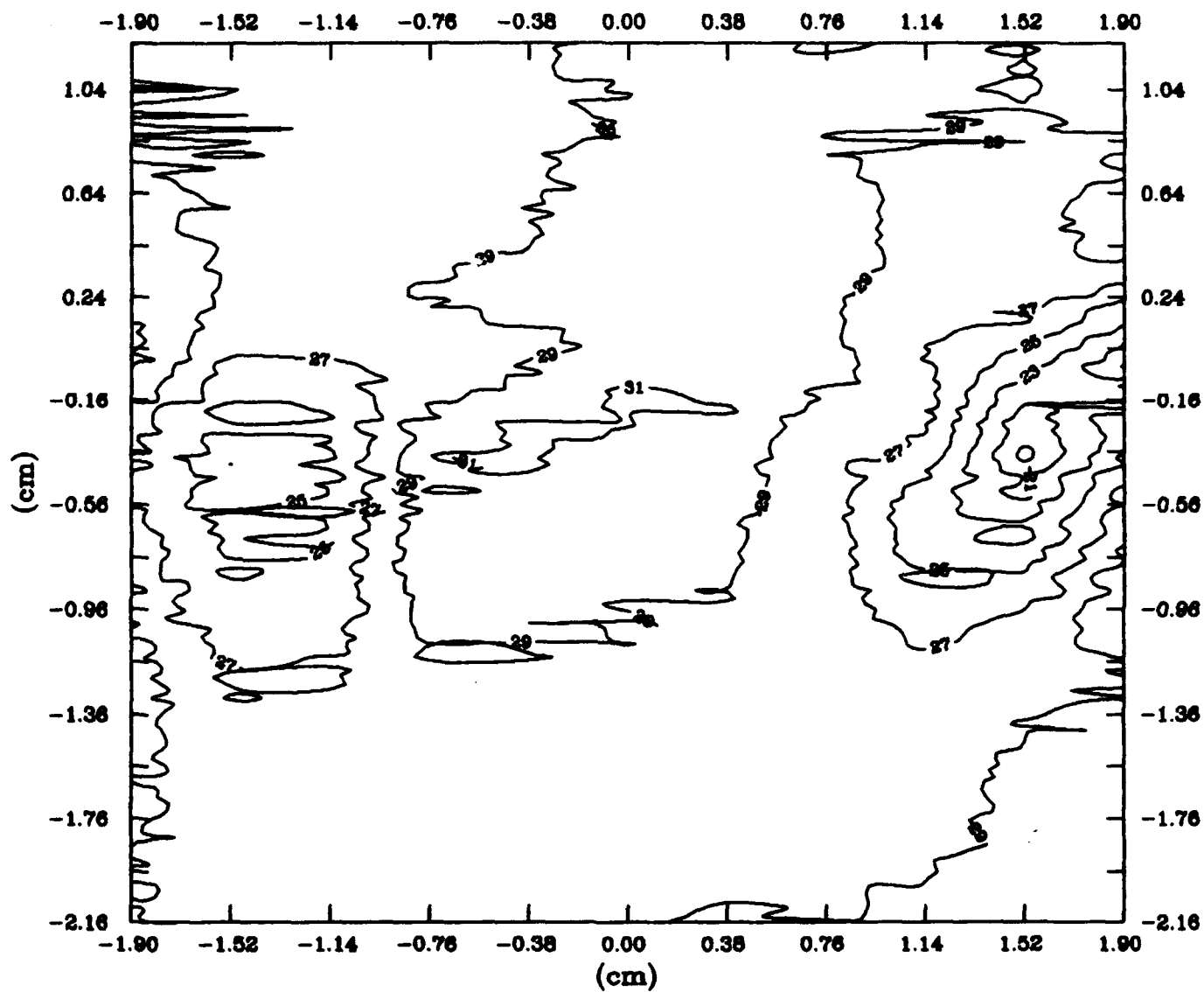ω Contours, Blade 4, 0.56c

(Contour Interval: 0.10, Maximum ω: 0.55)

ω Contours, Blade 4, 1.37c

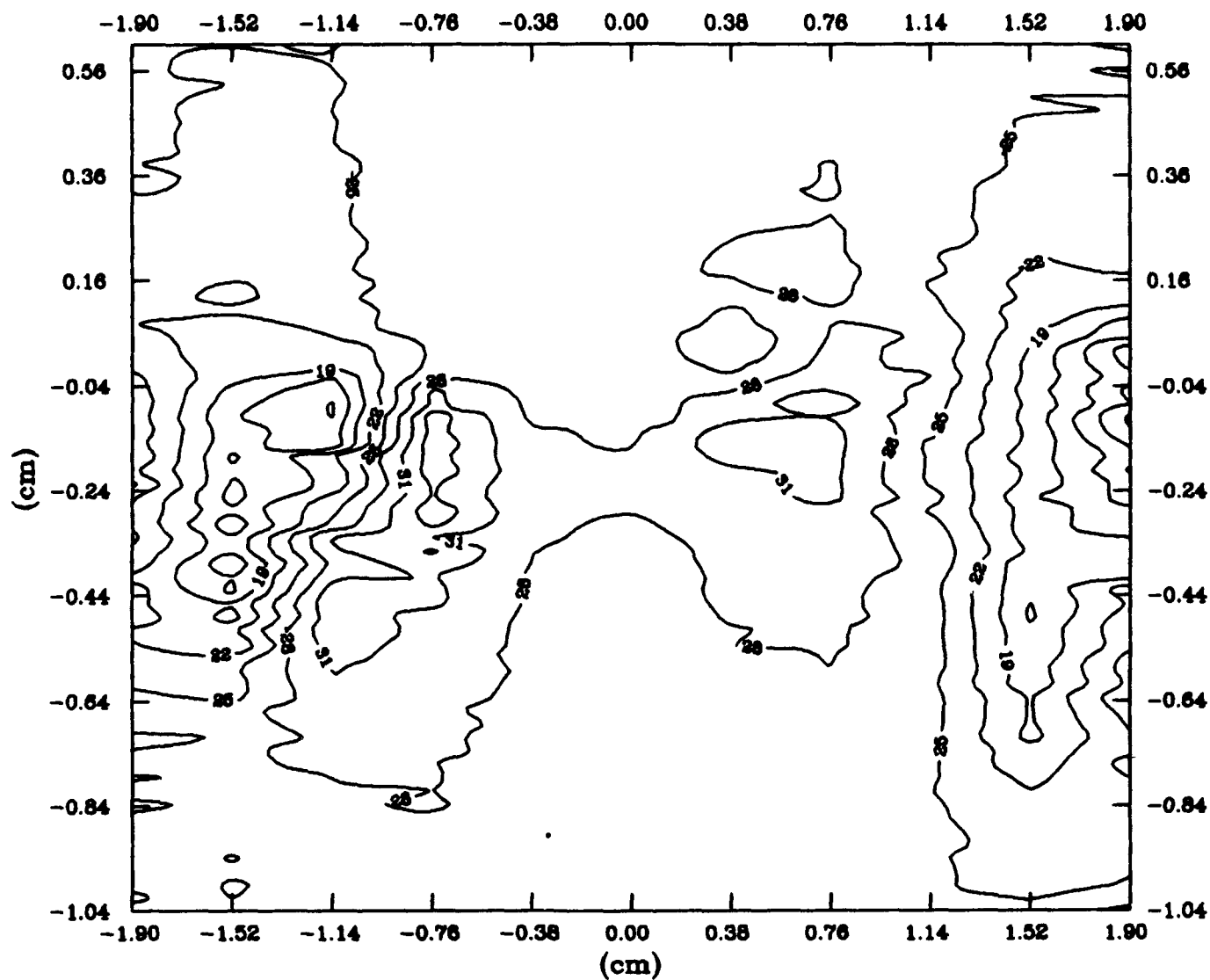(Contour Interval: 0.05, Maximum ω: 0.42)

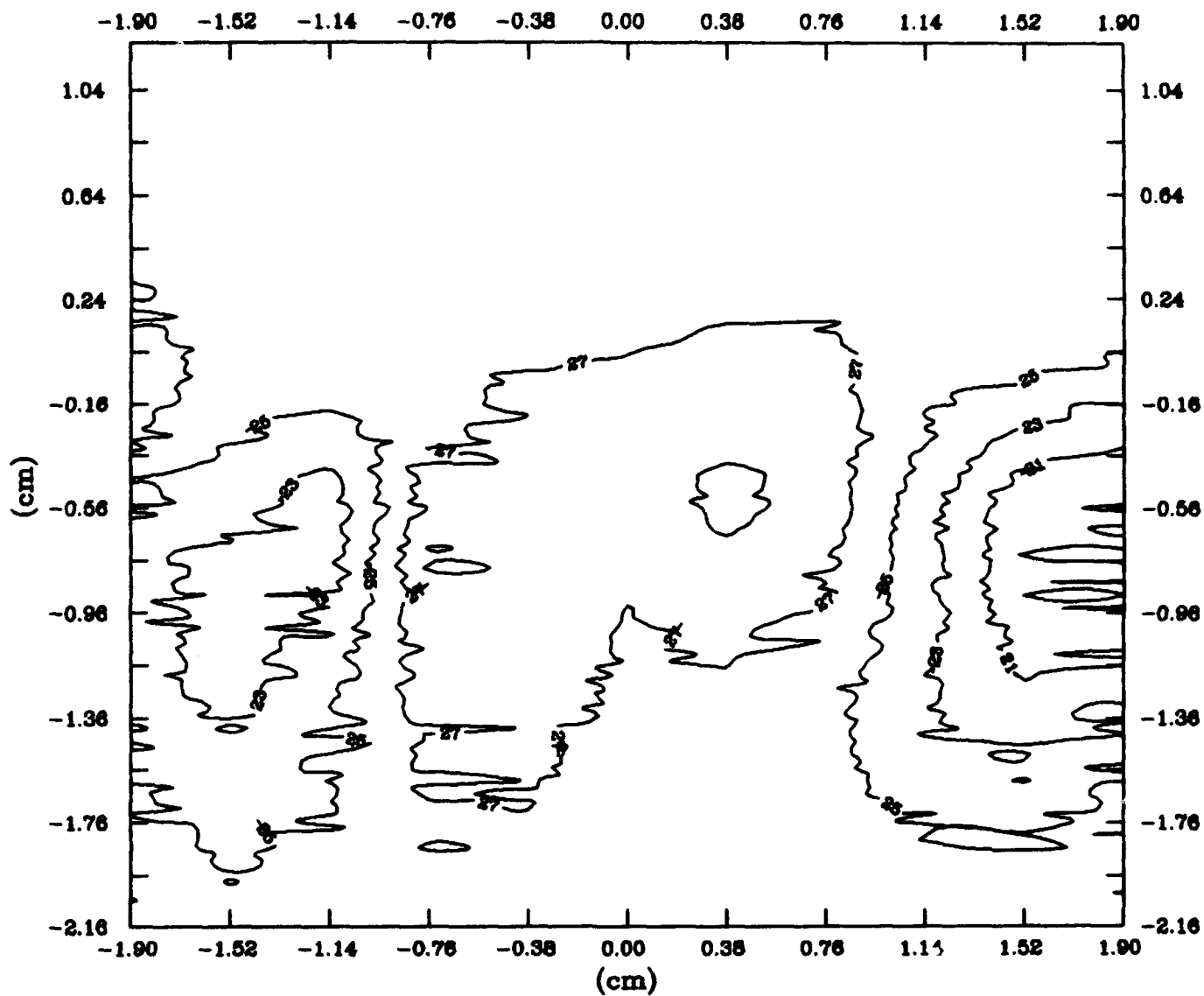Turning Angle Contours, Straight Blades, 0.05c

(Contour Interval: 2°)

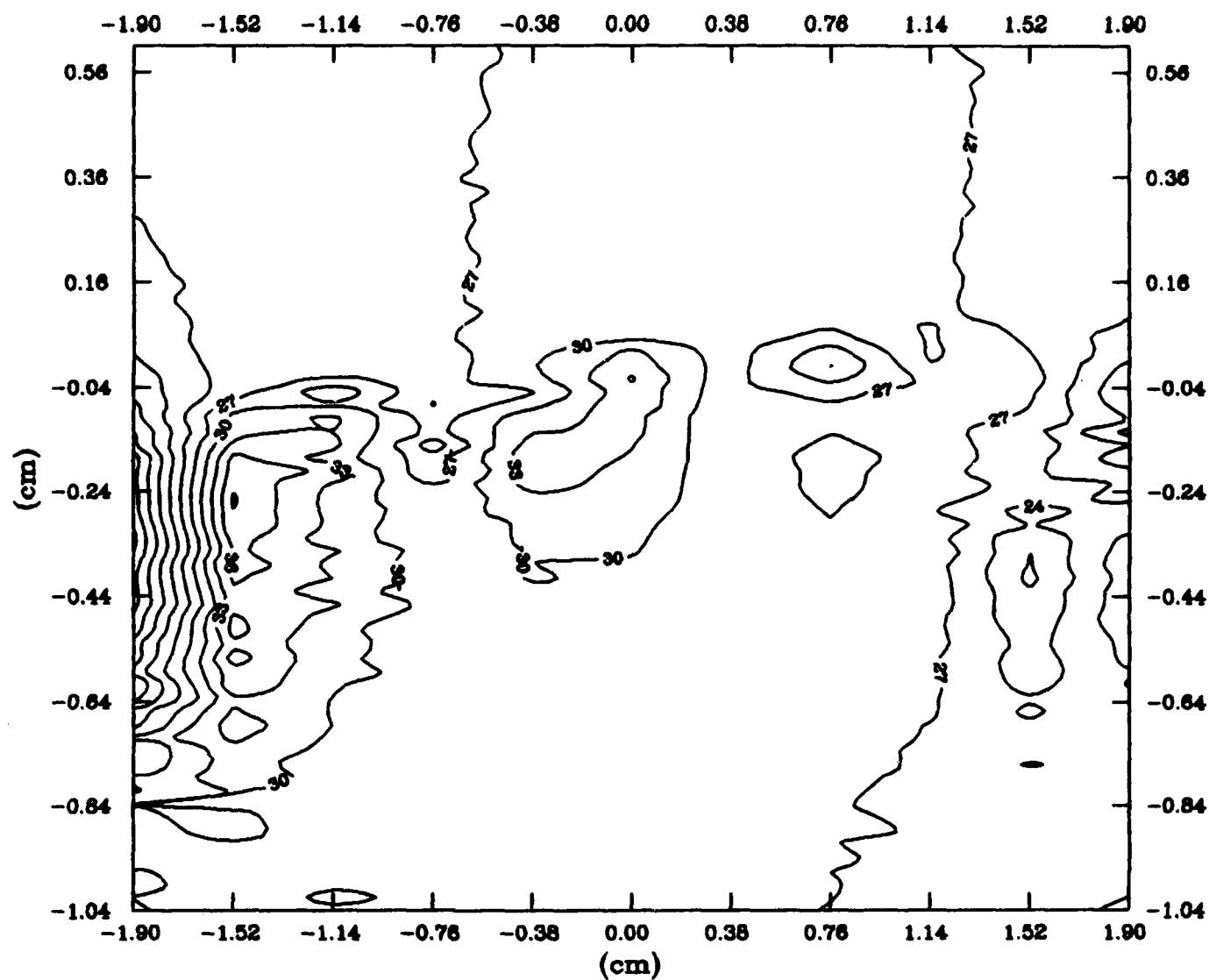Turning Angle Contours, Straight Blades, 1.37c

(Contour Interval: 2°)

171

Turning Angle Contours, Blade 2, 0.05c

(Contour Interval: 2°)
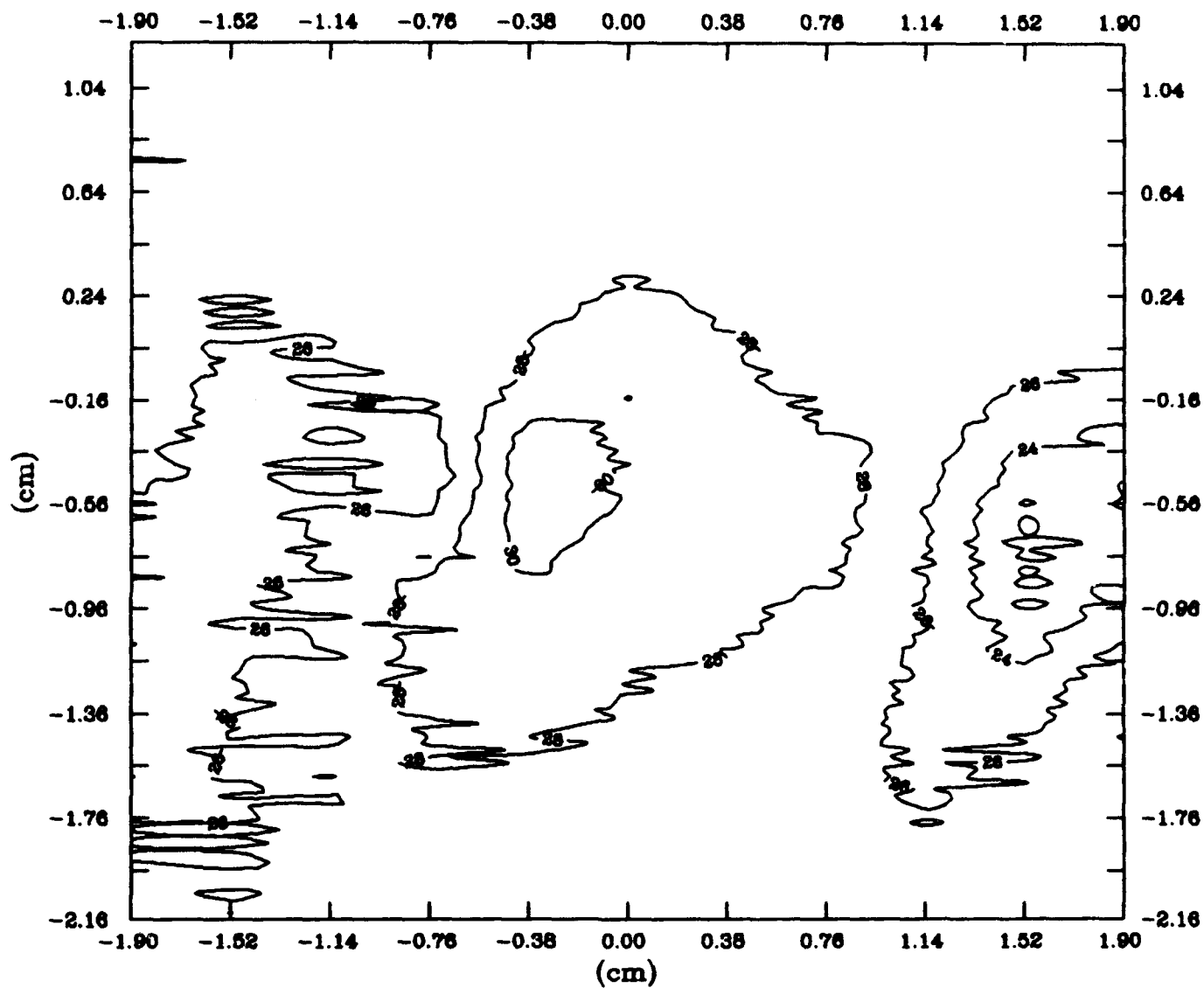
172

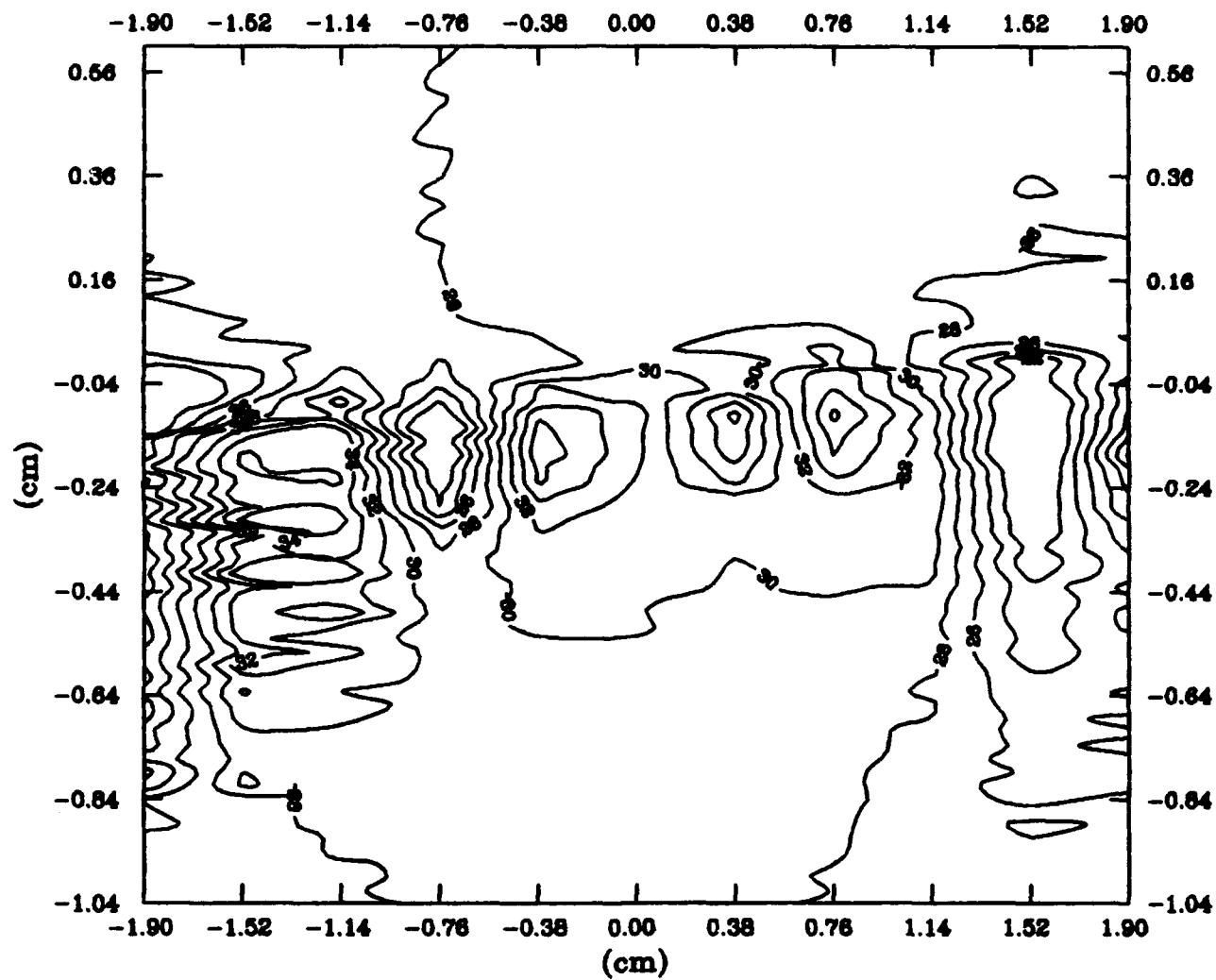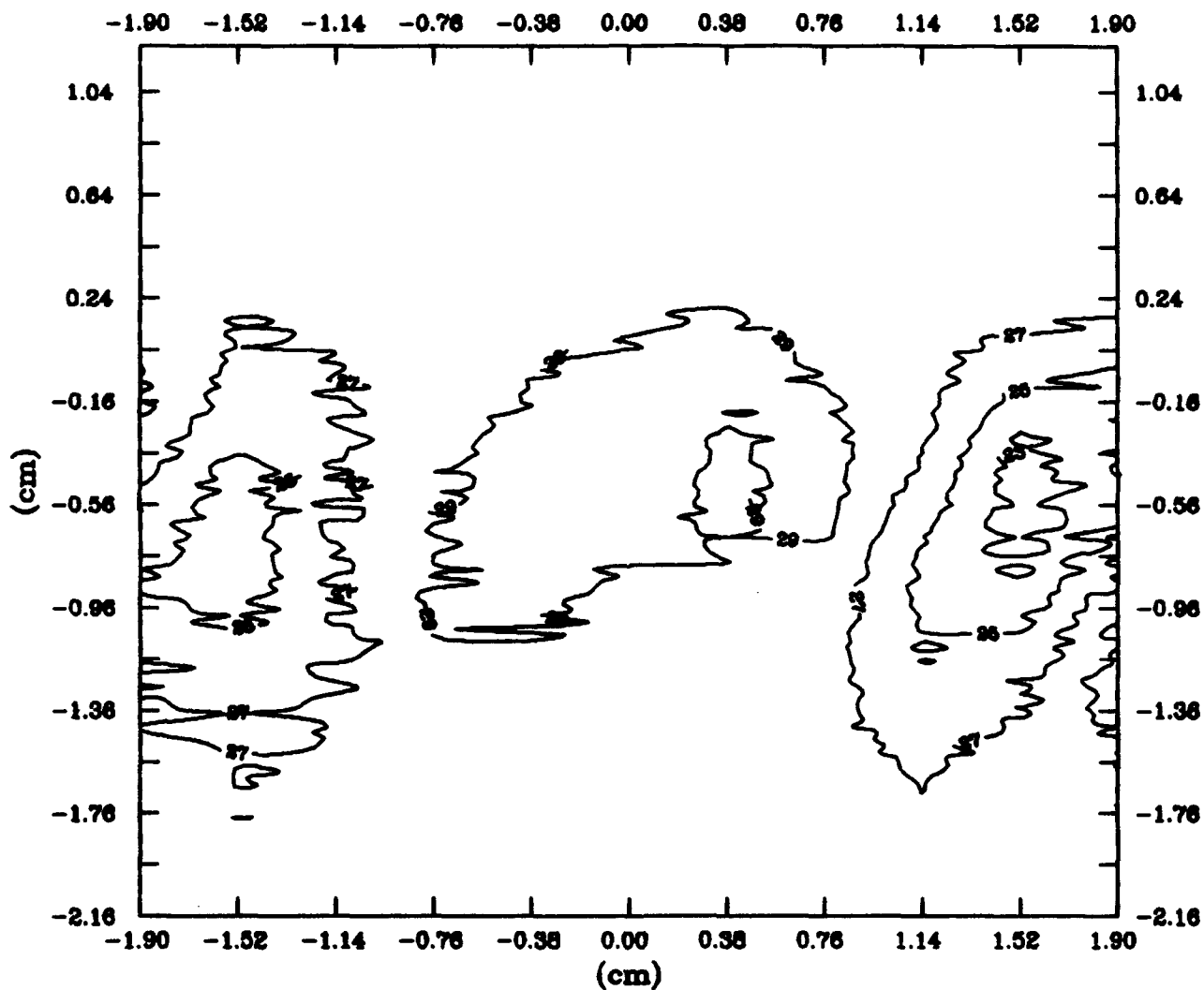Turning Angle Contours, Blade 2, 1.37c

(Contour Interval: 2°)

Turning Angle Contours, Blade 3, 0.05c

(Contour Interval: 2°)

Turning Angle Contours, Blade 3, 1.37c

(Contour Interval: 2°)

175

Turning Angle Contours, Blade 4, 0.05c

(Contour Interval: 2°)

Turning Angle Contours, Blade 4, 1.37c

(Contour Interval: 2°)

177

Vita

Capt William L. Spacy II was born on 7 May 1961 at Ft Dix NJ. He graduated from Zweibruecken American High School, Zweibruecken AB, FRG, in 1979 and went on to attend the United States Air Force Academy. In 1983 with a Bachelor of Sciences degree in Astronautical Engineering. Following graduation, he attended Under Graduate Pilot Training at Williams AFB, AZ and graduating from that program in 1985. Capt Spacy was next assigned to fly C-23 aircraft at Zweibruecken AB, FRG where he accumulated 1100 hours and qualified as an aircraft commander. Following this three year tour he attended C-130 transition training at Little Rock AFB, AR. This training was followed by a four year tour at Dyess AFB, TX where he accumulated 1200 hours flying C-130 aircraft.

In 1992, Capt Spacy entered the Master's Program in Aeronautical Engineering at the Air Force Institute of Technology. This paper was written in partial fulfillment of the graduation requirements.

Permanent Home Address:

24 Shadybrook Circle

Abilene, TX 79605

REPORT DOCUMENTATION PAGE

Public reporting burden for this collection of information is estimated to average 1 hour per response, including the time for reviewing instructions, searching existing data sources, gathering and maintaining the data needed, and completing and reviewing the collection of information. Send comments regarding this burden estimate or any other aspect of this collection of information, including suggestions for reducing this burden, to Washington Headquarters Services, Directorate for Information Operations and Reports, 1215 Jefferson Davis Highway, Suite 1204, Arlington, VA 22202-4302, and to the Office of Management and Budget, Paperwork Reduction Project (0704-0188), Washington, DC 20503.

1. AGENCY USE ONLY (Leave blank)	2. REPORT DATE DEC 93	3. REPORT TYPE AND DATES COVERED Master's Thesis

4. TITLE AND SUBTITLE

Effects of Crenulations on Three Dimensional
Losses in a Linear Compressor Cascade

5. FUNDING NUMBERS

6. AUTHOR(S)

Capt William L. Spacy II

7. PERFORMING ORGANIZATION NAME(S) AND ADDRESS(ES)

Air Force Institute of Technology,
WPAFB OH 45433-6538

8. PERFORMING ORGANIZATION REPORT NUMBER

AFIT/GAE/ENY/93D-26

9. SPONSORING/MONITORING AGENCY NAME(S) AND ADDRESS(ES)

10. SPONSORING/MONITORING AGENCY REPORT NUMBER

11. SUPPLEMENTARY NOTES

12a. DISTRIBUTION/AVAILABILITY STATEMENT

Approved for public release; distribution unlimited

12b. DISTRIBUTION CODE

13. ABSTRACT (Maximum 200 words)

An experimental investigation into the effect of compressor blade trailing edge geometry on three-dimensional flows in a linear cascade was conducted at the AFIT linear cascade test facility. Hot-wire/hot-film anemometry along with total pressure instrumentation was used to analyze crenulation generated vortices and their interaction with the three-dimensional flows in the cascade. The effects of this interaction on the performance parameters associated with the cascade were quantified. The results indicate that wake mixing is better for crenulated trailing edges and that the precise geometry of the crenulations is critical to performance. One crenulation geometry was found to increase wake mixing while slightly reducing the total pressure losses.

14. SUBJECT TERMS

Airfoil; Axial Flow Compressor Blades; Cascades; Crenulations;
Boundary Layer; Vortices; Secondary Flows; Wakes

15. NUMBER OF PAGES

195

16. PRICE CODE

17. SECURITY CLASSIFICATION OF REPORT	18. SECURITY CLASSIFICATION OF THIS PAGE	19. SECURITY CLASSIFICATION OF ABSTRACT	20. LIMITATION OF ABSTRACT
Unclassified	Unclassified	Unclassified	UL